Advanced Heteroatom Doped Nanocarbon Materials as Platinum catalyst Supports for Fuel Cells

by

Md Ariful Hoque

A thesis
presented to the University of Waterloo
in fulfillment of the
thesis requirement for the degree of
Doctor of Philosophy
in
Chemical Engineering (Nanotechnology)

Waterloo, Ontario, Canada, 2016

AUTHOR'S DECLARATION

This thesis contains material which I authored or co-authored: see list of contributions included in the thesis. This is a true copy of the thesis, including any required final revisions, as accepted by my examiners.

I understand that my thesis may be made electronically available to the public.

List of Contributions

Hoque, M. A., Hassan, M. F., Pritzker, M., Choi, J-. Y., Banham, D., Ye S., Knight S., and Chen, Z. (2015) Web-like 3D architecture of Pt nanowires and sulfur doped CNT with superior electrocatalytic performance *(To be submitted)*

Hoque, M. A., Hassan, F., Seo, M. H., Choi, J-. Y., Pritzker, M., Knights S., Ye, S., and Chen, Z. (2016) Optimization of sulfur doped graphene as an emerging platinum nanowires support for oxygen reduction reaction (*Nano Energy 19: 27-38)*

Wang X., Li G., Seo, M. H., Hassan, M. F., **Hoque, M. A.,** and Chen, Z. (2015) Sulfur Atoms Bridging Few-Layered MoS2 with S-doped Graphene Enables Highly Robust Anode for Lithium-ion Batteries (*Advanced Energy Mateirals 5 (23))*

Wang, R., Higgins, D. C., Prabhudev, S., Lee, D. U., Choi, J-. Y., **Hoque, M. A.,** Botton, G., Chen, Z. (2015) Synthesis and structural evolution of Pt nanotubular skeletons: revealing the source of the instability of nanostructured electrocatalysts (*Journal of Materials Chemistry A 3: 12663-12671)* Highlighted as Inside front cover

Higgins, D. C., Hassan, F., Seo, M. H., Choi, J-. Y., **Hoque, M. A.,** Lee, D. U., Chen, Z. (2015) Shape-controlled octahedral cobalt disulfide nanoparticles supported on nitrogen and sulfur-doped graphene/carbon nanotube composites for oxygen reduction in acidic electrolyte (Journal of Materials Chemistry A 3: 6340-6350) Highlighted as Inside back cover

Hoque, M. A., Hassan, F., Higgins, D., Choi, J-. Y., Pritzker M., Knight S., Ye S., and Chen, Z. (2015) Multigrain platinum nanowires consisting of oriented nanoparticles anchored on sulfur-doped graphene as a highly active and durable oxygen reduction electrocatalyst (*Advanced Materials 27 (7) 1229-1234)* Highlighted as Inside front cover

Higgins, D. C., Wang, R., **Hoque, M. A.,** Zamani, P., Abureden, S., Chen, Z. (2014) Morphology and composition controlled platinum-cobalt alloy nanowires prepared by electrospinning as oxygen reduction catalyst *(Nano Energy 10: 135-143)*

Higgins, D. C., **Hoque, M. A.,** Hassan, F., Choi, J-. Y., Kim, B.-J., Chen, Z. (2014) Oxygen Reduction on Graphene-Carbon Nanotube Composites Doped Sequentially with Nitrogen and Sulfur *(ACS Catalysis 4: 2734-2740)*

Higgins, D. C.[†], **Hoque, M. A.**[†], **([†]equal contribution)** Seo, M. H., Wang, R., Hassan, F., Choi, J-. Y., Pritzker M., Yu, A., Zhang, J., Chen, Z. (2014) Development and Simulation of Sulfur-doped Graphene Supported Platinum with Exemplary Stability and Activity Towards Oxygen Reduction (*Advanced Functional Materials 24: 4325-4336)* Highlighted as Frontispiece

Hoque, M. A., Higgins, D., Hassan, F., Choi, J-. Y., Pritzker M., Chen, Z. (2014) Tin oxide - mesoporous carbon composites as platinum catalyst supports for ethanol oxidation and oxygen reduction (*Electrochimica Acta 121:421-427)*

Wang, R., Higgins, D. C., **Hoque, M. A.,** Lee, D. U., Hassan, F., Chen, Z. W. (2013) *Controlled Growth of Platinum Nanowire Arrays on Sulfur Doped Graphene as High Performance Electrocatalyst* **(*Scientific Reports* *3: 2431)***

Patent:

Chen, Z., Yu, A., **Hoque, M. A.,** Hassan, F. (2014) Advanced Graphene Supports for Platinum or Platinum Alloy Nanowire Catalysts and Electrodes for Highly Durable Fuel Cell (US Patent Application No. 61/997,817)

Abstract

The pressing demand for high performance, operationally stable and inexpensive electrocatalyst materials for proton exchange membrane fuel cells (PEMFCs) has spurred significant research and development interest in this field. Until now, fuel cells based on commercially available Pt/C electrocatalysts have not met some of the technical challenges to the widespread commercial adoption of PEMFCs. The main issues associated with the commercial validity of PEMFCs are the high cost and inadequate long term operational stability of Pt/C catalysts typically used to facilitate the inherently sluggish oxygen reduction reaction (ORR). Therefore, the replacement of Pt/C with novel and more effective catalyst materials is critical. These expensive precious metal catalysts make up a large portion of the overall PEMFC stack cost and suffer degradation under harsh potentiodynamic conditions. Therefore, careful electrocatalyst design strategies must be developed to reduce the cost of ORR catalysts with sufficient activity and stability to meet the technical targets set for the use of PEMFCs.

In this work, two approaches are applied to develop new electrocatalyst materials for PEMFCs. The first is to design unique sulfur-doped graphene (SG) and sulfur-doped CNT (S-CNT) supports with the objective of replacing the traditional carbon black to enhance stability toward carbon corrosion. The second is to deposit Pt nanoparticles and nanowires onto SG and S-CNT with the objective of exceeding the activity and stability possible with conventional catalysts. These two catalyst technologies are developed with the ultimate objective of integrating the Pt electrodes into membrane electrode assembly (MEA) to provide excellent PEMFC performance.

The first study focuses on the use of SG prepared by a thermal shock/quench anneal process as a unique Pt nanoparticle support (Pt/SG). These materials are subjected to a variety of physicochemical characterizations and electrochemical investigation for the ORR. Based on half-cell electrochemical testing in acidic electrolyte, Pt/SG demonstrated increased ORR activity and unprecedented stability over the state-of-the-art commercial Pt/C, maintaining 87% of its electrochemically active surface area following accelerated durability testing. Density functional theory (DFT) calculations highlighted that the interactions between Pt and graphene are enhanced significantly by sulfur doping, leading to a tethering effect that can explain the outstanding electrochemical stability. Furthermore, sulfur dopants resulted in a downshift of the Pt d-band center, explaining the excellent ORR activity

and rendering SG as a new and highly promising class of catalyst supports for electrochemical energy technology and PEMFCs.

The beneficial impacts of SG support can be utilized by growing more stable nanostructures such as Pt nanowires on SG to further improve the activity and stability of Pt catalysts. Toward this end, we carried out the direct growth of platinum nanowires on SG (PtNW/SG) by a simple, surfactant free solvothermal technique. The growth mechanism, including Pt nanoparticle nucleation on SG, followed by nanoparticle attachment with orientation along the <111> direction is also highlighted. PtNW/SG demonstrated increased Pt mass activity and a specific activity that is 188% higher than state-of-the-art commercial Pt/C catalysts. Most notably, under a harsh potentiodynamic condition (potential cycles: 3000, potential range: 0.05 to 1.5 V vs RHE), PtNW/SG retained 58% of its electrochemically active surface area and 67% of its ORR activity in comparison to Pt/C that retained less than 1% of its surface area and activity and so failed.

Given the evidence that SG is a promising support for Pt catalysts, the next logical step is to investigate the influence of sulfur on catalytic materials. Accordingly, we study the effects of sulfur on the electrochemical activity and stability of various SG supported platinum nanowires (PtNW/SGs). To investigate the influence of sulfur, a series of SG materials with varying sulfur contents ranging from 0.35 to 3.95 at% are investigated as Pt nanowire catalyst supports. Based on the physico-chemical characterizations, electrochemical measurements and DFT calculations, the amount of sulfur is shown to significantly affect the electrokinetics of the Pt nanowires. The best ORR kinetics are observed for the Pt nanowires supported on graphene with 1.40 at% sulfur. At higher sulfur contents, further enhancements are not observed, and in fact, leads to a loss of activity. At lower sulfur contents, the beneficial role of sulfur does not have a marked impact on performance so that the characteristics and performance more closely resemble that obtained with undoped graphene supports.

Obviously, the beneficial effect of sulfur dopant species can be utilized by doping sulfur into other types of carbon supports such as CNT (S-CNT). Finally, we report on the synthesis, characterization and electrochemical evaluation of S-CNT-supported Pt nanowires (PtNW/S-CNT). PtNW/S-CNT synthesized by a modified solvothermal method demonstrated an increased mass activity and a specific activity 570% higher than state-of-the-art Pt/C. The stability of PtNW/S-CNT is also shown to be very impressive through accelerated degradation testing. Only insignificant changes to the electrochemically active surface area (ECSA, 93% retention) and mass activity (81% retention) of

PtNW/S-CNT are observed over the course of cycling, in contrast to sizable losses observed with commercial Pt/C (<1% retention in ECSA and mass activity) under same conditions.

Acknowledgements

First I would like to thank my supervisors, Professor Zhongwei Chen and Professor Mark Pritzker who provide incredible supports and advices in completing this thesis. I would also like to thank my PhD examining committee including Professor Eric Croiset, Professor Michael Fowler, Professor Hyung-Sool Lee and Professor Di-Jia Liu from Argonne National Laboratory for their contributions throughout this important process.

I would like to thank my parents and my wife for their personal support and great patience at all times. My brother and sister have given me their unequivocal support throughout, as always, for which my mere expression of thanks likewise does not suffice.

The advice, support and friendship of Dr. Fathy Hassan has been invaluable on both an academic and a personal level, for which I am extremely grateful.

Special thanks to all of our group members, current and past, for their support and assistance. I will never forget their kindness and enthusiasm for their research.

I would like to acknowledge the financial, academic and technical support of the University of Waterloo and its staff, particularly in the award of a Graduate Research Studentship and Waterloo Institute for Nanotechnology (WIN) Fellowship that provided the necessary financial support for this research.

Dedication

Dedicated to my beloved parents and my wife.

Table of Contents

List of Figures

List of Tables

Chapter 1 Introduction

1.1 Challenges and Motivation

The search for economically and environmentally sustainable energy sources is very important to meet the growing global energy demand. The continuous depletion of fossil fuels and the negative impact of carbon dioxide emissions on the environment have stimulated the development of alternative clean energy technologies from renewable energy sources. Hydrogen is a promising clean energy source with the potential to replace or reduce the reliance on hydrocarbon fuels and thermomechanical engines. Although hydrogen is produced from non-renewable feedstocks such as natural gas, it can also be produced from renewable energy sources such as wind, solar, hydro and biomass. As an example, hydrogen produced via the electrolysis of water by using electricity generated from the renewable energy sources is free of any impurities and carbon dioxide emissions at the point of use. Due to these advantages, hydrogen is an ideal fuel for developing efficient energy conversion technologies such as fuel cells [1, 2].

Proton exchange membrane fuel cells (PEMFCs) use hydrogen as fuel by oxidizing it to form protons at the anode which are transported to the cathode where they participate in the reduction of oxygen to form pure water as the only by-product. Therefore, PEMFCs are considered sustainable energy conversion devices when operating with hydrogen from renewable resources and forming environmentally benign products at the end. However, several factors such as performance, cost and operational durability must also be considered for the widespread commercialization of PEMFCs. The most expensive part of PEMFCs is the catalyst layer at each electrode that makes up to 55% of the total PEMFC stack cost [3]. The strong reliance on expensive noble metals consisting of platinum nanoparticles dispersed on a high surface area carbon support (Pt/C) is principally responsible for the high cost of PEMFC systems. One of the primary reasons for this reliance on platinum and the high cost of PEMFC arises from the oxygen reduction reaction (ORR) at the cathode due to its very sluggish kinetics compared to that of the anodic hydrogen oxidation reaction (HOR). Thus, relatively high loading of platinum catalyst on the cathode is required. In fact, the slow kinetics of ORR at the cathode leads to severe voltage loss i.e. activation loss that limit the overall performance of PEMFC during operation. Thus, the development of effective cathode catalyst materials is very important in order to enhance ORR kinetics and mitigate voltage losses in PEMFC devices. Furthermore, the challenges associated with the physical, structural and chemical degradation due to the harsh potentiodynamic and oxidizing conditions of fuel cell operation is of high interest for long term

operation of PEMFCs. If not overcome, these challenges will limit the acceptance and attractiveness of PEMFCs due to their short operating lifetimes.

The specified targets for the cost and durability of transportation-based PEMFCs at the stack level set by the US Department of Energy (DOE)[4] is shown in **Table 1-1**. Also included are the requirements for the total amount of electrocatalyst and their mass-based activity (per unit platinum).

Table 1-1 US Department of Energy specified status and target for PEMFC

Characteristics	Units	Targets	
		2011	2020
Power density	W L^{-1}	400	850
Specific power	W kg^{-1}	400	650
Cost	\$ kW^{-1}	49	30
Durability	hours	2500	5000
Pt group metal total loading	mg cm^{-2}-electrode area	0.15	0.125
Mass activity	A mg^{-1} Pt at 0.9 $V_{iR\ free}$	0.24	0.44

Therefore, the aforementioned challenges with ORR electrocatalysts highlight the need to develop innovative material solutions for the development and commercialization of PEMFC systems. Three common approaches are taken in research studies to simultaneously reduce the platinum content and increase stability. These include the development of: (i) unique platinum catalyst supports, (ii) extended surface platinum nanostructures such as nanowires/nanotubes, and (iii) non-platinum group metal (non-PGM) catalysts. It is quite possible that advanced electrocatalyst solutions will comprise a combination of these approaches. Therefore, intensive research efforts, such as those reported within this thesis, are highly warranted for PEMFC implementation.

1.2 Objectives of this work

The approaches to meet the particular project objectives will include the development and investigation of platinum catalysts supported on unique and advanced heteroatom-doped carbon materials. The main objectives include:

1. Development of unique sulfur doped graphene (SG) materials to support platinum nanoparticles (Pt/SG)
2. Apply SG materials to grow advanced platinum nanostructures such as Pt nanowires (PtNW/SG)
3. Optimization of SG supported Pt nanowire catalysts as a function of sulfur concentration and investigation of sulfur influence on catalytic performance
4. Development of sulfur doped CNT (S-CNT) materials to support Pt nanowire catalysts (PtNW/S-CNT) for further catalytic improvement.

1.3 Thesis outline

As already seen, Chapter 1 consists of an introduction relevant to the thesis work and the overall project objectives. Detailed background information on PEMFC systems including history, types of fuel cells and their applications, structure and operational principles, challenges associated with PEMFCs and electrocatalyst technologies will be provided in Chapter 2. In Chapter 3, a detailed description of support material synthesis, platinum nanoparticle deposition and platinum nanowire growth, physicochemical and electrochemical characterization techniques along with the theoretical principles, operation and their application to this thesis will be discussed. The results and discussion of the research activities are included in Chapters 4-7. Chapter 4 describes the development of unique SG materials and their use as platinum nanoparticle supports. Chapter 5 focuses on the growth of platinum nanowires on SG by a simple and facile surfactant-free solvothermal technique. The structure and electrochemical activity of these materials are carefully elucidated and discussed. Further investigation and challenges associated with SG are addressed by developing various SG materials by changing the amount of sulfur in SG supported platinum nanowire catalysts. Detailed results and discussion are provided in Chapter 6. The beneficial impact of extended platinum surface supported by one-dimensional S-CNT are carefully investigated and reported in Chapter 7. Finally, all the results reported within the thesis are summarized in Chapter 8. Chapter 9 provides additional/supporting information associated with the various projects accomplished in this thesis.

Chapter 2 Background and Literature Review

2.1 History of Fuel Cells

Fuel cells produce electricity directly by converting chemical energy of reactants into electrical energy through electrochemical reactions. The concept of fuel cells originated with Sir William Grove in 1839 who demonstrated that electric current could be produced between two Pt strips by placing them in separate bottles containing hydrogen and oxygen that were also filled with dilute sulfuric acid. However, it was only in 1889 when this idea was first applied by Ludwig Mond and Charles Langer who constructed the first practical fuel cell device using industrial coal gas as the fuel and air as the oxidant. However, practical implementation of fuel cells was not possible due to poor understanding of their principles, unreliable fuel resources and the requirement for expensive catalysts. Therefore, fuel cell research focused on laboratory-scale studies to further the basic understanding of the process and solve the associated problems. In 1932, Francis Bacon produced a fuel cell containing an alkaline electrolyte and a nickel electrode based on the previously proposed concept of Mond and Langer. General Electric (GE) produced the first proton exchange membrane fuel cells (PEMFCs) in 1950 that were used by NASA for the Gemini and Apollo space projects. In recent years, the interest of the research community in PEMFCs for sustainable energy production has grown dramatically due to the huge consumption of fossil fuels and increasing concerns about carbon dioxide emissions.

2.2 Types and Applications of Fuel Cells

In a PEMFC, the anode and cathode are separated by an electrolyte and hydrogen or hydrocarbons are used as fuel to be anodically oxidized, while pure oxygen or air is cathodically reduced. Regardless of the type of charge carrier in the fuel cell, the liberated electrons at the anode pass through the external circuit to the cathode. Thus, due to the difference in chemical potential, electric current is obtained when a load is applied. The most common types[5] of fuel cells with their intrinsic operating characteristics are shown in **Table 2-1**.

Table 2-1 Characteristics of five major types of fuel cells

Characteristics	PEMFC	PAFC	AFC	MCFC	SOFC
Electrolyte	Polymer membrane	Liquid H3PO4	Liquid KOH	Molten carbonate	Ceramic
Charge carrier	H^+	H^+	OH^-	CO_3^{2-}	O^{2-}
Operating temperature	80°C	200°C	60-220°C	650°C	600-1000°C
Catalysts	platinum	platinum	platinum	Nickel	Perovskites (ceramic)
Cell components	Carbon based	Carbon based	Carbon based	Stainless based	Ceramic based
Fuel compatibility	H_2, methanol	H_2	H_2	H_2, CH_4	H_2, CH_4, CO
Applications	Electric utility, portable power, transportation	Electric utility, transportation	Military, space	Electric utility	Electric utility, auxiliary power

2.2.1 Proton exchange membrane fuel cells (PEMFCs)

PEMFCs contain a polymer membrane that allows transport of protons to the cathode after being produced at the anode by hydrogen oxidation. These protons then participate in the oxygen reduction reaction and produce pure water as the only by-product. The polymer membrane (ionomer) which is very thin (thickness of ~ 20 um) is crucial for PEMFCs to achieve high power density. The operating temperature of PEMFC also has a significant impact on the durability of polymer membranes due to the effects of thermal degradation. The commonly used Nafion membranes made from perfluorinated sulfonic acid (PFSA) can operate at temperatures below 100°C and provide excellent proton conductivity. Moreover, PEMFCs are scalable, versatile and can be applied for a wide range of stationary, portable and transportation applications in the range of 10 W to 1 MW.

Direct methanol fuel cells (DMFC) are a class of PEMFCs using methanol that is easy to store and handle as a fuel at the anode and is oxidized in the presence of precious metal catalysts. The polymeric membrane used in DMFCs is a bit thicker than those used when hydrogen is the fuel to avoid methanol crossover, although this lowers efficiency or power density. The class of DMFCs also includes other fuel cells such as direct ethanol fuel cells which are more reliable and promising.

2.2.2 Phosphoric acid fuel cells (PAFCs)

Highly concentrated or pure liquid phosphoric acid (H_3PO_4) serves as an electrolyte for PAFCs. High temperature operation (200°C) makes PAFCs more tolerable to CO poisoning and so requires less purification of the hydrogen fuel. The electrochemical reactions are similar to those operating in

PEMFCs and also require platinum-based catalysts. However, the challenges associated with PAFCs such as an aggressive electrolyte at high temperature, low start-up and low power density must be considered before being used for practical applications.

2.2.3 Alkaline fuel cells (AFCs)

Alkaline fuel cells use aqueous potassium hydroxide (KOH) as the electrolyte generally as a 6M solution operating at temperatures varying from 20 to 90°C. Hydroxyl ions (OH^-) travel from the cathode to the anode in a direction opposite to PEMFCs. The electrochemical reactions involved in AFCs are as follows:

anode: $H_2 + 2OH^- \rightarrow 2H_2O + 2e^-$ (2-1)

cathode: $O_2 + 2H_2O + 4e^- \rightarrow 4OH^-$ (2-2)

overall: $2H_2 + O_2 \rightarrow 2H_2O$ (2-3)

The theoretical energy efficiency of these fuel cells is 83% with a thermodynamic cell voltage of 1.23 V at 25°C. Oxygen reduction kinetics is faster in alkaline solution than in acidic medium where PEMFCs operate. Despite many advantages, the main drawback of AFCs is electrolyte poisoning by CO_2 in the air when used as a fuel in anode. However, renewal of the electrolyte or use of pure oxygen can mitigate the formation of undesired carbonates to make AFCs more reliable during operation.

2.2.4 Molten carbonate fuel cell (MCFC)

MCFCs operate at high temperature (600°C or higher) and so expensive precious metal catalysts can be substituted with inexpensive non-precious materials such as nickel. The electrolyte used is composed of a molten carbonate salt (sodium or lithium) suspended in porous and inert beta-alumina solid electrolyte. MCFCs have significant advantages over PAFCs in that they are cheaper, more efficient and do not require externally supplied hydrogen since they are capable of internal reforming of coal. Also, MCFCs are not susceptible to poisoning by CO_2 that is transported to the cathode along with the oxidizer. In fact, CO_2 can be included in the fuel with gases obtained from coal. However, start-up issues and durability of MCFCs strongly limit their large-scale applications.

2.2.5 Solid oxide fuel cells (SOFCs)

SOFCs make use of ceramic or solid oxide electrolytes such as yttria-stabilized zirconia (mostly used), scandia-stabilized zirconia and gadolinium-doped ceria that conduct O^{2-} from the cathode to the anode. SOFCs operate at very high temperature (up to 1000°C) allowing the replacement of

expensive platinum catalysts with cheap perovskites or nickel catalysts. Also, high temperature operation of SOFCs makes them suitable for combined heat and power (CHP) systems. Despite other advantages such as low cost, durability, high efficiency, fuel flexibility and low emissions, SOFCs suffer from slow start-up during high temperature operation.

2.3 Thermodynamics and Kinetics of Fuel Cells

2.3.1 Thermodynamics of fuel cells

Fuel cells convert the chemical energy of reactants into electricity. Its energy efficiency can be defined by the ratio of change in Gibbs free energy (ΔG_r) to the change in total enthalpy (ΔH_r) for a certain chemical reaction. In the case of H_2/O_2 PEMFCs which make use of the overall reaction

$$H_2 + \ ½\ O_2 \rightarrow \ H_2O \tag{2-4}$$

ΔG_r and ΔH_r are −237 and −287 kJ/mole, respectively, at standard condition of 25°C and 1 atm P_{H2} and 1 atm P_{O2}. Based on these values, the maximum conversion efficiency that can be achieved is 83% which exceeds the level possible with any other current energy conversion devices.

At constant temperature and pressure, the maximum electrical work obtainable by converting the free energy of the electrochemical reaction is:

$$E_r \ = \ -\frac{\Delta G_r}{nF} \tag{2-5}$$

where n is the number of electrons transferred and F is the Faraday constant (96485 C mol^{-1}). By using these data, the cell voltage obtained for the H_2/O_2 PEMFC at standard conditions is therefore E^0 = 1.23 V SHE. The temperature dependence of the cell voltage E_r can be estimated by the following equation:

$$E_r(T) = \ E_r^0(298) + \frac{\Delta S_r^0}{nF}(T - 298) \tag{2-6}$$

Given that ΔS_r^0 is −163 J mol^{-1} K^{-1}, E_r^0 for an H_2/O_2 PEMFC operating at 80°C has a value of 1.18 V SHE. Again, the relationship between the activity of reactants and products and the Gibbs free energy can be written as:

$$\Delta G_r = \Delta G_r^0 + RT\ ln\frac{\prod_i a_{i,prod}}{\prod_i a_{i,react}} \tag{2-7}$$

The cell voltage E_r of the PEMFC can be related to the activities of reactant and products by the following equation

$$E_r = E_r^0 + \frac{RT}{nF}\, ln \frac{a_{H_2} a_{O_2}^{1/2}}{a_{H_2O}} \tag{2-8}$$

The temperature and activity dependencies of the cell voltage can be combined to yield:

$$E_r(T) = E_r^0(298) + \frac{\Delta S_r^0}{nF}(T - 298) + \frac{RT}{nF}\, ln \frac{a_{H_2} a_{O_2}^{1/2}}{a_{H_2O}} \tag{2-9}$$

or

$$E_r(T) = E_r^0(298) + \frac{\Delta S_r^0}{nF}(T - 298) + \frac{RT}{nF}\, ln \left(\frac{P_{H_2}}{P^0}\right)\left(\frac{P_{O_2}}{P^0}\right)^{1/2} \tag{2-10}$$

where P^0 is the standard pressure (1 atm).

2.3.2 Kinetics of fuel cells

Butler-Volmer equation can be employed to describe the kinetics of the electrochemical reactions associated with fuel cells. The relationship between the current density i (A cm^{-2}) for a half-cell reaction and the overpotential η (V) is as follows:

$$i = i_0 \left[exp\left(\frac{\alpha nF}{RT}\eta\right) - exp\left(-\frac{(1-\alpha)nF}{RT}\eta\right)\right] \tag{2-11}$$

The kinetics for each reaction occurring at an electrode in a fuel cell can be described by its own Butler-Volmer equation. The overpotential η is the difference between the potential of an electrode and the equilibrium potential for the given half-cell reaction and is a measure of the deviation from the reaction equilibrium. When a half-cell reaction is at equilibrium, it proceeds in the anodic direction at the same rate as it does in the cathodic direction. The exchange current density i_0 (A cm^{-2}) is the current density corresponding to this rate when the electrochemical reaction is at equilibrium. The exchange current density is an intrinsic property of electrode materials and is used as an important tool to measure the activity of a catalyst for a certain reaction. In the above equation, α is the transfer coefficient and is related to the inverse of the Tafel slope $(2.303\, RT/n\, \alpha F)$ and can be obtained experimentally. The transfer coefficient is an important parameter to evaluate the mechanism of an electrode reaction.

Under typical operating conditions, the magnitude of the overpotential at each electrode is larger than 0.1 or 0.2 V. In this situation, the rate of the backward direction of the reaction at each electrode usually is negligible compared to the rate of the forward direction and the Butler-Volmer equation for the reaction at each electrode can be simplified as follow:

$$i_a = i_{0,a}\, exp\left(\frac{\alpha_a n_a F}{RT}\eta_a\right) \tag{2-12}$$

$$i_c = -i_{0,c}\, exp\left(-\frac{\beta_c n_c F}{RT}\,\eta_c\right) \tag{2-13}$$

Some of the parameters in the expressions are identified with subscripts a and c to signify that they are associated with the anodic and cathodic reactions, respectively. An example of plots of i_a and i_c versus the overpotential is presented in **Figure 2-1a**. The effect of i_0 on the electrode response is shown in **Figure 2-1b** and reveals that an increase in the exchange current density leads to a higher current density at a given overpotential. Equations (2-12) and (2-13) can be re-arranged to give the so-called Tafel equations for the anodic and cathodic reactions:

$$\eta_a = \frac{2.303\,RT}{\alpha_a n_a F}\, log\left(\frac{i_a}{i_{0,a}}\right) \tag{2-14}$$

$$\eta_c = -\frac{2.303\,RT}{\beta_c n_c F}\, log\left(\frac{|i_c|}{i_{0,c}}\right) \tag{2-15}$$

Semi-log plots of i_a and i_c versus the overpotential according to Equations (2-14) and (2-15) are shown in **Figure 2-1c**. The slopes of these plots are known as the Tafel slopes and are given as $\frac{2.303\,RT}{\alpha_a n_a F}$ and $-\frac{2.303\,RT}{\beta_c n_c F}$ for the anodic and cathodic reactions, respectively. The magnitude of the Tafel slope for the ORR typically has a value in the range of 0.04 to 0.12 V/dec depending on the reaction mechanism, electrode material, structure, surface condition and temperature. It should be noted that a decrease in the Tafel slope leads to an increase in the current density and improvement in fuel cell performance.

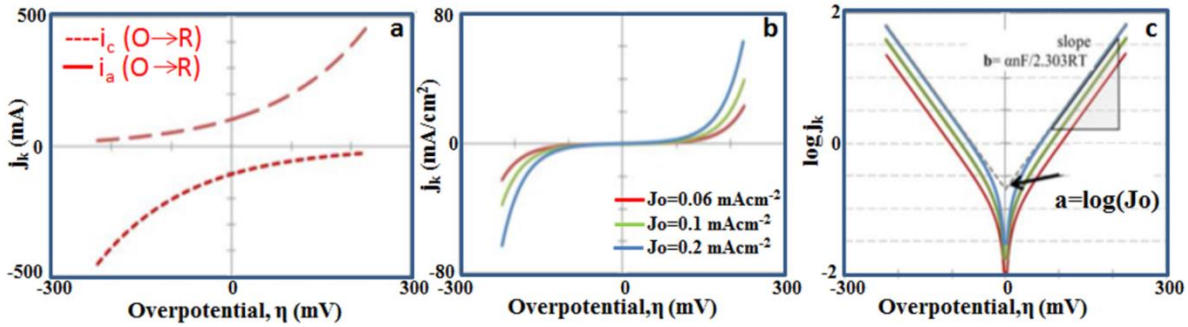

Figure 2-1 Diagrams depicting (a) J_k vs **η** (b) the effect of i_0 (=J_0) (c) determination of i_0 (=J_0) and b.

2.4 Introduction to Polymer Electrolyte Membrane Fuel Cells (PEMFCs)

2.4.1 Structure of PEMFCs

PEMFCs were first developed by General Electric in the early 1960s as an alternative to alkaline fuel cells. PEMFCs are very attractive for low temperature operation, more environmentally benign and more efficient compared to other fuel cell technologies. **Figure 2-2** shows the three major components (anode, cathode and membrane) of a typical H_2/O_2-based PEMFC. The polymeric membrane sandwiched between the two electrodes is capable of conducting protons from anode to cathode. A catalyst layer based on platinum is used in both the anode and cathode in order to accelerate the electrochemical reactions at the interface between the membrane and electrodes. At the anode, the protons generated by the splitting of H_2 diffuse across the membrane to the catalyst layer in the cathode and combine with O_2 to produce pure water only. At the same time, the transport of electrons from anode to the cathode in the external circuit generates electricity.

The most commonly used polymer electrolyte membrane is perfluorinated sulfonic acid (PFSA), developed by Dupont and consists of a tetrafluoroethylene backbone with perfluorovinyl ether side groups terminated by sulfonate moieties. The chemical structure of the Nafion membrane is also included in **Figure 2-2**. The sulfonated groups in this material are responsible for conducting protons by the hopping mechanism. At the same time, the membrane prevents the passage of electrons and any short circuit recombination of protons and electrons from occurring.

Catalyst surface area is a key factor to obtain the maximum current by enhancing the electrochemical reactions in the electrodes. Thus, Pt nanoparticles with high surface/volume ratio are utilized in order to increase the surface area and minimize the required amount and cost of the catalyst. On the other hand, the high surface energy of Pt nanoparticles tends to cause them to aggregate and reduce their surface area significantly over time. To overcome this aggregation problem, high surface area carbon is used to disperse and stabilize Pt nanoparticles and to provide highly conductive channels between the catalysts and the current collector. Catalyst materials are usually dispersed in a highly porous carbon paper known as the gas diffusion layer at both the anode and cathode. Normally, the two electrodes and the membrane are combined together in a single unit called the membrane electrode assembly (MEA). The MEA is then sandwiched between two bipolar plates which are made of carbon, graphite or stainless steel due to having their distinct mechanical properties, electrical conductivity and corrosion resistivity. These bipolar plates must meet a number of important

requirements: satisfactory electrical conductivity, mechanical strength to maintain the intrinsic shape and structure of the fuel cell and fast removal of the waste heat produced by the fuel cell reactions.

The reactions involved in a H_2/O_2-based PEMFC are as follows:

Anode: $H_2 \rightarrow 2H^+ + 2e^-$ $E^o = 0$ V vs. RHE (2-16)

Cathode: $\frac{1}{2} O_2 + 2H^+ + 2e^- \rightarrow H_2O$ $E^o = 1.229$ V vs. RHE (2-17)

Overall reaction: $H_2 + \frac{1}{2} O_2 \rightarrow H_2O$ $E^o = 1.229$ V vs. RHE (2-18)

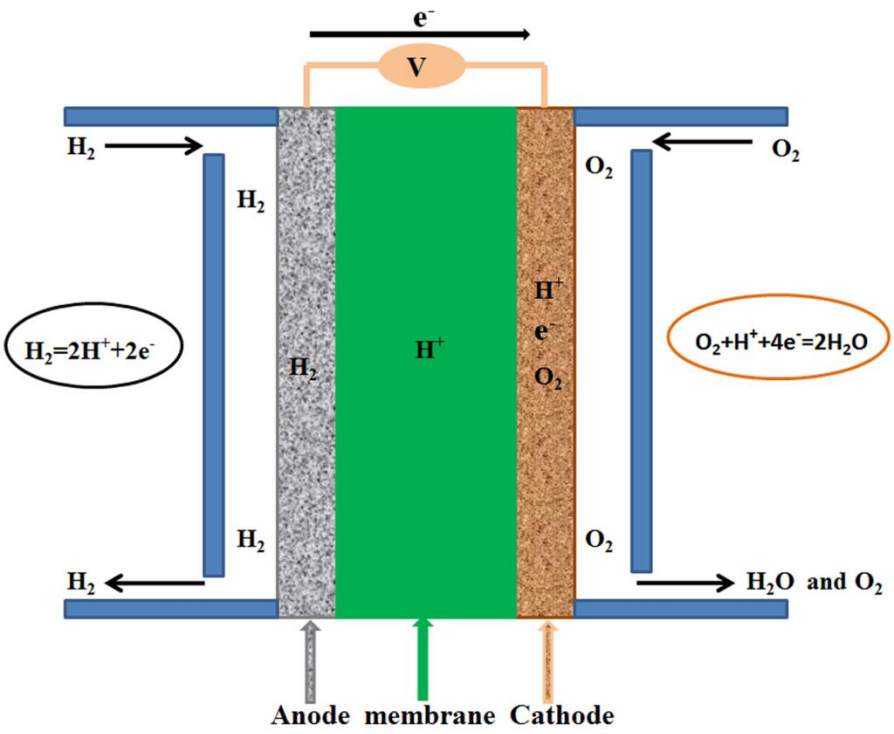

Figure 2-2 Schematic diagram of a H_2/O_2 PEMFC.

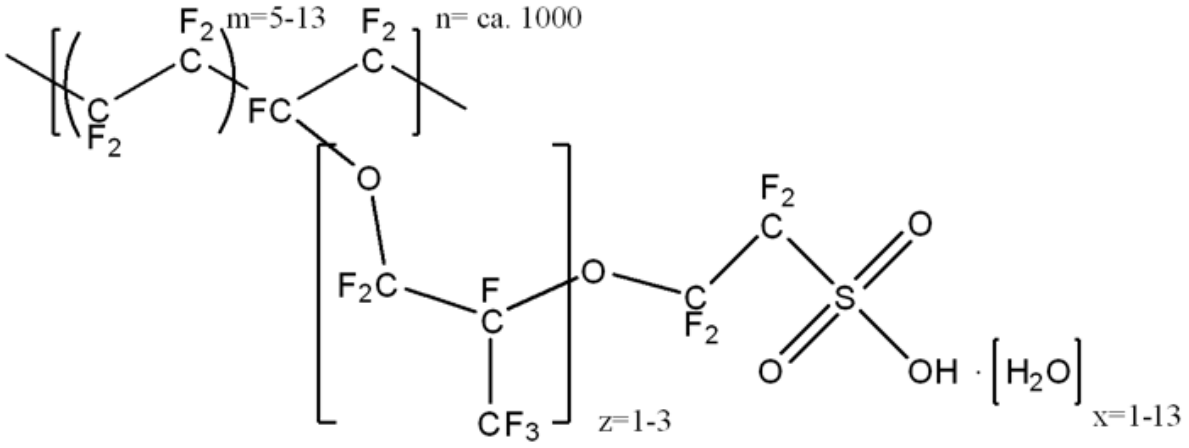

Figure 2-3 Chemical structure of Nafion(R) membranes used in PEMFCs.

2.4.2 Challenges of PEMFCs

Although H_2/O_2 PEMFCs have a theoretical cell voltage of 1.229 V, the voltages observed during operation are always significantly lower than this value. This is due to irreversible voltage losses during operation. Typically, the most significant loss is attributed to slow cathode kinetics associated with the ORR. The HOR at the anode proceeds with a high exchange current density (3-10 mA cm^{-2}) and so causes only a very minor loss (<10 mV) to the cell voltage. On the other hand, the exchange current density of the ORR is lower (0.5-1.5 mA cm^{-2}) and so leads to significant activation losses (approximately 300 mV). **Figure 2-3** presents a typical polarization curve for a PEMFC highlighting the different losses and indicating that ORR kinetics contributes 70% of the total losses of an operating fuel cell [6].

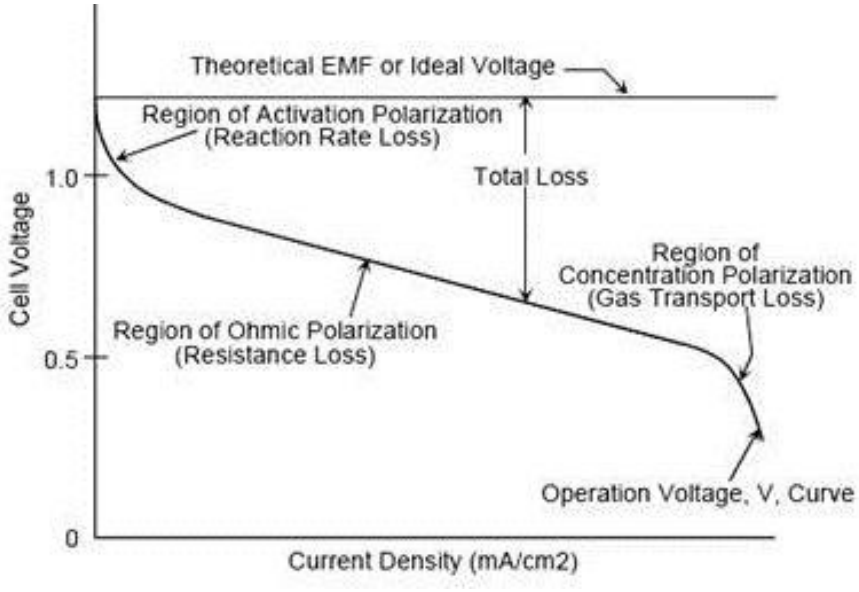

Figure 2-4 A typical PEMFC polarization curve, showing contributions of losses.

As shown in **Figure 2-3**, the losses in cell performance can be divided into the following regions as the operating current is raised: (i) mixed-potential losses, (ii) activation losses primarily due to cathode reaction kinetics, (iii) ohmic resistance and (iv) mass transport limitations.

Mixed potential losses:- The open-circuit voltage (OCV) of 1.15 V at 80°C is lower than the reversible value of 1.23 V H_2/O_2 due to mixed potential losses related to fuel cross-over, short circuiting and oxidation of the catalyst materials in the cathode. Possible secondary reactions that occur at the cathode and lower the OCV are described below:

1. Cathode oxidization can occur due to a slight permeability of the PEM electrolyte to H_2 gas. This enables some H_2 to cross over to the cathode where it can oxidize due to the high potential and thereby decrease the overall cell potential by ~25-90 mV. Obviously, membrane thickness and permeability have a large effect on the decrease in OCV.
2. Reversible adsorption of oxygen-containing species at the surface of the catalyst at the cathode can lead to a reaction between Pt and PtO and losses of ~90-190 mV:

$$Pt + H_2O = PtO + 2H^+ + 2e^- \qquad (2\text{-}19)$$

(i) Activation loss:- Activation losses arise from limitations to the kinetics of the electrochemical reactions of the electrodes. As mentioned previously, sluggish ORR kinetics at the cathode is the most important and detrimental cause of the voltage drops in a PEMFC. The exchange current density of this reaction is only 0.5 to 1.5 mA cm^{-2}. As a result, the ORR exhibits a large overpotential (~300 mV)

even in the presence of the most active Pt-based catalysts. Thus, considerable scope exists to design effective nanostructured catalysts on advanced carbon materials in order to reduce the voltage losses and so is a primary objective of the research community.

(ii) Ohmic loss:- The ohmic losses in PEMFCs arise from the bulk electrical resistance of the cell materials, cell connections (bipolar plates, catalyst layers, current collector cables etc.) and the resistance to H^+ transport in the polymer electrolyte. By using appropriate materials including electrode structures with high conductivity, these losses can be maintained small.

(iii) Mass transport limitation:- In this situation, the rate at which reactants are replenished at the electrode surface cannot keep pace with the rate at which they are consumed by the electrode reactions. When this limitation becomes severe enough, the surface concentration of the reactant is driven to zero and the current density reaches a limiting value. No further increase in current is possible under the given operating conditions. Reactant concentration, feed flow rates, cell temperature and the structure of the gas diffusion and catalyst layers are the primary factors that influence mass transport and determine the limiting current density of a PEMFC.

2.5 Electrocatalyst Stability Limitations

Activation voltage loss at the cathode due to sluggish ORR kinetics is perhaps the most significant and critical problem preventing widespread commercialization of PEMFCs. Thus, catalyst materials have a direct impact on the activation voltage loss and the overall performance of PEMFC devices. The current status of electrocatalyst technology strongly relies on very expensive platinum nanoparticles that are well dispersed on a high surface area carbon support, commonly known as Pt/C. Besides the high cost and the slow rate of the ORR, another challenge for operating PEMFCs is their durability due to the limited stability of platinum catalysts. The combined effects of potentiodynamic cycling, start-up and shut-down, the nature of the polymeric membrane, humidity and elevated temperature create a harsh environment for the electrocatalyst and cause its degradation and loss of performance loss over time. The specific reasons for the degradation of the Pt/C electrocatalyst are (i) carbon corrosion, (ii) platinum nanoparticle dissolution and/or agglomeration and (iii) catalyst contamination and poisoning.

The oxidation/corrosion of carbon is thermodynamically favoured under normal operating conditions with a standard equilibrium potential of 0.207 vs RHE.

$$C + 2H_2O \rightarrow CO_2 + 4H^+ + 4e^- \quad (2\text{-}20)$$

Although the cathode potential is normally high enough to drive direct oxidation/corrosion of carbon, platinum has been found to catalyze carbon oxidation. Humidity, temperature and the amount of carbon also influence carbon corrosion [7, 8]. Obviously, carbon corrosion is very detrimental towards the long term operation of fuel cells and must be mitigated. The most common approaches investigated in recent research to slow down carbon corrosion have been to replace the traditional carbon black with highly graphitized carbon such as graphene or carbon nanotubes.

The dissolution and/or agglomeration of platinum nanoparticles play a key role in degrading PEMFC performance. Since platinum nanoparticles are very small in size (2-3 nm), they have very high surface energy that promotes migration and agglomeration into larger particles to reduce the surface energy. This phenomenon is known as Ostwald ripening and can occur via the following pathways: (i) migration of platinum ion through the ionomer layer in the catalyst and (ii) platinum dissolution and subsequent deposition on neighboring particles. **Figure 2-4** shows TEM images of Pt/C in fresh and used states providing clear evidence of platinum agglomeration after 200 hours of operation in a 10 cell PEMFC stack [9]. Several techniques studied to overcome this detrimental phenomenon are (i) design and development of unique support materials that can strongly tether to platinum nanoparticles and inhibit their dissolution and agglomeration (ii) fabrication of controlled and more stable platinum nanostructures such as nanowires.

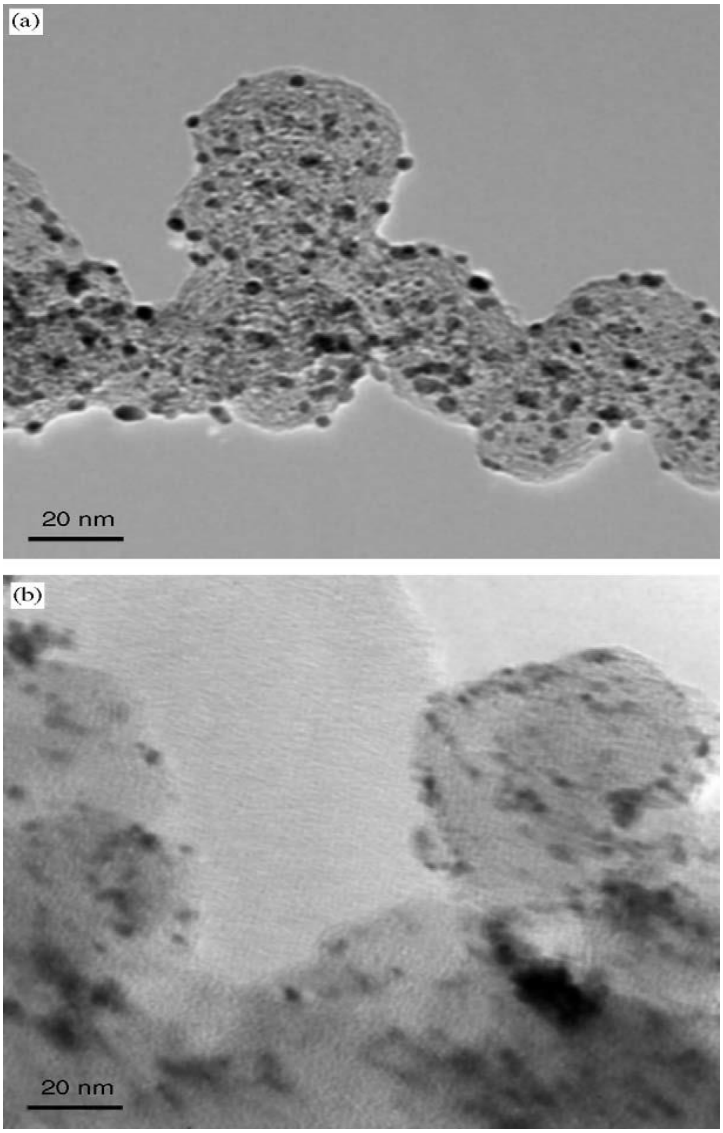

Figure 2-5 TEM micrographs of the fresh Pt/C catalyst (a) and the degraded catalyst after 200 hours.

2.5.1 Nano-structured carbon supports

The main objective in PEMFC development is to reduce the cost and improve the performance and durability of materials. Design of improved carbonaceous electrocatalyst supports is one of the approaches to achieve these goals. It is well known that supported metal catalysts exhibit superior activity and stability than unsupported metal catalysts. An ideal support should possess good electrical conductivity, good catalyst-support interaction, large surface area, ability to maximize the triple phase boundary, good water handling capability to avoid flooding and good corrosion resistance

[10]. Thus, the choice of support material is very important in determining performance, durability and cost effectiveness of the catalysts and the overall fuel cell performance. Traditionally, highly conductive electrocatalyst supports have been based on carbon blacks with high surface area such as Vulcan XC-72R (Cabot corp. 250 m^2 g^{-1}), Shawinigan (Chevron, 80 m^2 g^{-1}), Black pearl 2000 (BP2000, Cabot corp. 1500 m^2 g^{-1}), Ketjen Black (KBEC600JD & Ketjen International, 1270 m^2 g^{-1} and 800 m^2 g^{-1}, respectively) and Denka Black (DB, Denka, 65 m^2 g^{-1}).

Carbon blacks, especially Vulcan XC-72R, are the most widely used supports for platinum and platinum alloy catalysts in fuel cells and are produced from the pyrolysis of hydrocarbons. Carbon black (CB) particles are nearly perfectly spherical in shape with a size < 50nm and grow to approximately 250 nm when they aggregate and agglomerate. CB has a polycrystalline structure consisting of several turbostratic layers with an interplanar spacing of 0.35-0.38 nm. The process of thermal decomposition and the source material greatly affect the morphology and particle size distribution of CB [11]. Despite having a high surface area and being a widely used support material, the use of CB suffers from a number of problems: (i) the presence of organo-sulfur impurities, (ii) deep micropores which trap the catalyst nanoparticles and make them inaccessible to reactants leading to a reduction of catalyst activity and (iii) thermochemical instability leading to the corrosion of CB which is severe and the loss of active catalyst material from the surface. The interaction between the Nafion$^{(R)}$ ionomer and the catalyst nanoparticles is affected by the CB pore size and distribution. Since the typical size of Nafion$^{(R)}$ micelles (> 40 nm) is much larger than that of CB micropores, many metal nanoparticles in recesses or micropores become inaccessible to the electrolyte and therefore make no contribution to the electrochemical activity This has led to research into a multitude of materials other than carbon blacks as support materials with unique and stable nanostructure, as discussed below.

Mesoporous carbon: Mesoporous carbon materials are a class of porous carbon materials that have a high electrical conductivity and high surface area with pore sizes in the range 2 – 50 nm. Two types of mesoporous carbon exist based on the structure and method of preparation. The first one is ordered mesoporous carbon (OMC), while the second is disordered mesoporous carbon (DOMC) which has an irregularly interconnected structure and thus a lower conductivity and wider pore size distribution than OMC. OMCs are generally prepared by using ordered mesoporous silica or triblock copolymer template structures [12]. The structure of the carbon support determines the access of reactants to the catalytic sites and the removal of the products which have strong effects on electrocatalyst

performance. OMCs have very interesting morphological structures with high surface area and three-dimensionally connected mono-dispersed mesopores which help to facilitate the diffusion of reactants and by-products. OMCs also contain some surface oxygen groups that improve the interaction between the catalyst and support and so improve catalyst dispersion. Many researchers have shown that platinum nanoparticles supported on ordered mesoporous carbon such as CMK-3 exhibit superior ORR activity due to the uniformly dispersed nanoparticles, more electrochemically active sites and higher electrochemical active surface area [13]. ORR activity improvement was attributed to the highly ordered structure and good 3D interconnection of the hexagonally arranged carbon nanorods that enable higher catalyst utilization. Pore morphology, pore structure and surface chemistry were also deemed to play key roles [13]. As an example, platinum supported by ordered mesoporous carbon CMK-3 has been found to be a promising catalyst for alcohol oxidation in DMFCs [14]. Surface functionalization or modification and doping of OMCs can also significantly improve electrocatalytic activity, stability and resistance to fuel crossover.

Graphene: Graphene is a flat monolayer of hexagonally arranged carbon atoms tightly packed into a two-dimensional (2D) honeycomb lattice [15]. This material has been widely studied for many applications including fuel cell catalyst supports due to its high electron transfer rate, large surface area and high conductivity [16]. Catalyst nanoparticles can interact with the edge and basal planes of the 2D planar carbon sheets. Since these sheets are actually rippled, they have a very high surface area to strongly attach to catalyst nanoparticles. Graphene enables very fast electron transport that facilitates the ORR in fuel cells [17] and has a band gap equal or close to zero [18]. High quality graphene can be synthesized by micromechanical exfoliation, epitaxial growth and CVD. Among the synthesis procedures, CVD has distinct advantages for obtaining highly exfoliated large surface area graphene from graphene oxide (GO). The GO used is normally obtained by the modified Hammers method and then placed inside a furnace for annealing at high temperature (800-1000^{o}C) in the presence of Ar. The catalytic properties of graphene can be further improved by doping with heteroatoms such as boron, phosphorous, nitrogen or sulfur to provide more active sites and tuning their band gaps [19].

Carbon nanotubes (CNTs): CNTs are 1D nanostructures generally formed from rolled up single sheets of hexagonally arranged carbon atoms. CNTs can be single-walled (SWCNT) or multi-walled (MWCNT). Depending on the synthesis procedure and desired properties, SWCNTs or MWCNTs are used as carbon nanostructures for application as catalyst supports in fuel cells [20]. SWCNTs tend to provide more surface area while MWCNTs are usually more conductive. MWCNTs can have

diameters of a few tens of nanometers with a spacing of ~0.34 nm between the cylindrical walls. However, since CNTs are chemically inert, it is difficult to attach them to catalyst nanoparticles. To solve this problem, it is necessary to functionalize the surfaces of CNTs, for example, by the use of a strong oxidizing agent in order to make the surface more hydrophilic and improve the catalyst support interaction [21]. The use of CNTs as a support material enables better catalyst nanoparticle dispersion, controlled size distribution and selective morphologies. CNTs are strongly resistant to corrosion and allow good catalyst activity to be maintained for longer periods of fuel cell operation than that possible using commercial carbon black [22]. Moreover, CNTs can also be doped with heteroatoms in order to alter and improve their intrinsic catalytic properties.

Carbon nanofibers (CNFs): Carbon nanofibers (CNFs) have also been extensively studied as promising supports for fuel cell catalysts [23]. Unlike CNTs, CNFs have either a very thin or no hollow cavity and are much larger than CNTs with diameters as high as 500 nm and lengths up to a few millimeters. Three types of CNFs have been observed – ribbon-like, platelet and herringbone CNFs. Herringbone CNFs show very promising activity and durability compared to the other types of CNFs. Although CNFs have lower surface area and pore volume than carbon black, they display better catalytic activity [24]. Moreover, they can be functionalized or acid-treated to improve their performance as a support material. The most important difference between CNTs and CNFs is that only edge planes are exposed in the case of CNFs, whereas the basal plane is primarily exposed in the case of CNTs. The much larger area associated with the basal plane makes CNTs a better choice as a catalyst support for fuel cell applications.

2.5.2 Doping of nanostructured carbon materials

The introduction of heteroatoms such as B, P, N and S into nanostructured carbon frameworks is very effective in modifying their electrical properties and chemical activities [25-29]. Recent studies have shown that N-doped carbon materials such as CNTs, graphene and mesoporous graphitic arrays exhibit high catalytic activity, long term durability and excellent methanol tolerance. Furthermore, these materials are relatively inexpensive and environmentally friendly. The excellent catalytic activity toward the ORR has been attributed to the areas of positive charge density on adjacent carbon atoms due to the electronegativity of N (electronegativity of N: 3.04) which is favorable for O_2 adsorption. Moreover, carbon materials doped with B and P (electronegativity of B: 2.04, electronegativity of P: 2.19 respectively) also showed pronounced catalytic activity. On the other hand, S-doped carbon materials have rarely been investigated for catalytic applications [30]. It is

important to note that the electronegativity of S is close to that of carbon (electronegativity of S: 2.58 and electronegativity of C: 2.55). The introduction of S atoms into nanostructured carbon materials stabilizes their structure and improves their electrical properties significantly. It was found that the formation energy for S-doped SWCNT is at least 0.7 eV larger than its N-doped counterpart and the formation energy can even be increased to 1 eV for graphene with S-substitutional defects [25]. Therefore, these materials may be effective as catalyst support materials in fuel cells by adjusting the amount of S incorporated to modulate the electronic properties of the sheets and using S atoms to anchor platinum nanoparticles or nanowires. Due to these potential benefits, S-doped graphene and S-doped CNT are extensively investigated throughout this project.

2.5.3 ORR electrocatalyst technologies

The potential uses of unique heteroatom doped nano-structured carbon supports for platinum nanostructures such as nanoparticles and nanowires, are discussed in the following section.

(i) Platinum nanoparticles supported on S-doped graphene (Pt/SG)

As stated previously, support materials have direct impact on the ORR and so the selection of suitable support materials is very important to obtain the highest catalytic activity and stability. The properties of an ideal support include high surface area, excellent electronic conductivity, chemical stability, favorable catalyst-support interaction and strong cohesive bond to the active materials. Support materials also affect the interaction with the ionomer in the catalyst, electrode architecture and properties. In order to achieve favorable nanostructures, the factors leading to the formation of triple points, excellent mass transport of reactants, proper catalyst nanostructure are of great interest [31]. Surface properties of the support materials directly influence the utilization of platinum materials and good dispersion of platinum nanoparticles. In general, platinum nanoparticles are deposited onto a support by chemical reduction. In this method, chloroplatinic acid hexahydrate is reduced by ethylene glycol or sodium borohydrate to form nanosized platinum metal particles. The high density of π electrons in the carbon-based support material provides necessary anchoring sites for nucleation and growth of the platinum nanoparticles [32]. Common carbon supports used in Pt/C often do not exhibit satisfactory stability and therefore new and improved configurations are required to obtain the desired PEMFC durability. Furthermore, the cohesion between platinum and the support material should be strong enough to hinder platinum migration, agglomeration and dissolution that greatly reduce the material durability. Moreover, the interaction energy between platinum and support affects the strength of the tethering of platinum to the support. Thereby, it should be possible to tailor PEMFC

performance by developing novel catalyst support materials with favorable physicochemical properties and catalyst-support interactions.

Graphene has recently emerged as a highly promising catalyst support material for PEMFC applications due to its immense surface area, excellent conductivity and electron transfer capabilities that are important criteria pertaining to electrocatalysis [33-35]. Graphene is theoretically composed of only graphitic carbon atoms which can provide added resilience against carbon corrosion during PEMFC operation,[36] However, the relatively inert and hydrophobic nature of its surface does not culminate in facile Pt deposition and so it must be functionalized to obtain well dispersed nanoparticles and overcome stability limitations [37]. To this end, nitrogen-doped graphene and other graphitic carbons have been extensively developed and investigated for fuel cell catalyst applications, either as stand-alone ORR electrocatalysts in alkaline media[38-46] or as Pt nanoparticle supports under acidic (i.e. PEMFC) conditions.[47-53] The presence of nitrogen dopants has been reported to promote the tethering of Pt nanoparticles, benefiting both catalyst activity and stability [53, 54]. While density functional theory (DFT) simulations have been carried out to investigate the adsorption and binding interactions between Pt and either nitrogen- and boron-doped graphene or CNTs, [55-58] a fundamental understanding of the interaction between Pt and heteroatom-doped graphene catalyst-support and their associated impact on ORR performance and operational stability is still lacking. Furthermore, the impact of graphene doped with various other heteroatoms (e.g., sulfur) remains largely unexplored despite their high potential for applications such as ORR catalysis [19, 59, 60] or catalyst support materials[61]. The elucidation of these important considerations can be provided by linking fundamental computational simulations with detailed experimental investigations.

(ii) Platinum nanowires supported on S-doped graphene (PtNW/SG)

One dimensional platinum nanowires have unique morphology and distinct advantages with respect to ORR activity and stability. Ultrathin platinum nanowires possess unique photonic, electronic, magnetic and catalytic properties. The anisotropic nature of platinum nanowires enables superior stability in fuel cells compared to zero-dimensional platinum nanoparticles. The distinct properties of platinum nanowires include (i) high catalyst utilization due to enhanced reactant/product mass transport properties, (ii) high aspect ratio and (iii) micrometer-scale length that mitigates platinum dissolution and agglomeration due to lower surface energy relative to that of platinum nanoparticles [62-64]. The synthesis of platinum nanowires is based on the use of templates or substrates such as biomaterials, carbon nanotubes, block copolymers and other mesoporous materials to guide the

growth and formation of nanowires. However, the requirements for template removal and scale-up hinder the use of platinum nanowires in commercial applications and therefore, create great challenges for the direct synthesis of platinum nanowire. Although researchers have shown that surfactant- or ligand-assisted solution methods are effective at synthesizing single crystal ultrathin noble metal nanowires, it is very difficult for platinum to grow directly into one-dimensional single crystalline nanowires having high aspect ratios without using templates or substrates. Despite this difficulty, some researchers have been able to show that a facile, highly reproducible and scalable solvothermal technique can synthesize nanowires without stabilizers and templates [65, 66]. This facile surfactant-free method is utilized for the direct growth of Pt nanowire on SG materials. In this way, the combined properties of nanostructured platinum and the support materials effectively fulfill the activity and stability requirements of the catalysts.

(iii) Platinum nanowires supported on S-doped CNT (PtNW/S-CNT)

The superiority of SG as a support for platinum nanoparticles/nanowires has been already discussed in the previous section. The beneficial impact of 1D platinum nanostructures can be further extended using 1D carbon nanotubes (CNTs). CNTs possess attractive mechanical, electrical and thermal properties, which can help to significantly improve the ORR activity and stability. However, the properties of CNTs can also be tuned by doping with sulfur. Therefore, an increase of the number of sulfur sites should introduce more anchoring sites for the platinum nanowires that can provide benefits in terms of the electrochemically active surface area availability and platinum utilization.

Chapter 3 Experimental Methods and Characterization Techniques

The specific methods used to synthesize and characterize the materials throughout the projects are discussed below:

3.1 Fabrication Techniques

3.1.1 Chemical based techniques

Chemical-based synthesis techniques comprise a broad range of procedures used to synthesize various class of materials ranging from nanocarbon materials to ultrathin platinum/ruthenium nanowires [67].

3.1.2 Chemical vapor deposition (CVD)

In general, chemical vapor deposition (CVD) is a process whereby a solid material is deposited from a vapor phase onto the surface of a heated substrate or material of interest. By changing the experimental conditions such as substrate material, temperature, composition of the reaction gas mixture or ratio of precursors, pressure, gas flow rate etc., materials with various properties can be obtained. CVD is an excellent technique that enables the formation at high temperature of a high surface area material such as SG/S-CNT which can serve as a reliable and stable support material for platinum nanostructured catalysts.

3.1.3 Platinum deposition

Platinum nanoparticles deposited onto SG has been synthesized and evaluated in this study. Typically, platinum nanoparticles are deposited using ethylene glycol since this method is very simple, reliable and uses non-toxic materials. Briefly, 80 mg of catalyst support are ultrasonically dispersed in 60 mL of ethylene glycol and mixed with a magnetic stirrer for at least 1h. After that, 4 mL solution of $H_2PtCl_6.6H_2O$ are added into ethylene glycol (5 mg Pt mL^{-1} solution) to achieve 20% Pt in the final crystal material. In order to maintain pH >10, several drops of 2.5 M NaOH are added to the solution and then the contents are heated at 140^{o}C for 4 h under reflux conditions. Finally, a few drops of 2M HCl are added to adjust the pH to 5-6 before filtering the solution and collecting the solids. The final step is to wash and dry the solids in an oven overnight at 70^{o}C for subsequent characterization and evaluation.

3.1.4 Solvothermal synthesis of extended platinum nanostructures

The solvothermal technique involves the synthesis of materials by using an organic solvent for the precursors that are subjected to high pressure and temperature in order to obtain materials with a controlled size and shape distribution and crystallinity. The properties or characteristics of materials can be altered by varying certain experimental parameters such as reaction temperature, reaction time, precursor type, surfactant type and solvent type. In this technique, the precursor solution is loaded into a Teflon-lined sealed autoclave vessel and fastened securely before placing it in an oven at a specified reaction temperature for a given duration. Solvothermal synthesis techniques are capable of producing a wide range of materials such as SG/S-CNT, platinum nanowires and cobalt selenide nanosheets etc.

3.2 Physico-chemical characterizations

3.2.1 Scanning electron microscopy

Scanning electron microscopy (SEM) is a useful technique to investigate the topography and morphology of micro- and nano-structured materials. This instrument uses a powerful beam of electrons (produced by a thermionic or field emission technique) to illuminate the sample and then project images based on the secondary or back-scattered electrons collected by the detector after scanning. The spatial image resolution depends on the spot size of the electron beam and the electron interaction volume and can reach as high as 1 nm. In this project, distinct nanostructures of the synthesized catalyst materials are analyzed using SEM. Sample preparation before SEM imaging involves the spreading of solid catalyst powder onto a conductive carbon tape that is secured to a sample holder. This holder is then placed in the SEM followed by evacuation of the chamber and subsequent imaging.

3.2.2 Transmission electron microscopy

Transmission electron microscopy (TEM) is a powerful imaging tool for producing high resolution images of samples that can approach near-atomic scale. Samples are illuminated by a high energy electron beam (200 to 400 kV) that passes through several condensers and then is transmitted to the sample. Electrons can be scattered elastically or inelastically and then collected. Based on diffraction theory, the signals from the collected electrons are processed to produce images. TEM is a high resolution technique which can effectively determine crystal structure, atomic arrangements, exposed crystal facets and chemical compositions.

3.2.3 Energy dispersive x-ray spectroscopy

Energy dispersive x-ray spectroscopy (EDX) can be carried out simultaneously with a common imaging technique by adding an EDX detector to an SEM and TEM unit. When electrons bombard a material surface of interest, x-rays are also emitted and can be collected by the EDX detector. The energy of the x-rays and their corresponding intensities are related to the appropriate elemental identity and quantity in a specific material. Moreover, elemental mapping can also be done by analyzing the x-rays emitted from localized positions on the sample. Atomic contents depend on the emitted x-ray intensities at various locations and can be used to map the concentration of different elements over the entirety of the sample being investigated.

3.2.4 X-ray diffraction

X-ray diffraction (XRD) is a widespread characterization technique used to determine crystal structures based upon comparison with a diffraction pattern database. Generally, x-ray beams are emitted from a source (Cu, K, Mo, etc.) and directed to the sample of interest. Once these beams interact with the atoms in the materials, a diffraction pattern of a specific crystal structure can be obtained depending on the incident x-ray wavelength and the spacing between the atomic planes in crystalline and polycrystalline materials. XRD is capable of determining the average nanoparticle size and lattice parameter along with the crystal phases. The Scherrer equation can be employed to estimate the average nanoparticle size as follows:

$$d = \frac{k\lambda}{B\cos\theta} \tag{3-1}$$

where d is the average crystal or nanoparticle size, k is the shape factor (0.89), λ is the x-ray wavelength, B (2θ) is the full width at half maximum (FWHM) and cosθ is the maximum angle of the diffraction peak. Furthermore, Vergard's law can be used in order to calculate the lattice parameter a:

$$\mathrm{a} = \frac{\sqrt{2}\lambda k}{\sin\theta} \tag{3-2}$$

3.2.5 X-ray photoelectron spectroscopy

X-ray photoelectron spectroscopy (XPS) involves the use of x-rays to irradiate a sample and cause the emission of electrons from its surface according to the photoelectric effect. The kinetic energies of these emitted electrons are reflective of their specific binding energies which are characteristic of the elements from which they are emitted and their oxidation states. Due to the short mean-free path of electrons, only electrons emitted from the surface of a sample can escape and make it to the detector.

Therefore, surface elemental compositions and oxidation state of the elements can be easily determined by XPS. However, as XPS requires high vacuum ($P \sim 10^{-8}$ millibar), samples to be investigated must be in solid form.

3.2.6 Raman spectroscopy

Raman spectroscopy is a useful technique to obtain the information on rotational and vibrational modes in a system. The Raman effect which is small, but accessible by the use of lasers, involves the interaction of the monochromatic laser light with the molecular vibrations, photons or other excitations in the sample and the resulting shift in the energy of the laser photons. This shift in energy provides information about the vibrational modes in a sample. *In situ* analysis of organic and inorganic compounds can be performed by Raman spectroscopy along with the analysis of gas, aqueous solutions and solid powders. In this study, Raman spectroscopy is used as an important characterization tool for the investigation of defect sites in graphene or CNT.

3.3 Electrochemical and Performance Characterization

3.3.1 Cyclic voltammetry

Cyclic voltammetry (CV) is a potentiostatic electrochemical technique used to examine the electrochemical properties of electrodes. In a cyclic voltammetry test, the potential of the working electrode is varied linearly between two potential limits with respect to time and the corresponding current is measured. A typical CV of Pt/C collected at a sweep rate of 50 mV s^{-1} in N_2-saturated 0.1 M $HClO_4$ shows the current response of the working electrode when the potential is swept and cycled between 0.05 to 1.3 V vs. RHE (**Figure 3-1**). Positive current corresponds to anodic current and negative current represents the cathodic current. The CV can be divided into three regions: (i) H underpotential deposition region (~0.05 to 0.4 V vs. RHE), (ii) double layer region (~0.4 to 0.7 V vs. RHE) and (iii) Pt oxide formation region (above 0.7 V vs. RHE). As the potential increases from ~0.05 to 0.4 V vs. RHE during the forward scan, the pre-adsorbed H atoms on Pt surface are oxidized to form H^+ which desorbs from the Pt surface and then diffuses into the electrolyte. When the potential increases (in a potential window above 0.7 V vs. RHE), Pt is oxidized to form Pt hydroxide or oxide, i.e. PtOH or Pt oxides by the adsorption and dissociation of H_2O molecules. When the potential is decreased to ~ 0.7 V vs. RHE during the backward scan, the reduction of Pt-OH or Pt oxide occurs. With a further decrease of the potential to 0.4 V vs. RHE, the protons in the electrolyte adsorb on the Pt surface and are reduced via H underpotential deposition. The Pt surface is free of H

or OH/H in the potential window of ~ 0.4 to 0.7 V vs. RHE known as the double layer region. The current measured in this region is not associated with a faradaic process and instead is associated with capacitive effects due to the contribution from the large surface area carbon support and anionic adsorption of the electrolyte. This capacitive current must be subtracted from faradaic currents before estimating the electrochemically active surface area (ECSA) of platinum from such a CV. The charge associated with H adsorption or desorption is integrated to determine the number of hydrogen atoms adsorbed in a monolayer of coverage of the electrode surface. From knowledge of the electric charge density C for each cm^2 covered by H atoms (0.21 mC m^{-2} Pt), the specific ECSA of Pt (m^2 gm^{-1} Pt) can be determined as follows:

$$ECSA = \frac{Q}{mC} \tag{3-3}$$

where Q is the total integrated charge for H adsorption/desorption (mC cm^{-2} electrode) obtained from the CV and m is the mass loading of platinum (mg cm^{-2} electrode) .

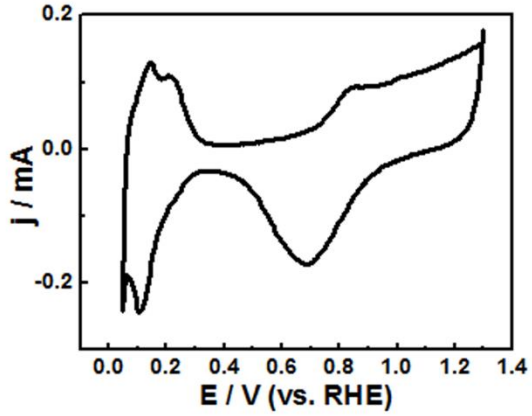

Figure 3-1 Typical CV of the commercial Pt/C catalyst.

3.3.2 Half-cell rotating disc electrode testing

The use of a half-cell rotating disc electrode (RDE) is a simple and effective approach for screening of electrochemical reactions in electrodes. The electrocatalytic evaluation of catalyst materials is cumbersome and time-consuming when it is done on the basis of full cell experiments in an operating fuel cell. A typical three-electrode cell used in a RDE technique is shown below in **Figure 3-2**.

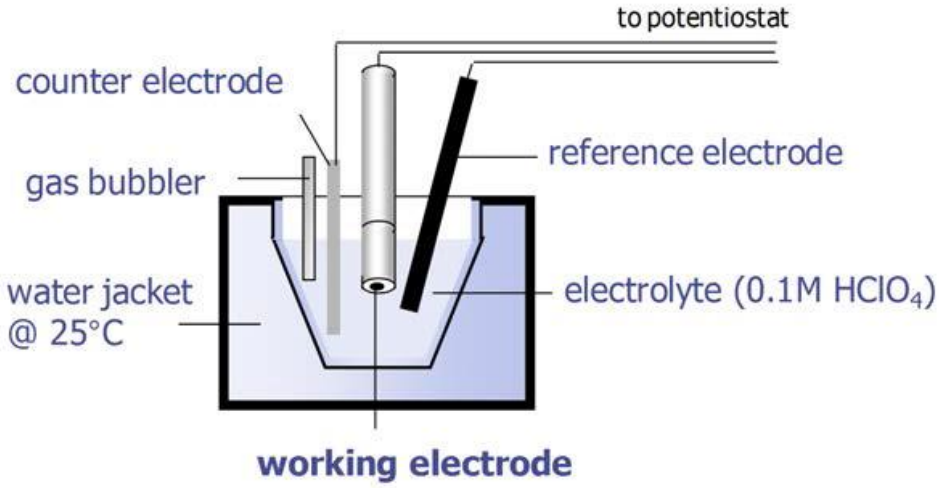

Figure 3-2 Three electrode half-cell system.

In fact, the RDE technique allows the precise control of electrocatalytic activity measurements by differentiating between effects due to the limited activity of the catalyst and poor mass transport of reactant gas. The rotation of the working electrode induces convective mass transport to bring the reactant to the surface of the electrode in a controlled fashion. The intrinsic properties of the electrolyte and the rotation speed determine the flux of the reacting gas to the electrode surface. The overall measured current i is related to the component i_k associated with kinetic limitations and the mass transport limiting current i_d which in turn can be described using the Levich equation to yield:

$$\frac{1}{i} = \frac{1}{i_K} + \left(\frac{1}{0.620\, n\, F\, A\, D^{2/3}\, \nu^{-1/6}\, C} \right) \omega^{-1/2} \qquad (3\text{-}4)$$

where n is the number of transferred electrons, F is the Faraday constant, A is the electrode area, C is the concentration of the dissolved electroactive species O_2, D is the diffusivity of the electroactive species , ν is the kinetic viscosity of electrolyte and ω is the rotational speed. A plot of $\frac{1}{i}$ vs. $\omega^{-1/2}$, known as the Koutecky-Levich (K-L) plot should give a straight line with a y-axis intersect equal to $\frac{1}{i_k}$. From the measured slope, the number of electrons transferred due to the electrode reaction can be determined. The obtained kinetic current (typically obtained at 0.9 V) is significant in terms of the specific and mass activities of the platinum catalyst. The former (mA m^{-2} Pt) measures the intrinsic catalytic value of platinum, while the latter provides the activity normalized to the cost of platinum.

In a half-cell RDE test, the three electrodes are known as the working, counter and reference electrodes. In order to evaluate the ORR, the working electrode is normally coated uniformly with the catalyst material. To prepare the working electrode, the catalyst particles are first dispersed in 2 mL ethanol containing 5μL (15 wt.%) Nafion solution for at least 30 minutes and then loaded onto the glassy carbon (GC) electrode with a diameter of 5 mm. In order to compare the results obtained from different experiments, the loading of catalyst in each case is controlled to be 20 $\mu g_{Pt} cm^{-2}$. During the coating of materials onto the GC electrode, efforts are made to ensure that the electrode thickness is uniform to minimize any possible mass transfer limitations of the reactants. Also, each material is tested at least three times to confirm the reproducibility of the results. The counter electrode is a platinum-based electrode, while several possible reference electrodes (e.g., Ag/AgCl, standard calomel electrode, reversible hydrogen electrode-RHE) can be used. The three electrodes are immersed into an electrolyte, i.e. 0.1 M $HClO_4$ or 0.5 M H_2SO_4, to obtain a polarization curve for ORR at a certain rotation speed. **Figure 3-3** shows a typical polarization curve of the ORR on carbon-supported Pt nanoparticles in 0.1 M $HClO_4$ at a scan rate of 50 mV s^{-1} and various rotational speeds. The K-L plot is also obtained to calculate the number of electrons transferred by the ORR reaction. Three regions are evident from the ORR polarization curve: (i) minimal current flows at potentials more positive than 0.9 V due to the insufficient overpotential to drive the ORR forward, (ii) mixed-controlled region where both ORR kinetics and O_2 mass transport affect the overall rate at potentials from~0.7 to 0.9 V and (iii) diffusion-controlled region at potentials below 0.7 V when transport of O_2 to the catalyst surface becomes rate-limiting.

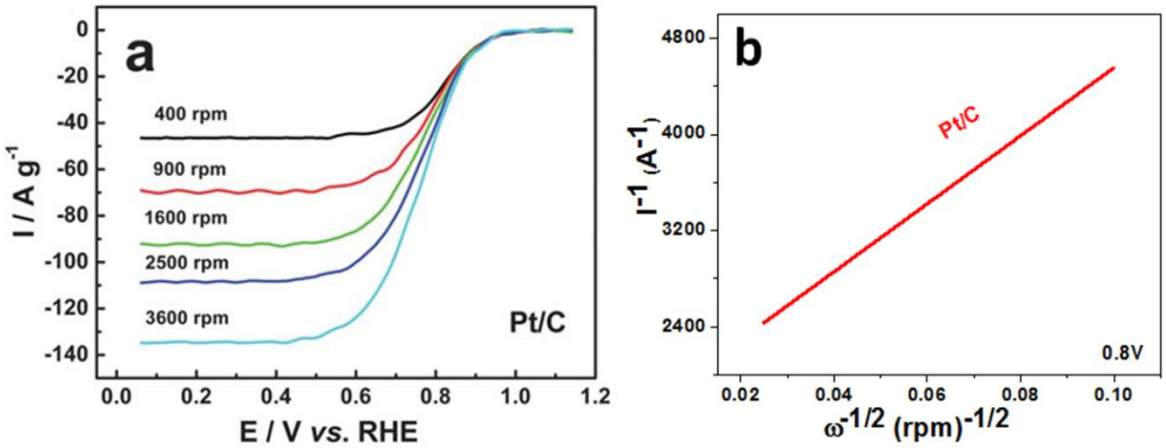

Figure 3-3 (a) ORR polarization curve of commercial Pt/C and (b) Corresponding K-L plot.

3.3.3 Half-cell accelerated degradation testing

The RDE set-up can be used to conduct accelerated degradation testing (ADT) to investigate the durability of the catalyst materials. In these tests, catalyst materials are normally subjected to repeated potential cycles (normally several thousand at least) in a range between 0.05 and 1.5 V vs RHE. These transient conditions are very harsh and will induce catalyst deactivation faster than what might be encountered under normal operative conditions. In this way, it is possible to compare the ORR activity, ECSA and electrochemical signature of the materials before and after ADT. This will enable the electrochemical stability and the effects of any physical changes that may occur due to the extended potential cycling to be assessed. Typical guidelines regarding experimental conditions that can used for ADT testing have already been published (US Department of Energy-Fuel Cell Technologies Office Webinar). Parameters can be modified during testing to induce different catalytic degradation mechanisms. For example, a potential range that spans the oxidation/reduction of Pt surface sites will accelerate Pt particle/nanowire degradation, while higher electrode potentials will cause more rapid corrosion of the carbon support materials. Many different ADT conditions are described in the literature and chosen according to the objectives of each particular study.

Chapter 4 Platinum Nanoparticles on Sulfur-Doped Graphene

The following section is based on previously published work by Higgins, D. C.[†], **Hoque, M. A.[†],** ([†]equal contribution) Seo, M. H., Wang, R., Hassan, F., Choi, J-. Y., Pritzker M., Yu, A., Zhang, J., Chen, Z.

Advanced Functional Materials 2014, 24(24): 4325-4336

"Development and simulation of sulfur-doped graphene supported platinum with exemplary stability and activity towards oxygen reduction"

Author contributions: H.M.A conducted the material preparations, characterizations and electrochemical tests. H.M.A and H.D.C co-wrote the manuscript. S.M.H performed the DFT analysis. C.Z. and P.M co-supervised the project. All authors reviewed the manuscript.

4.1 Introduction

Polymer electrolyte membrane fuel cells (PEMFCs) offer the great appeal of high energy conversion efficiency, excellent energy density and environmentally benign operation; however, they require highly active and operationally stable catalysts to facilitate the inherently sluggish oxygen reduction reaction (ORR) occurring at the cathode. Conventional PEMFC systems employ platinum (Pt)-based catalysts, which to date have been the only materials capable of catalyzing the ORR to practical rates, although still insufficient for PEMFC operation. The widespread commercialization and deployment of PEMFCs into advanced sustainable energy infrastructures including the automotive sector is still limited by three primary factors: (i) high cost, (ii) insufficient performance and (iii) low durability.[68, 69] At the root of these limitations lies the aforementioned expensive Pt catalyst materials employed; generally consisting of Pt nanoparticles (ca. 2-3 nm) uniformly distributed on high surface area carbon black supports (Pt/C).

Although significant improvements to state-of-the-art Pt/C catalysts and electrode designs for automobile PEMFCs has been realized in recent years, an immense challenge in achieving the 2017 technical targets set by the United States Department of Energy still remains for the current state-of-the-art catalyst technology. According to these targets, the total Pt loading (anode and cathode) must be reduced to below 0.125 mg cm^{-2} coupled with 5,000 hours of operational stability under simulated drive cycleS by 2017.[70] Specifically, Pt/C is known to degrade under the harsh oxidizing conditions

encountered at the PEMFC cathode due to corrosion of the carbon support materials or by agglomeration and/or dissolution of the platinum nanoparticles resulting from weak interactions with the catalyst supports.[71] This in turn leads to a sharp loss in available electrochemically active surface areas (ECSA) and by extension fuel cell performance.

A common approach to improve catalyst stability and activity has involved the design of non-conventional catalyst supports, including transition metal oxides and nitrides;[72-75] or alternative carbon supports doped with heteroatoms such as nitrogen to enhance the interaction and synergy between the catalyst particle and its support.[54, 76] It is well understood that the structure and properties of the support materials will directly govern the performance and stability of the catalyst materials. There still however remains a lack of fundamental understanding regarding the exact nature of these particular catalyst-support interactions [77], a phenomena that has widespread implications in many fields of heterogeneous catalysis.[78] Recent advances in density functional theory and computational chemistry now provide the tools to adequately model catalyst behavior and enable a more advanced understanding of electro-catalysis; including the specific catalyst-support interactions occurring at the cathode of fuel cells. It is thereby a worthwhile approach to couple fundamental computational simulations with experimental investigations of novel nanostructured support materials. This will allow scientists to predict, understand and explain improvements in catalytic activity and durability that are influenced by supports, thereby providing valuable guidance for future catalyst design endeavors.

Graphene has recently emerged as a highly promising catalyst support material for PEMFC applications due to its immense surface area, excellent conductivity and electron transfer capabilities that are important properties for electro-catalysis.[34, 35, 79] Graphene is theoretically composed of only graphitic carbon atoms which can provide added resistance against corrosion during PEMFC operation,[36] although the relatively inert and hydrophobic nature of its surface does not culminate in facile Pt deposition. This requires functionalization procedures to obtain well-dispersed nanoparticles and overcome stability limitations.[37] To this end, nitrogen-doped graphene and other graphitic carbons have been extensively developed and investigated for fuel cell catalyst applications, either as stand-alone ORR electrocatalysts in alkaline media[38-46] or as Pt nanoparticle supports under acidic (i.e. PEMFC) conditions.[47-53] The presence of nitrogen dopants has been reported to exert a "tethering" effect on Pt nanoparticles,[53, 54] providing both beneficial catalytic activity and stability enhancements. While density functional theory simulations of the adsorption and binding interactions

between Pt and either nitrogen- or boron-doped graphene or CNTs,[55-58] a fundamental understanding of the Pt-heteroatom doped graphene catalyst-support interactions and their associated impact on ORR performance and operational stability is still lacking. Furthermore, the impact of graphene doped with various other heteroatoms (i.e. sulfur) remains largely unexplored despite their high potential for applications as ORR catalysts[19, 59, 60] or catalyst support materials.[61] Elucidation of these important considerations can be provided by effectively linking fundamental computational simulations with detailed experimental investigations.

In the present work, we report the development of sulfur-doped graphene (SG) as Pt nanoparticle support materials by thermal shock/quench annealing a mixture of graphene oxide (GO) and phenyl disulfide (PDS). After Pt deposition onto SG (Pt/SG) by a modified ethylene glycol (EG) method, uniformly sized nanoparticles well dispersed across the entirety of the SG surface have been successfully obtained. Improved ORR activity has been found for Pt/SG in comparison to Pt supported on undoped graphene (Pt/G) and to commercial state-of-the-art Pt/C. Furthermore and most notably, we also observed significantly enhanced stability of Pt/SG; including excellent ORR activity and ECSA retention after exposing the catalysts to repetitive potential cycles in a 0.1 M $HClO_4$ electrolyte.

On the basis of these observations, we performed *ab initio* density functional theory calculations to investigate the interactions occurring between SG and Pt and elucidate the root causes of the ORR performance and stability enhancements. Based on comparative simulations on both doped and undoped G, we found that the strengthened interaction and binding energies between Pt and SG occur exclusively due to sulfur incorporation. Specifically, sulfur doping leads to stronger adsorptive and cohesive binding energies with Pt, leading to the aforementioned catalyst-support tethering effect, along with a negative shift of the d-band center of the Pt atoms. These findings are used to explain the dramatically enhanced stability and improved activity of Pt/SG, respectively, in comparison to both Pt/G and Pt/C. This work represents the first comprehensive report of fundamental *ab initio* simulations linked to rigorous experimental investigations for sulfur-doped graphene. Furthermore, Pt/SG is presented for the first time as a highly active ORR catalyst material with exemplary stability capabilities for PEMFC applications.

4.2 Experimental Section

4.2.1 Graphene oxide (GO) synthesis

Graphene oxide was prepared from graphite powder (Alfa Aesar, natural, microcrystal grade, APS 2-15 micron, 99.9995%) using an improved method reported previously by Marcano *et al*.[80] Briefly, 2.2 g of graphite powder were added to 400 mL of a 9:1 volumetric mixture of concentrated H_2SO_4/H_3PO_4. 18 g of $KMnO_4$ was then added slowly and the reaction was heated to 50^oC and held for 16 hours. After completion, the reaction mixture was cooled down to ca. 10^oC in an ice container and 400 mL DDI water was added in a dropwise fashion. Finally 15 mL of H_2O_2 (30%) was added in order to complete the oxidation reaction. The final mixture was centrifuged to separate out the solids which were washed thoroughly with water, ethanol and HCl (30 %) before undergoing lyophilization.

4.2.2 Sulfur doping of graphene synthesis

A thermal shock/quench annealing process was utilized to prepare SG materials using a tube furnace operating under the protection of argon (100 sccm). Specifically, 200 mg of GO and 100 mg of phenyl disulfide (PDS, Sigma Aldrich) were ultrasonically dispersed in 4 mL of ethanol for 20 minutes. The residual solvent was then evaporated to obtain a uniform solid mixture by holding the temperature at 70^oC on a hot plate. The solid mixture was then transferred to a quartz boat, which was placed in the large tube furnace for annealing. The sample was kept outside of the heating zone while the temperature of the furnace was raised to 1000^oC, after which the sample was slid inside the tube furnace and left for 30 minutes before removal and cooling. The SG was washed with acetone, DDI and ethanol thoroughly to remove any residual organic impurities, and then dried for further processing. Pure graphene (G) was synthesized for comparative purposes by a similar procedure, albeit in the absence of PDS.

4.2.3 Platinum nanoparticle deposition

Pt was deposited onto SG (Pt/SG) and G (Pt/G) using the modified ethylene glycol (EG) technique.[81] Briefly, 80 mg of SG was ultrasonically dispersed in 50 mL EG for 1 hour, after which the pH was adjusted above 10 by adding a 2.5 M NaOH in EG solution and the mixture stirred for 12 hours. 4 mL of hexachloroplatinic acid dissolved in EG (5 mL Pt per mL EG) was then added dropwise corresponding to a Pt catalyst loading of 20 wt%. The temperature was then raised to 130^oC to initiate Pt reduction that was allowed to proceed for 7 hours under reflux conditions in order to ensure the reaction went to completion. After cooling the mixture, several drops of 2M HCl were added to adjust

the pH in the range of 6 to 7. Finally, the resulting mixture was filtered and washed thoroughly with DDI water and then dried.

4.2.4 Physico-chemical characterization

The samples were characterized by transmission electron microscopy (TEM, JEOL 2010F) equipped with energy dispersive x-ray spectroscopy (EDX) for elemental quantification and mapping. Further physical and spectroscopic characterizations included Raman spectroscopy (Bruker -Senterra 314), X-ray diffraction (XRD, Inel XRG 3000 diffractometer), x-ray photoelectron spectroscopy (XPS, PHI Quantera) and scanning electron microscopy (SEM, LEO FESEM 1530).

4.2.5 Electrochemical activity and durability measurements

A conventional three-compartment electrochemical cell employing a Pt wire counter electrode and reversible hydrogen reference electrode (RHE) was used for all electrochemical tests. A glassy carbon working electrode was prepared by cleaning and polishing it thoroughly, followed by pipetting 10 uL of catalyst ink (2 mg catalyst dispersed in 950 µL ethanol and 50 µL of 5 wt.% Nafion® solution). All electrodes were prepared with a Pt loading of 20 $\mu g_{Pt} cm^{-2}$, while the ink concentration of commercial state of the art Pt/C (TKK, 28.2 wt. % Pt) tested for comparison was modified accordingly. Experiments were carried out in 0.1 M $HClO_4$ electrolyte at 30^{o}C, either saturated with O_2 for ORR measurements or N_2 for background current collection and ECSA measurements. The ORR activity was measured at a potential scan rate of 10 mVs^{-1} and CV curves were obtained for ECSA measurements at 50 mVs^{-1}. Accelerated degradation testing (ADT) was carried out by cycling the electrode potential 1,500 times under N_2 saturation between 0.05 and 1.3 V vs RHE at a scan rate of 50 mVs^{-1}.

4.2.6 Computational details

Density functional theory (DFT)[82, 83] calculations were carried out using the Vienna *ab initio* simulation package (VASP).[84] The exchange-correlation energies of electrons are described by the Perdew, Burke and Ernzerhof (PBE) functional[85] for generalized gradient approximation (GGA).[86] Core electrons were replaced by the projector augmented wave (PAW) pseudo-potentials,[87, 88] while Kohn-Sham wave functions for the valence electrons were expanded using a plane-wave basis set with a cutoff energy of 520 eV. A periodic boundary condition was imposed on the doped graphene unit cell with a vacuum space of 20 Å for the graphene sheets to avoid interplanar interactions. To sample the Brillouin zone, a Gamma point mesh of 36 × 36 × 1 was used in relation to the size of the

graphene (1 × 1) unit cells with a smearing of the Methfessel-Paxton method[89] to find the thermodynamically stable S-doped graphene structures. For larger supercells, smaller mesh sizes were used. The graphene, graphitic and thiophene-like S-doped graphene sheets having (4 × 4) supercells were fully relaxed to optimize the structures with Pt atom deposited on the surfaces. Furthermore, the Pt nanoparticles deposited on (8 × 8) supercells of pristine graphene, graphitic and thiophene like S-doped graphene were also calculated with a Gamma point mesh of (4 × 4 × 1). Spin polarized calculations were performed and the tetrahedron method with Blöchl corrections was used to calculate the density of states (DOS).[90]

Equation (4-1) was used to calculate the formation energy (EF) of the SG structures investigated.

$$E_F = E(C_{m-n}S_n) - (m-n)\mu_{C,graphene} - \frac{1}{6}n\mu_{S_6} \quad (4\text{-}1)$$

Here, *n* is the concentration of sulfur in the graphene framework and $E(C_{m-n}S_n)$ is the corresponding energies obtained from the VASP program. $\mu_{C,graphene}$ and μ_{S_6} are the chemical potentials of carbon and sulfur taken to be the total energy of a graphene sheet per atom and cyclo-hexasulfur, respectively.[91]

The adsorption energy between Pt and the various carbon supports (E_{ads}) was calculated by Equation (4-2):

$$E_{ads} = E_{Pt/support} - E_{Pt} - E_{support} \quad (4\text{-}2)$$

Here, $E_{Pt/support}$ is the total energy of the support material with a single Pt atom on it, E_{Pt} is the total energy of the Pt atom and $E_{support}$ is the total energy of the support.

4.3 Results and discussion

4.3.1 Physicochemical characterization

After preparation, both SG and G demonstrated a wrinkled voile-like structure consisting of thin single or multi-layer graphene sheets **(shown in Figure A-1 in the Appendix)** and indicative that the presence of PDS during high temperature thermal annealing had negligible impact on the resultant physical structures. With the whole preparation processes schematically depicted in **Figure A-2 (Appendix)**, Pt nanoparticle deposition by the well-established ethylene glycol technique[49, 81, 92] was capable of achieving excellent nanoparticle dispersion and a narrow size distribution for both Pt/SG **(Figures 4-1a, b)** and Pt/G **(Figures 4-1c, d)**. The x-ray diffraction (XRD) profile displayed typical

Pt fcc peaks with the diffraction pattern of the commercial state of the art Pt/C (TKK) used throughout the present investigation included for comparison **(Figure 4-1e)**. By applying the Scherrer equation to the Pt(220) peak, average Pt nanoparticle sizes were calculated to be 2.16, 2.42, 2.25 for Pt/SG, Pt/G and Pt/C, respectively. These values are in close agreement, albeit slightly larger than the calculated average nanoparticle sizes of 2.10, 2.25 and 2.15 nm, respectively, obtained directly from analysis of transmission electron microscopy (TEM) images.

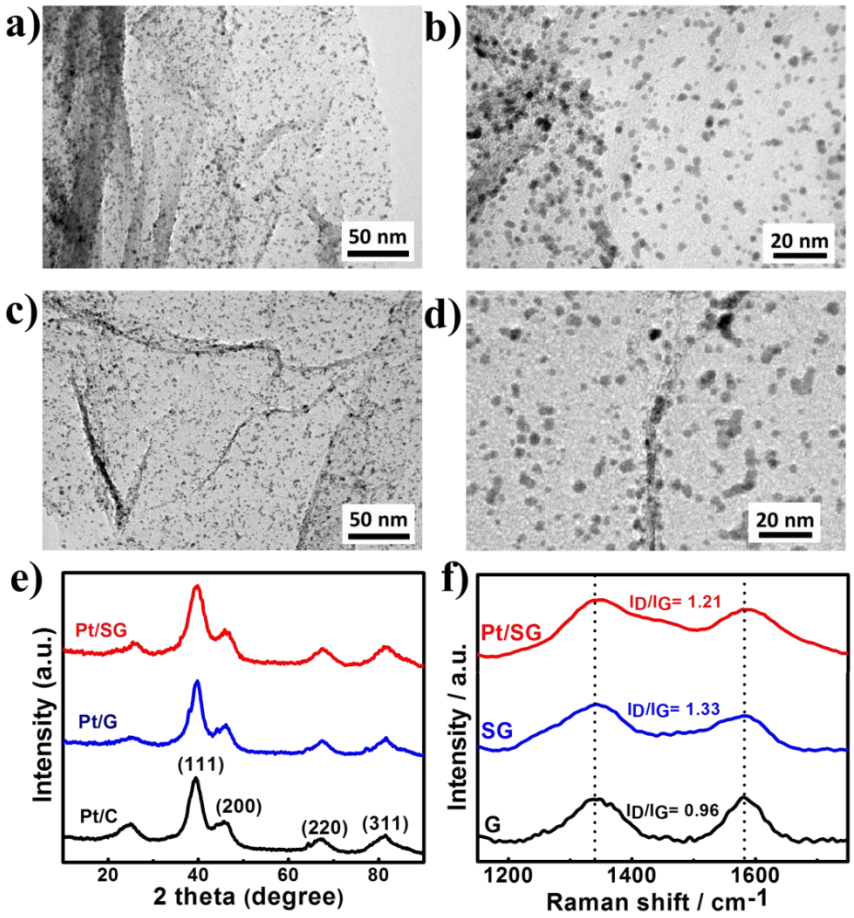

Figure 4-1 TEM images of (a,b) Pt/SG and (c,d) Pt/G, (e) XRD pattern and (f) Raman spectra.

The Raman spectra for SG and G **(Figure 4-1f)** display a strong D-band peak, typically attributed to disorder or defects in the crystalline graphitic structure of carbon-based materials. These were analyzed to obtain the ratio of the intensities of the D-band to G-band (I_D:I_G). I_G attributed to the E_{2g} vibrations from sp^2 bonded carbon is commonly used as a gauge for structural disorder in graphitic

materials. I_D:I_G values for SG and G were calculated to be 1.33 and 0.96, respectively. Both materials exhibited higher I_D:I_G ratios than that of pristine graphene in which the D-band is theoretically non-existent.[93] Typically, good Pt nanoparticle distribution and uniform sizing are difficult to achieve on relatively inert graphitic surfaces such as CNTs or graphene[37] and requires the use of specific pre-treatment or functionalization procedures.[94-96] Clearly the high temperature shock anneal/quench of GO and PDS in the present study is capable of producing graphene-based materials with interruptions in the planar crystal lattice as highlighted by Raman spectroscopy; and furthermore offers reasonable explanation for the facile deposition of well-dispersed Pt nanoparticles. This notion is supported by the reduced I_D:I_G ratio of 1.21 for Pt/SG **(Figure 4-1f)**, suggesting that the Pt nanoparticles deposit favourably on the defect sites of SG and thereby suppress the vibrations from the underlying functionalities.

To gain understanding of the identity and concentrations of the surface species most likely responsible for the anchorage of Pt catalyst nanoparticles, x-ray photoelectron spectroscopy (XPS) was conducted to yield the full range spectra displayed in **Figure 4-2a.** The surface atomic concentrations for SG and G listed in **Table A-1 (Appendix)** have been obtained from the narrow C1s scan spectra (**Figure A-3 in Appendix)**. Of particular interest is the appearance of an S2p sulfur signal centered at 161.1 eV for SG, representing a surface concentration of 2.32 at. %, a value consistent with results from energy dispersive x-ray (EDX) analysis (2.41 at. %) that also indicated the sulfur atoms are well distributed over the entirety of the materials **(Figure A-4 in the Appendix)**. Interestingly, this sulfur content is larger than that in SG materials reported previously[19, 59, 60] and approaching that of a sulfur-doped microporous carbon obtained by heat treating sulfur-rich thienyl-based polymers at the same temperature.[30] This indicates the effectiveness of applying the thermal shock/quench technique on a mixture of GO and DPS to incorporate sulfur dopants into the final graphene structure.

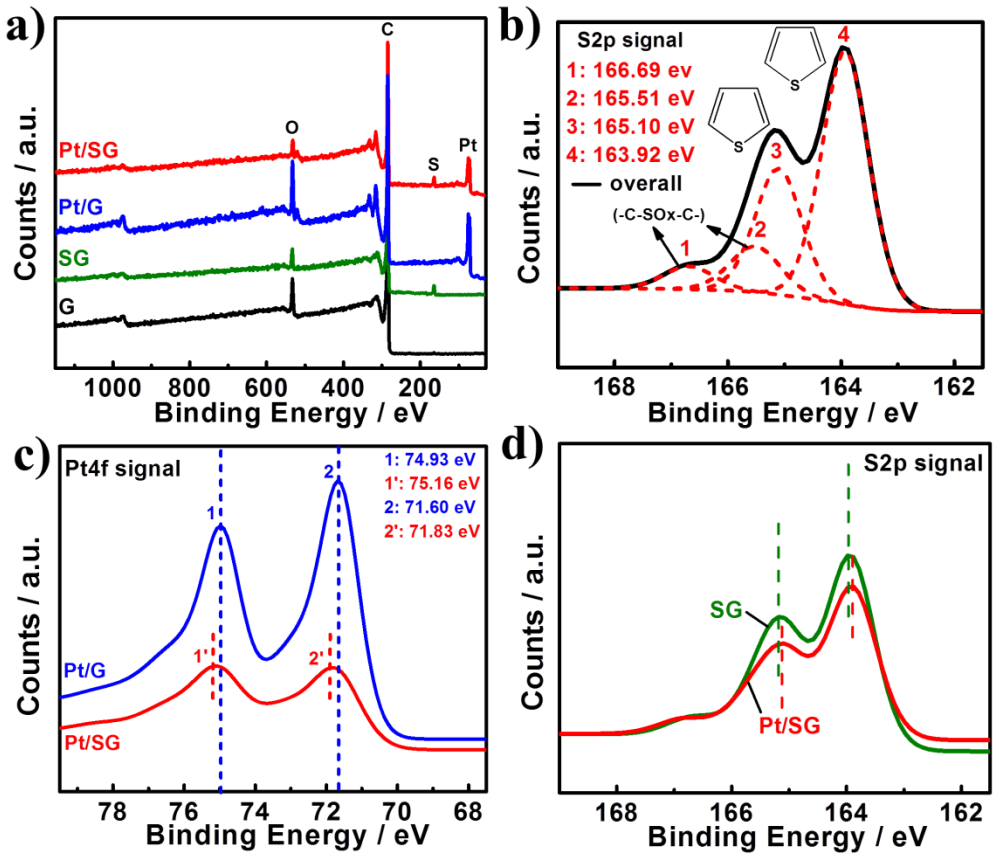

Figure 4-2 XPS spectra: (a) full range, (b) S2p, (c) Pt4f and (d) S2p.

Figure 4-2b provides a high resolution XPS scan of the S2p signal deconvoluted into two minor peaks located at 166.69 (peak 1) and 165.51 (peak 2) and two major peaks located at 165.10 (peak 3) and 163.92 eV (peak 4). While the minor peaks can be attributed to carbon bonded SO_x species,[19, 97] the two major peaks appear to result from the S2p spin-orbit doublet ($S2p_{1/2}$ and $S2p_{3/2}$, respectively) with a separation of 1.18 eV, which is in close agreement with the theoretical spin doublet separation of 1.13 eV.[98] These peaks can be attributed to sulfur bonded directly to the carbon atoms in a heterocyclic configuration[99, 100] since no elemental sulfur was observed by XRD or TEM and, if present, would have been removed by the rigorous washing procedure employed after SG synthesis. We also speculate that these C-S-C species exist in the thiophene form, a notion consistent with previously reported investigations[59, 60, 101] and supported by our formation energy calculations discussed later. Furthermore, thiophene species exist in a pentagonal arrangement, thereby residing on the edge plane and defect sites of SG and most likely giving rise to the strong emergence of the D-

band observed through Raman spectroscopy. It is expected that these sulfur-based species could serve as anchoring sites for Pt-ion nucleation and subsequent nanoparticle growth.[61] In terms of Pt deposition on G, well distributed nanoparticles are also most likely anchored on the edge plane or defect sites.[102] The presence of these moieties in G is indicated by XPS that also indicate a surface oxygen concentration of 7.49 at. %, which is supported by the collected Raman spectra.

XPS also serves as an important tool for probing the electronic states of catalyst materials, which in the case of Pt plays a governing role in terms of catalyst activity and stability.[34] Detailed Pt4f spectra are provided in **Figure 4-2c** for Pt/G and Pt/SG. Both materials display the characteristic doublet of zero-valence Pt[103] with the $Pt4f_{7/2}$ and $Pt4f_{5/2}$ peaks located at 71.60 and 74.93 eV for Pt/G, and 71.83 and 75.16 eV for Pt/SG, respectively. Small doublet contributions are observed for Pt(II) species at higher binding energies, although the differences between the two samples and contributions to the overall spectra are difficult to resolve. It is important to notice the positive peak shifts of 0.23 eV for Pt/SG in comparison to Pt/G. This provides indication of an enhanced interaction between the Pt and the support materials. Furthermore, the increase in electron binding energy for Pt/S indicates a transfer of electrons from Pt to the SG supports. This notion is further supported by a ca. 0.11 eV negative shift in the S2p doublet peak positions for Pt/SG in comparison to SG, indicating that the sulfur atoms in SG and Pt might exist in a $Pt^{\delta+}$-$SG^{\delta-}$ arrangement.[104]

4.3.2 Electrochemical activity and stability

To investigate catalyst stability, accelerated durability testing (ADT) protocols are commonly employed to simulate the harsh, potentiodynamic and corrosive conditions encountered at the cathode of PEMFCs during operation. Pt/SG, Pt/G and Pt/C catalysts were subjected to 1,500 cycles under nitrogen-saturated electrolyte with cyclic voltammograms (CVs) collected before and after ADT, as shown in **Figures 4-3a, b and c,** respectively. Pt/SG and Pt/G clearly provide higher double layer current densities, attributed to the high surface areas and capacitance capabilities of graphene materials. ECSA values were determined based on the calculated charge for hydrogen adsorption/desorption initially and after each 500 subsequent cycles. It can be seen that the ECSA retention of Pt/SG is clearly superior to that of the other two catalysts, retaining 87 % of its initial surface area after 1,500 cycles compared to 54 and 48 % for Pt/G and commercial Pt/C, respectively. The improved stability of Pt/G in comparison to Pt/C is an observation consistent with previous investigations[8, 105, 106] and primarily attributed to the higher graphitic content of graphene-based supports, enhanced Pt-π orbital bonding strength and the presence of functional anchoring groups.

However, the dramatically enhanced stability of Pt/SG in comparison to Pt/C, and more importantly in comparison to Pt/G can be exclusively linked to sulfur incorporation into the graphene structure of the support materials. This strongly suggests that improved catalyst-support interactions between SG and Pt comprise the root cause of these stability enhancements. Interestingly the emergence of quinone/hydroquinone redox peaks (around ca.0.6 V vs RHE) were observed after ADT especially in the case of Pt/G (**Figure 4-3b**). This could be due to the formation of these species, most likely on the planar edges of graphene induced by the high potentials encountered during ADT. In the case of Pt/SG, suppression of the hydrogen adsorption/desorption peaks and large oxidative currents at potentials above ca. 1.0 V vs RHE are not observed after ADT, indicating that no significant emission of sulfur-oxide species from SG due to degradation occurs in these developed materials.[107]

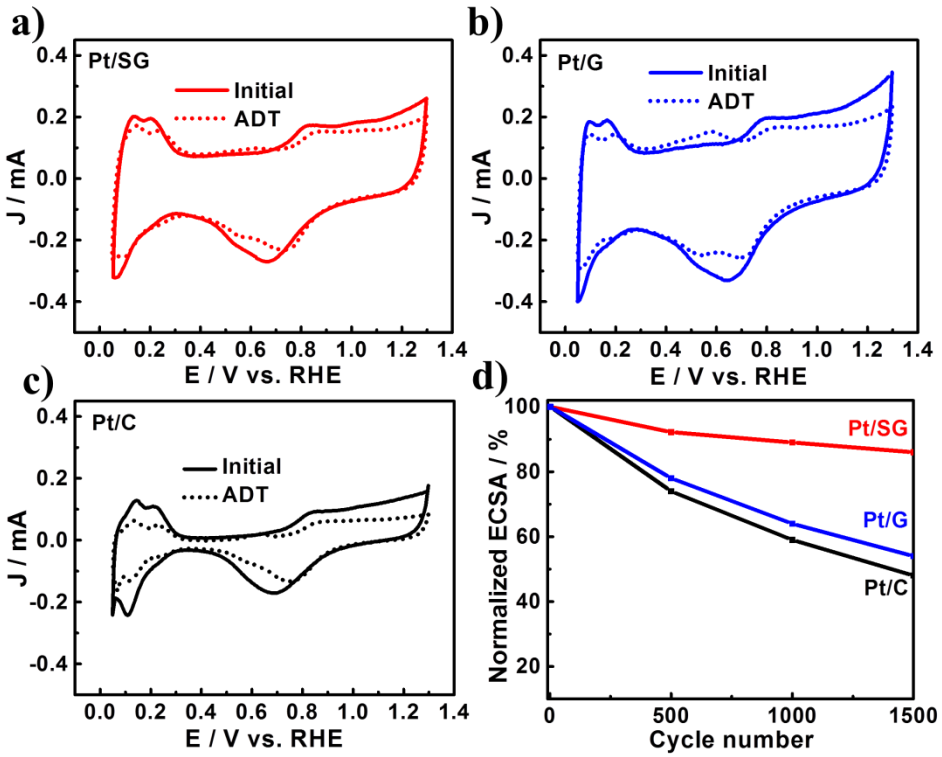

Figure 4-3 CV curves for (a) Pt/SG, (b) Pt/G, (c) Pt/C and (d) normalized ECSA.

ORR activity polarization curves for Pt/SG, Pt/G and Pt/C obtained both before and after ADT are presented in **Figures 4-4a, b and c,** respectively. All three materials demonstrate typical ORR polarization curves after correction for electrolyte resistance, with well-defined diffusion limited currents below ca. 0.7 V vs RHE. Polarization curves at various rotation rates and the corresponding

Koutecky-Levich plots for Pt/SG are shown in **Figure A-5 in the Appendix**. It can specifically be seen that Pt/SG initially demonstrates excellent ORR activity, with a kinetically corrected Pt mass-based activity of 139 mA mg_{Pt}^{-1} at an electrode potential of 0.9 V vs RHE **(Figures 4-4d and f)** and rotation speed of 1600 rpm. This is superior to that of Pt/G (101 mA mg_{Pt}^{-1}) and commercial Pt/C (121 mA mg_{Pt}^{-1}) measured under the same conditions at identical Pt electrode loadings. The order of the mass-based activities (Pt/SG > Pt/C > Pt/G) is commensurate with the differences in average Pt nanoparticle size. However, since the specific activity of Pt/SG (279 µA cm^{-2}_{Pt}) is superior to that of Pt/G (235 µA cm^{-2}_{Pt}) and Pt/C (230 µA cm^{-2}_{Pt}) despite smaller average nanoparticle sizes, it appears that particular catalyst-support interaction effects also play a role in the enhanced activity of Pt/SG, but to an unknown extent.

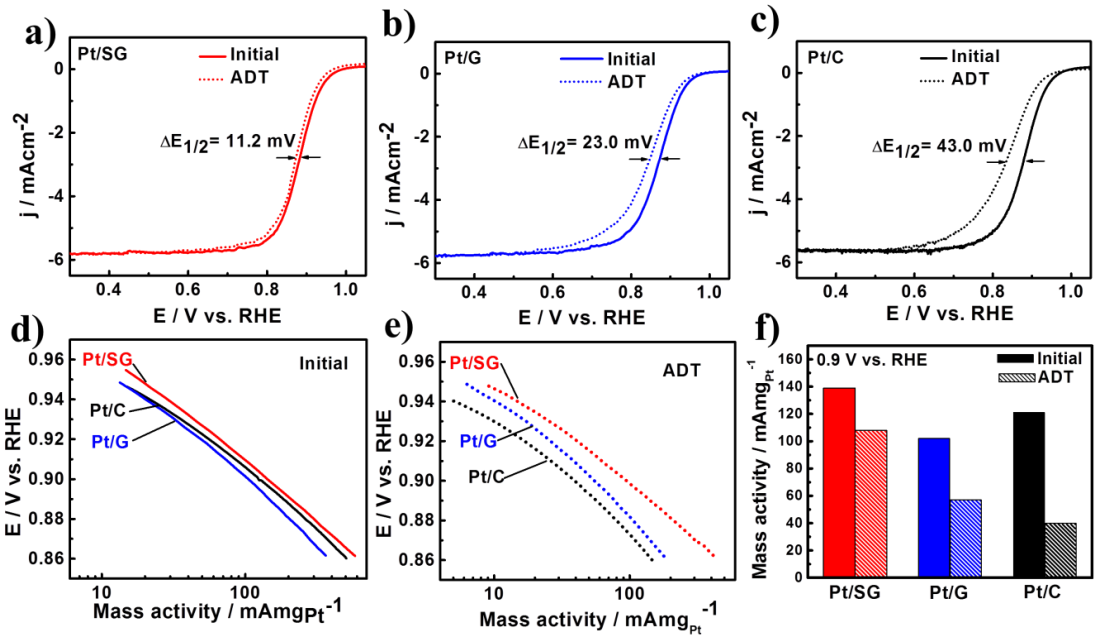

Figure 4-4 ORR for (a) Pt/SG, (b) Pt/G and (c) Pt/C. (d-f) Pt mass based activities of each catalyst.

Pt/SG furthermore possesses excellent ORR activity retention after the ADT. After 1,500 potential cycles, Pt/SG demonstrates only an 11.2 mV loss in its half-wave potential ($E_{1/2}$) and retains almost 78% of the Pt-mass based activity at 0.9 V vs RHE **(Figures 4-4 e and f)**. Meanwhile, Pt/G exhibits a 23.0 mV loss in $E_{1/2}$ and retains 56% of its Pt mass-based activity at 0.9 V vs RHE, whereas Pt/C demonstrates a significant $E_{1/2}$ loss of 43.0 mV and retains only 33% of the initial Pt mass-based activity. This culminates in Pt/SG boasting a 171% higher Pt mass-based activity after the ADT in

comparison to that of the commercial Pt/C catalyst (i.e., 108.0 versus 39.8 mA mg_{Pt}^{-1} at 0.9 V vs RHE). Consistent with the ECSA loss measurements determined through the ADT, Pt/SG displays the highest stability among the materials investigated, followed by Pt/G and commercial Pt/C with much poorer stability.

As Pt particle agglomeration and dissolution are among the primary mechanisms for catalyst degradation and performance loss during PEMFC operation, TEM operates as a powerful tool to investigate the morphological changes occurring in catalyst materials following ADT.[108, 109] **Figure 4-5** provides TEM images and corresponding particle size distributions after ADT for Pt/SG **(Figures 4-5 a and b)**, Pt/G **(Figures 4-5 c and d)** and Pt/C (**Figures 4-5 e and f**, with TEM images of the as-purchased Pt/C presented in **Figure A-6 in the Appendix**). Interestingly, Pt/SG still contains small Pt nanoparticles uniformly distributed across the entirety of the SG support surface **(Figure 4-5a)**. Notably, based on measurement of over 200 individual nanoparticles **(Figures 4-5a and A-7 in the Appendix)**, the average Pt nanoparticle size increases from 2.10 nm to only 2.30 nm over the course of the ADT. On the other hand, Pt/G **(Figure 4-5c)** and Pt/C **(Figure 4-5e)** nanoparticles grow much more significantly. Evidence of particle agglomeration is most pronounced with Pt/C. Specifically, the Pt nanoparticle size in Pt/G increases from 2.25 to 3.80 nm over the course of the ADT (**Figure 4-5d**), while the average size in Pt/C rises from 2.15 to as much as 5.25 nm **(Figure 4-5f)**. This provides further verification of the beneficial impact of using SG support materials that can suppress the agglomeration and growth of Pt nanoparticles during electrochemical cycling. To further experimentally investigate the interactions occurring between sulfur dopant species in SG and Pt nanoparticles, a select area of Pt/SG following ADT **(Figure 4-5g)** was subjected to high-angle annular dark field (HAADF) imaging and EDX colour mapping. ADT on this sample was conducted in the absence of binder in the catalyst ink solution in order to avoid interference from the sulfonate species present in Nafion on sulfur mapping. **Figure 4-5h** displays the HAADF image of Pt/SG, with the Pt nanoparticles clearly visible as bright spots distributed over the SG surface. This image is overlapped with the EDX colour map of Pt/SG in **Figure 4-5i**. Clearly, the Pt species (displayed in red) tend to reside in areas rich in sulfur content (displayed in green), providing further supporting evidence of the favourable interactions and binding between these species. With experimental results reflecting the improved interactions between Pt and SG and the enhanced ORR activity and electrochemical stability, we turn to first-principles computational simulations in order to gain insight into the exact nature of these enhancements.

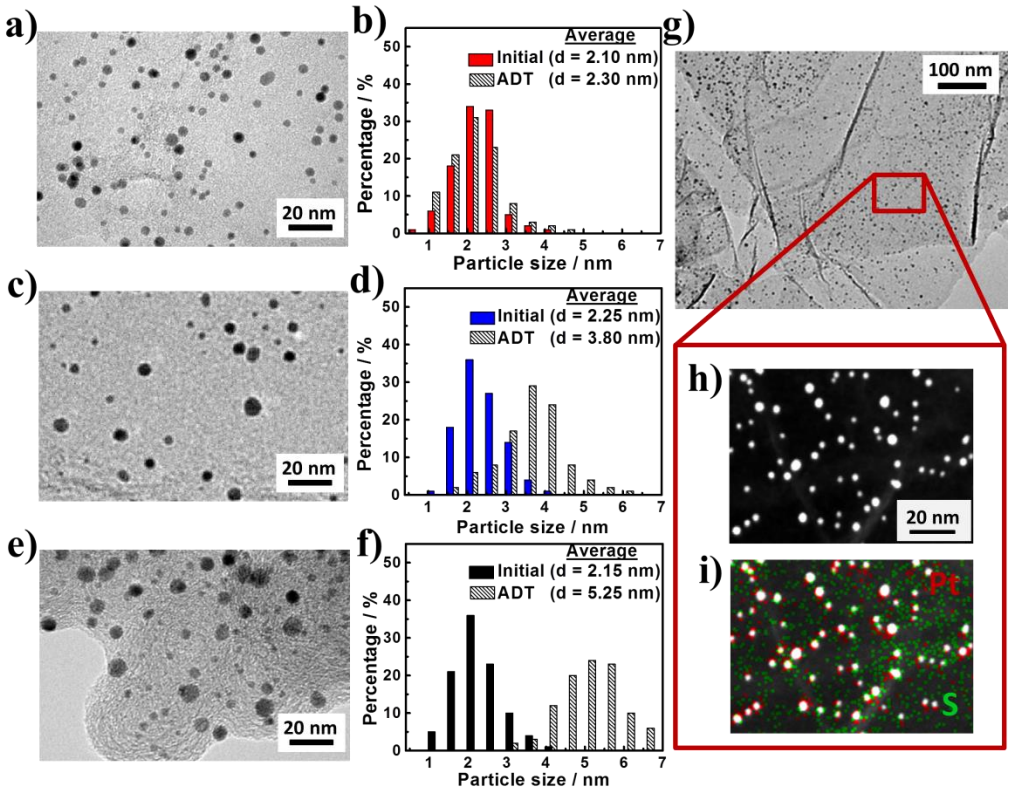

Figure 4-5 (a-f) TEM images and size distributions initially and after ADT, (g-i) Pt and S overlap.

4.3.3 Computational investigations of sulfur doping

To investigate and understand the support effects of SG, a 4 x 4 supercell of a graphene sheet **(Figure 4-6a)** is selected for the calculations. We assume that one of the carbon atoms in the graphene sheet is replaced by a sulfur atom as shown in **Figure 4-6c** and described as "graphitic S". In addition, the presence of thiophene-like sulfur (thiophene S) in a pentagonal arrangement is considered by eliminating the carbon atom adjacent to the graphitic S from the model supercell (**Figure 4-6e**). The formation energy (E_F) of each structure was calculated. E_F can be regarded as a measure of the additional stability of each structure, indicative of the energetic stability relative to that of a homogeneous local environment at the same concentrations.[110] E_F values are calculated to be 0.21 and 0.19 eV atom^{-1} for graphitic S and thiophene S, respectively. This provides indication that thiophene S formation is more favourable during SG synthesis, a conclusion that is supported by the results of XPS analysis after high temperature thermal annealing. In the case of pristine graphene, the C–C bond distance is 1.42 Å, which is very close to the experimentally measured value of 1.42 Å.[111] On

the other hand, the C-S distance in the model complex is found to change from 1.42 to 1.70 Å for graphitic S-doped graphene after relaxation, due to the difference in the atomic radius of sulfur (1.04 Å) and carbon (0.77 Å). For thiophene S-doped graphene, the C-S bond distance of 1.87 Å is even larger.

Previous investigations have linked enhanced catalytic activity and improved metallic nanoparticle dispersion to the modulated electronic structures and chemical properties of graphitic materials induced by heteroatomic doping.[111-119] Density-of-states (DOS) and projected density-of-states (PDOS) analyses can provide insight into these modifications and furthermore allow further insight into the interactions occurring between the surface of graphene and adsorbed species or reactants.[111, 115, 116, 119, 120] The results of DOS and PDOS analyses of the valence electrons of the pristine graphene and sulfur incorporated graphene materials are shown in **Figure 4-6**. Specifically, the DOS for pristine graphene reveals the conical shape near the Fermi level (**Figure 4-6b**), consistent with previous reports.[121-123] Thus, graphene is considered a semi-metal because no band gap or density of electronic states occurs at the Fermi level.[121] Thus, the electrical conductivity of these materials is governed by the Dirac equation.[123] The substitution of graphitic S into graphene results in a shift of the Fermi level towards higher energies as shown in the PDOS of the carbon atoms and the DOS of these materials (**Figure 4-6d**). Furthermore, electrons in graphitic S-doped graphene occupy the energy states at the Fermi level, implying that this material should have excellent electrical conductivity which is an important requirement of electrode materials.[124] Interestingly, the position of the Fermi level for thiophene S-doped graphene (**Figure 4-6f**) is not significantly different from that of graphene doped with graphitic S; however, a band gap appears at the Fermi level which implies that excellent electrical conductivity should not be expected for this material. Nevertheless, this is not a limiting factor for an ORR electrocatalysis support material because the band gap could be filled after the deposition of Pt atoms onto these materials.

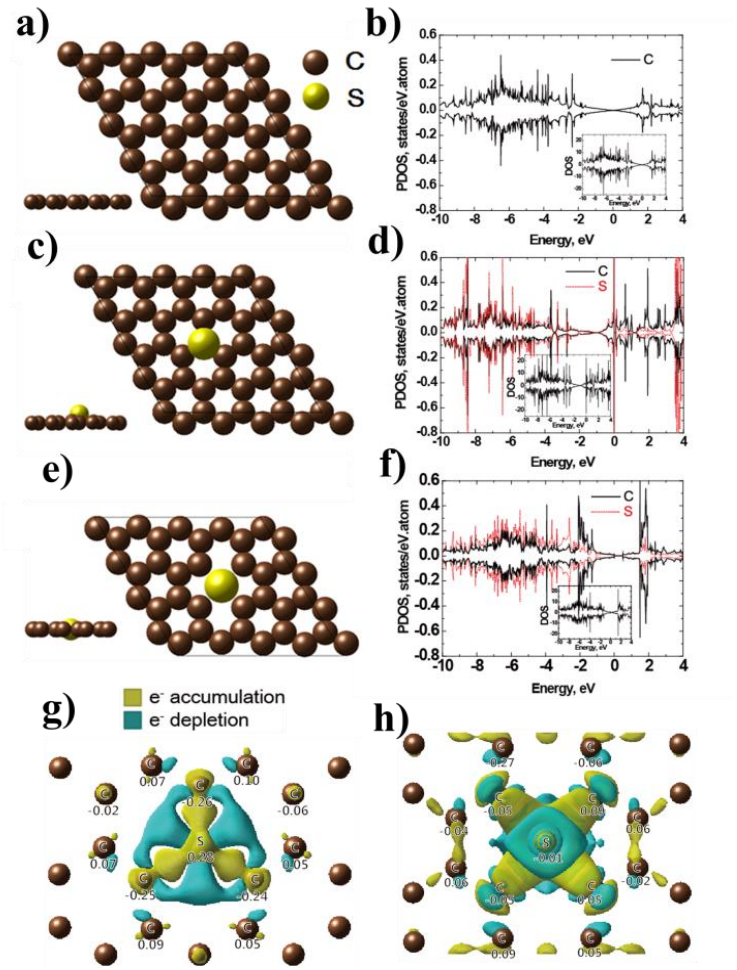

Figure 4-6 Schematic top view of the model systems (a, c, e), PDOS (b, d, f) and Charge density change of G and SG (g-h).

The atomic partial charges and changes to the charge density of individual atoms are obtained using Bader charge analysis.[125] The total number of valence electrons calculated from the Bader charge method are 128, 130 and 126 for a (4 × 4) supercell of pristine graphene, graphitic S-doped graphene and thiophene S-doped graphene, respectively. The charge of the graphitic S atom in graphene is depleted to 0.28 e **(Figure 4-6g),** whereas the thiophene S atom has a slight charge accumulation of -0.01 e **(Figure 4-6h)**. Generally, electron charge accumulation or depletion is attributed to charge transfer from atoms with lower electronegativity to atoms with higher electronegativity.[126-128] However, in the present case, the electronegativity of sulfur (2.58) on the Pauling scale is similar to that of carbon (2.55).[129] Interestingly, in graphitic S-doped graphene **(Figure 4-6g)**, the electronic charge of the sulfur atom is depleted towards the neighbouring carbon atoms which possess charge

densities varying from -0.24 to -0.26 e. Conversely, the sulfur atom in thiophene S-doped graphene has a slight charge accumulation **(Figure 4-6h)**. Clearly, these results indicate that the exact charge transfer phenomena and electronic properties of the SG materials depend on the specific arrangement of the dopant atoms. Regardless, the disruptions of the sp^2 carbon hybridization caused by heteroatomic sulfur dopants result in a change of the Fermi level and DOS of the materials that can enhance the Pt catalyst-support interactions.

4.3.4 Electronic structure analysis of Pt atoms on SG

Prior to the investigation of SG-supported Pt nanoparticles, the adsorption of a single Pt atom on a (4x4) unit cell of pristine graphene, graphitic S-doped graphene and thiophene S-doped graphene have been investigated to gain a better understanding of the interaction between the support materials and Pt and to obtain and visualize their stable configurations. For this analysis, each Pt atom is placed on the top, hollow and bridge sites of the three different unit cells to elucidate the most energetically favoured nucleation site, an important determination in order to ensure the reliability of subsequent DFT simulations. The calculations show that the Pt atom adsorbs preferentially on a C-C bridge site in pristine graphene **(Figure 4-7a)** and the bridge C-S site in thiophene S-doped graphene **(Figure 4-7c)**; on the other hand, Pt adsorbs on top of the sulfur atom in graphitic S-doped graphene **(Figure 4-7b)**. In addition, the bond length between the Pt atom and nearest adjacent carbon atom on graphitic S- (2.05 Å) and thiophene S- (2.06 Å) doped graphene is shorter than that of pristine graphene (2.08 Å). This observation is likely related to the adsorption energy between Pt and carbon (E_{ads}) on the support materials that can be calculated as follows: $E_{ads} = E_{Pt/support} - E_{Pt} - E_{support}$, where $E_{Pt/support}$ is the total energy of the support material with a single Pt atom adsorbed on it, E_{Pt} is the total energy of the Pt atom and $E_{support}$ is the total energy of the support. It has been well established that the interactions occurring between a catalyst material (i.e., Pt) and support play a significant role in the final composite structure in terms of nanoparticle size and distribution because the properties of the support directly affect the nucleation and growth processes during preparation. [54, 130, 131] The values of E_{ads} of Pt on graphitic S- and thiophene S-doped graphene are found to be -3.27 and -2.68 eV, respectively. These are more negative than that of Pt on pristine graphene (-2.01 eV), highlighting the fact that Pt adsorbs much more strongly on SG materials as a result of sulfur incorporation. This enhances the interaction between the Pt and support and facilitate Pt nanoparticle dispersion and size uniformity as indicated by the TEM analysis. Moreover, the strengthened interactions will provide a

tethering effect between the SG and Pt nanoparticles that can inhibit their self-agglomeration or dissolution under conditions such as those encountered during fuel cell operation.

4.3.5 Ab-initio simulations of Pt nanoparticles on SG

Prior to the relaxation of graphene-supported Pt, we first conduct calculations in which free-standing icosahedron Pt_{13} nanoparticles are fully relaxed to find their preferred structure under vacuum conditions. Then, this icosahedron Pt nanoparticle is deposited onto pristine graphene **(Figure 4-7d)**, graphitic S- **(Figure 4-7e)** and thiophene S- **(Figure 4-7f)** doped graphene for subsequent calculations to gain a comprehensive understanding of the previously reported excellent electrocatalyst activity and stability under acidic operating conditions. The d-band center model proposed by Nørskov *et al.*[132-138] has turned out to be very useful for describing the underlying mechanisms of experimentally observed, albeit complicated, surface catalytic reactions. Using the d-band center model, the electronic structure of the surface exposed metal layer and its inherent catalytic activity can be correlated.[135] This model relies on the assumption that the weighted average of the d-band electron energies (d-band center) of a catalyst is strongly correlated to the binding energy of the catalyst atoms with the chemical species adsorbed (e.g., oxygen).[134, 135, 137, 139] Utilizing these underlying fundamentals, Pt alloys with weaker oxygen binding energies than conventional Pt materials have been predicted to possess superior ORR activities by DFT calculations;[132-134, 137, 138] an assertion that has been confirmed by experimental observations of a variety of researchers employing extended surface and bulk catalysts.[140-143] In the case of nanoparticles however, intrinsic ORR activity enhancements cannot be exclusively linked to the d-band center theory due to complications related to the coordination environment and Pt particle size that significantly affects the ability to adsorb oxygen-containing species.[144] Nevertheless, for our present purposes, it is reasonable to quantitatively evaluate the adsorptive strengths of oxygen due to the fact these materials consist of pure Pt with minimal differences in nanoparticle size.[145] Therefore, the deposition of the icosahedron Pt_{13} nanoparticle on the G and SG materials is used as the basis to calculate the d-band center value and predict variations in the ORR activity. From the PDOS of Pt atom, d-band center values are evaluated on the graphene-based support materials using Equation (4-3):[146]

$$E_d = \frac{\int_{-\infty}^{E_F} E p_d(E) dE}{\int_{-\infty}^{E_F} p_d(E) dE} \tag{4-3}$$

Here, p_d is the density of states projected onto the d orbitals of a Pt atom. The d-band center value is determined for a Pt atom located at a vertex site near the support and found to be -2.33, -2.50 and -2.72 for graphene, graphitic S- and thiophene S-doped graphene, respectively. Independent of the arrangement of sulfur dopants within the SG, their presence alone causes the d-band center of the supported Pt nanoparticle to shift in the negative direction. This observation is consistent with a previous investigation that indicated a negative d-band shift for a Pt nanoparticle supported on CNTs functionalized with thiol groups that are not necessarily incorporated into the planar graphitic lattice of CNTs, but rather as functional species extending from the basal plane of these supports.[147] Regardless, the negative shift in the d-band center for the Pt nanoparticles supported on SG is reflected in the improved ORR kinetics of Pt/SG in comparison to Pt/G that is observed in our half-cell experimental investigations.

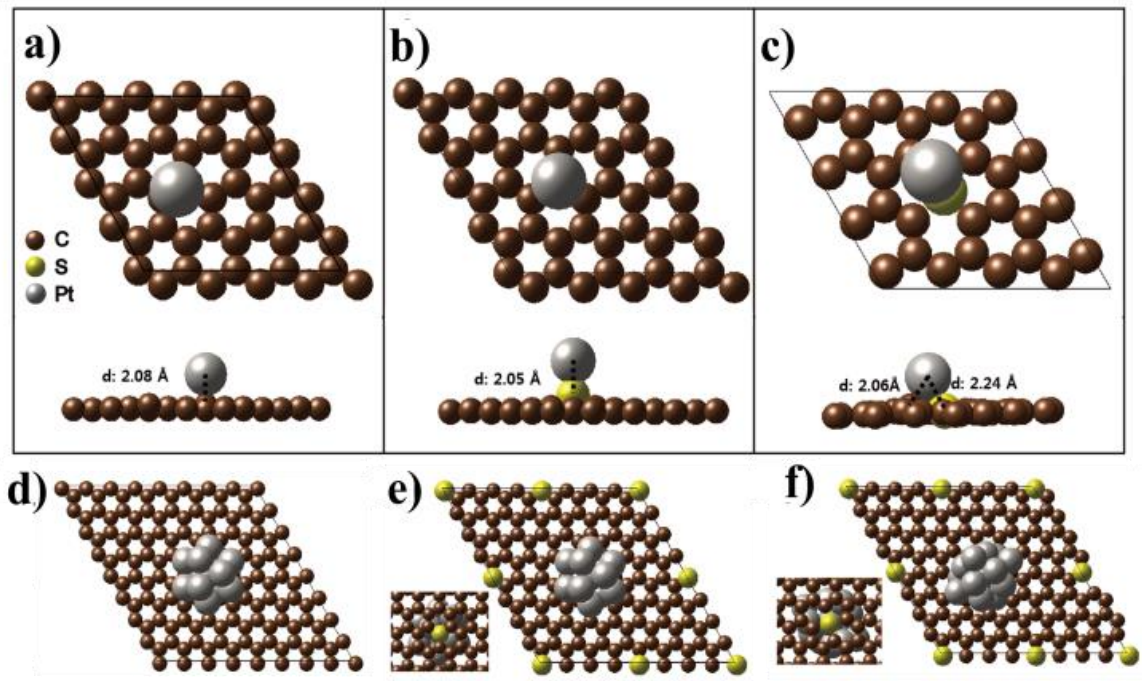

Figure 4-7 (a-c) Schematic top and side view of Pt atom adsorption on G and S, (d-f) Schematic top and bottom (inset) views of Pt atom adsorption on G and SG.

The Pt nanoparticles are stabilized by a subtle interplay occurring between the size-dependent cohesive energy per atom and the propensity for nanoparticle surface energy minimization.[148] It has been proposed that lower cohesive energies results in a lowering of the electrochemical dissolution

potential of Pt into acidic solutions.[145, 148-150] The cohesive energies of Pt nanoparticles on different support materials (E_{coh}) can be calculated using Equation (4-4):

$$E_{coh} = \frac{E_{Pt/support} - E_{support} - nE_{Pt,g}}{n} \quad (4\text{-}4)$$

Here, $E_{Pt,g}$ is the total energy of an individual Pt atom, n is the number of Pt atoms, $E_{Pt/support}$ is the total energy of the support with the Pt cluster adsorbed on it and $E_{support}$ is the total energy of the support. The cohesive energy of the unsupported Pt_{13} icosahedron is -3.62 eV taking spin-polarized calculations into consideration, a value that is consistent with previous reports.[145, 148] The values of E_{coh} for the Pt_{13} nanoparticles supported on graphene-based materials are calculated to be -3.67, -3.77 and -3.95 eV for the case of pristine graphene, graphitic S- and thiophene S-doped graphene, respectively. Clearly, the cohesive energy of Pt_{13} on graphene-based support materials is higher. Moreover and most notably, the cohesive energy of the Pt nanoparticles can be increased when using graphene doped with either graphitic- or thiophene-like sulfur species. By extension, this implies that the electrochemical dissolution potential of Pt nanoparticles supported on SG could be increased. Once again, the result of this computational analysis supports our findings that Pt/SG provides excellent electrochemical stability investigated through ADT protocols in acidic electrolyte.

4.4 Conclusions

SG materials (2.32 at. % S) were synthesizd by thermally shock/quench annealing a mixture of GO and PBS. The SG materials were used to support well-dispersed uniformly sized (ca. 2.10 nm) Pt nanoparticles for ORR catalysis. Pt/SG demonstrated excellent ORR activity based on half-cell investigations, providing a Pt-mass based current of 139 mA mg_{Pt}^{-1} at an electrode potential of 0.9 V vs RHE. This performance was superior to that of commercial Pt/C (121 mA mg_{Pt}^{-1}) and Pt/G (101 mA mg_{Pt}^{-1}) and clearly illustrated the beneficial impact of sulfur dopants in graphene supports. Notably, the outstanding electrochemical stability of Pt/SG was clearly demonstrated through ADT, displaying only an 11.2 mV decrease in the ORR half-wave potential and maintaining 87% of its initial ECSA after 1,500 potential cycles. This was a dramatic improvement over Pt/G and Pt/C, which demonstrated 23.0 and 43.0 mV losses in the half-wave potential, while retaining only 54 and 48 % of their initial ECSA, respectively. Finally, in order to investigate fundamental aspects of the role of catalyst-support interactions in these new materials, DFT computational simulations revealed that sulfur doping of graphene leads to stronger interactions with Pt, enhanced nanoparticle cohesive energies and ultimately the outstanding electrochemical stability of Pt/SG that has been observed.

Furthermore, the sulfur dopants modify the electronic properties of Pt, resulting in a negative shift in the d-band that should enhance ORR kinetics.

Chapter 5 Platinum Nanowires on Sulfur-Doped Graphene

The following section is based on previously published work by **Hoque, M. A.,** Hassan, F., Higgins, D., Choi, J-. Y., Pritzker M., Knight S., Ye S., and Chen, Z.

Advanced Materials 2015, 27(7): 1229-1234

"Multigrain platinum nanowires consisting of oriented nanoparticles anchored on sulfur-doped graphene as highly active and durable oxygen reduction electrocatalyst"

Author contributions: H.M.A conducted the material preparations, characterizations and electrochemical tests. H.M.A wrote the manuscript. C.Z. and P.M co-supervised the project. All authors reviewed the manuscript.

5.1 Introduction

Recently, one-dimensional (1D) nanostructures such as Pt nanowires have been demonstrated capable of overcoming some of the drawbacks of Pt nanoparticles in catalyzing ORR, in particular, providing much improved catalytic activity and/or durability.[65, 151-154] The durability of Pt nanowires can be further improved by growing the nanowires onto stable nanostructured support materials, such as graphene or carbon nanotubes (CNTs).[155-157] Unlike the carbon black conventionally used to support Pt catalysts, graphene in particular possesses very unique chemical, mechanical and electrical properties due to its two dimensional sp^2 hybridized carbon network.[158] Studies have additionally shown that doping graphene with heteroatoms is an effective way to tune the intrinsic properties, which is beneficial for improving electrocatalyst activity and stability.[19, 159] In our previous work, we demonstrated that sulfur-doped graphene (SG) is a highly promising support for Pt nanoparticles, providing a 14% increase in Pt-based mass activity in comparison to the state-of-the-art Pt/C and remarkable stability in terms of electrochemically active surface area (ECSA) and mass activity retention following accelerated durability testing.[160] We propose that combining the beneficial catalyst-support interactions provided by SG with Pt nanostructure control strategies (i.e., 1D nanowires) could provide further ORR activity and durability improvements to achieve practical targets for commercial devices.

Herein we report the direct synthesis of Pt nanowires on SG (PtNW/SG) by applying a simple and facile surfactant free solvothermal technique.[66] The prepared PtNWs are comprised of numerous

single crystalline nanoparticles oriented along the <111> direction, and provide increased Pt mass-based ORR activity in comparison to commercial Pt/C catalyst and PtNWs supported on graphene (PtNW/G). Most notably, PtNW/SG showed excellent stability through 3000 cycles of accelerated durability testing (ADT) in terms of both ECSA and ORR activity retention. By combining the advantages of both the 1D nanostructure of Pt and unique support materials, PtNW/SG are reported as a practical and highly promising candidate for overcoming the long term durability issues of conventional PEMFC cathode electrocatalysts.

5.2 Experimental section

5.2.1 Preparation of S-doped graphene (SG)

100 mg of graphene oxide (GO) prepared by a modified Hummer's method was mixed with 100 mg of phenyl disulfide (PDS) by grinding. The materials were loaded into a tube furnace and kept outside the heating zone until the furnace temperature reached 1000^{o}C. The sample was then slid into the heating zone where it remained for 30 minutes under argon protection, followed by cooling to room remperature. Graphene was prepared under identical conditions without PDS.

5.2.2 Preparation of S-doped graphene supported platinum nanowires (PtNW/SG)

9.2 mg of SG was dispersed by 2 hours of ultrasonication in a mixture of 12 mL ethylene glycol and 18 mL of *N*,*N*-dimethyl formaide. 30 mg of $H_2PtCl_6.6H_2O$ was then added followed by the addition of 1.5 g KOH and stirring overnight. The final solution was transferred to a 40 mL Teflon-lined autoclave and heated at 170^{o}C for 8 hours. The resultant black product was collected and washed thoroughly with ethanol and DDI water before drying in a vacuum oven at 80^{o}C. The same procedure was applied to prepare PtNW/G, with a platinum loading of 50 wt% achieved for both materials.

5.2.3 Materials characterization

The catalyst materials were characterized using scanning electron microscopy (SEM, LEO FESEM 1530), TEM (JEOL 2010F) equipped with EDS, and XRD (XRG 3000) using monochromatic Cu Kα x-rays.

5.2.4 Electrochemical characterization

1.75 mg of catalyst materials were dispersed in a solution of 1.9 mL ethanol and 0.1 mL 5wt% nafion and dropcasted on a glassy carbon electrode to achieve a loading of 22 μg cm^{-2}. CV curves were

collected at 50 mV s^{-1} in N_2-saturated 0.1M $HClO_4$ and ORR measurements at 5 mV s^{-1} under O_2-saturation with electrolyte resistance correction applied. To improve the dispersion of nanowire catalyst on the electrode, 20 wt% carbon black (Vulcan XC-72) was added to the suspension.

5.3 Results and Discussion

SG with a sheet like morphology **(Figure 5-1a)** was prepared and found by x-ray photoelectron spectroscopy (XPS) to possess a surface sulfur content of 1.05 at.%, consisting primarily of thiophenic species **(Figure A-8 in the appendix)**. After the solvothermal synthesis of PtNW on the SG, the overall morphology of the materials is shown in **Figure 5-1b**. A variety of nanowire diameters ranging from 3 to 25 nm are observed, along with nanowire lengths in excess of 1 μm **(Figure 5-1c)**. The crystal structure of Pt nanowires was confirmed to be Pt-fcc (JCPDS No. 04-0802) based on the x-ray diffraction (XRD) peaks shown in **Figure A-9 in the appendix**, with diffraction patterns of commercial Pt/C and PtNW/G shown for reference. High resolution transmission electron microscopy (HR-TEM) images of the Pt nanowires shown in **Figure 5-1d** indicate that the nanowires are composed of numerous attached Pt crystals oriented along the <111> direction, with a measured d-spacing of 2.24 Å corresponded to the (111) facet. Interestingly, Pt nanowires with different diameters possess the same crystallographic orientation along the <111> direction as shown from a HRTEM image of a nanowire possessing a smaller diameter (ca. 7nm) in **Figure A-10 in the appendix.** For comparison, the structure of undoped graphene and PtNW/G are shown in **Figure A-11a** and **b in the appendix**, respectively. We investigated the time dependent growth mechanism of Pt nanowires on SG and the results are shown in **Figure 5-1f** through **j**. After just 10 minutes of reaction, growth is initiated by the nucleation of nano-sized Pt particles on the surface of SG **(Figure 5-1f)**. After 1h, the number of nanoparticles on SG increases significantly, and side by side attachment is observed **(Figure 5-1g)**. Interestingly, after 2h, the process of attachment and coalescence of nanoparticles eventually occurrs to the point that nanorods are formed **(Figure 5-1h)**. This process is continued with an increase in reaction time to 4h, where it can be clearly seen in **Figure 5-1i** that the nanoparticles have attached together to form nanowires with larger lengths, and finally,after 6h, smooth, continuous nanowires are obtained **(Figure5- 1j)**. Based on these observations, it appears that the PtNWs evolve from the preferential attachment and crystallographic arrangement[161, 162] along the <111> direction, rather than a seed-initiated growth process.[163]

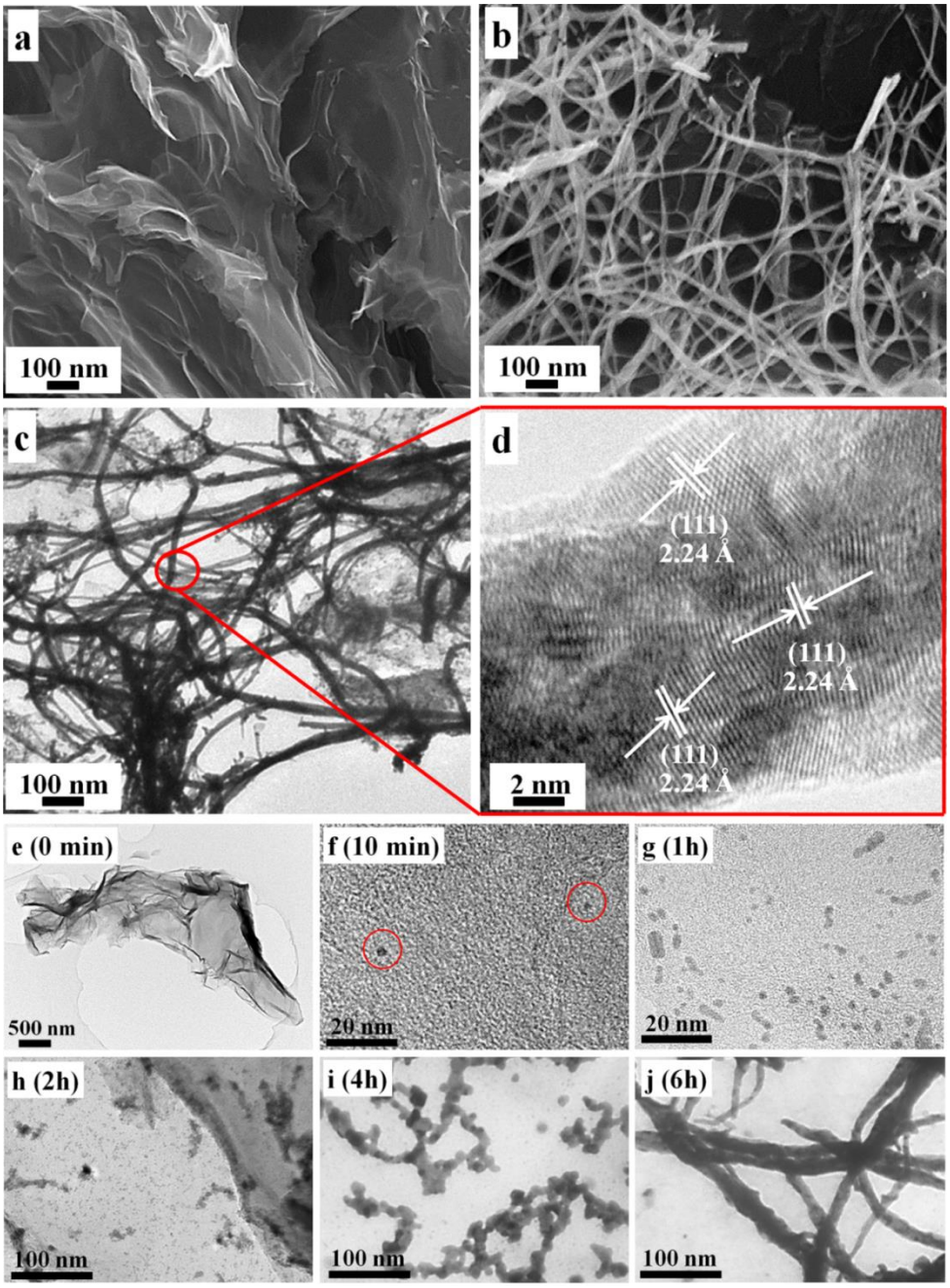

Figure 5-1 (a-d) SEM and TEM images of SG and PtNW/SG, (e-g) Growth of nanowires.

The electrochemical properties and stability of the various catalyst materials were investigated using cyclic voltammetry (CV) in 0.1 M $HClO_4$. CV curves before and after accelerated durability testing (ADT), which involved subjecting the catalyst to 3000 potential cycles between 0.05 and 1.5 V vs. RHE, are shown for PtNW/SG, PtNW/G and commercial Pt/C in **Figure 5-2a, b and c**, respectively.

It should be noted that the ADT conditions employed are very harsh and include the potential regions in which repeated Pt oxidation/reduction and carbon corrosion will occur.[164] After ADT, additional redox peaks appear in the range of 0.50 to 0.75 V vs. RHE. These peaks likely arise due to the formation of quinone/hydroquinone redox species under the high potentials encountered during ADT. The electrochemically active surface area (ECSA) of the various catalysts was calculated by integrating the hydrogen adsorption-desorption region[49] with ECSA values of 24.5, 24.0 and 53 m^2 gm_{Pt}^{-1} determined for PtNW/SG, PtNW/G and Pt/C, respectively. The reduced ECSA of PtNW/SG and PtNW/G in comparison to Pt/C is to be expected, owing to the thicker diameter and anisotropic structure that results in a lower degree of Pt-atom exposure.[165, 166] Normalized ECSA values obtained after a varying number of ADT cycles are shown in **Figure 5-2d**. It can be seen that after 3000 cycles, PtNW/SG loses only 42% of its initial ECSA, whereas the losses in ECSA for PtNW/G and Pt/C are 72 and 99%, respectively. These results exemplify the excellent stability of PtNW/SG in comparison to PtNW/G and commercial Pt/C cunder the harsh potentiodynamic conditions of ADT. In our previous study,[160] we found that Pt nanoparticle ECSA losses could also be significantly mitigated using SG supports, owing to the strengthened adsorptive and cohesive interactions induced by sulfur dopant atoms on Pt atoms and nanoclusters, respectively. The current results indicate a similar effect in PtNW/SG based on the significant improvements in ECSA retention observed in comparison to PtNW/G. To investigate the impact of nanostructure control (i.e., nanowires), the as prepared PtNW/G was compared with Pt nanoparticles supported on un-doped graphene (PtNP/G). Electrochemical testing results provided in **Figure A-12 in the appendix** demonstrate that PtNW/G shows clear stability enhancements in comparison to PtNP/G, albeit not to the extent observed in the presence of sulfur-doping. This stability enhancement could likely arise owing to surface of the PtNWs that consists primarily of (111) facets, the most thermodynamically favourable configuration, as the (111) planes possess the lowest surface energy of all the low-index crystallographic planes of Pt.[3]

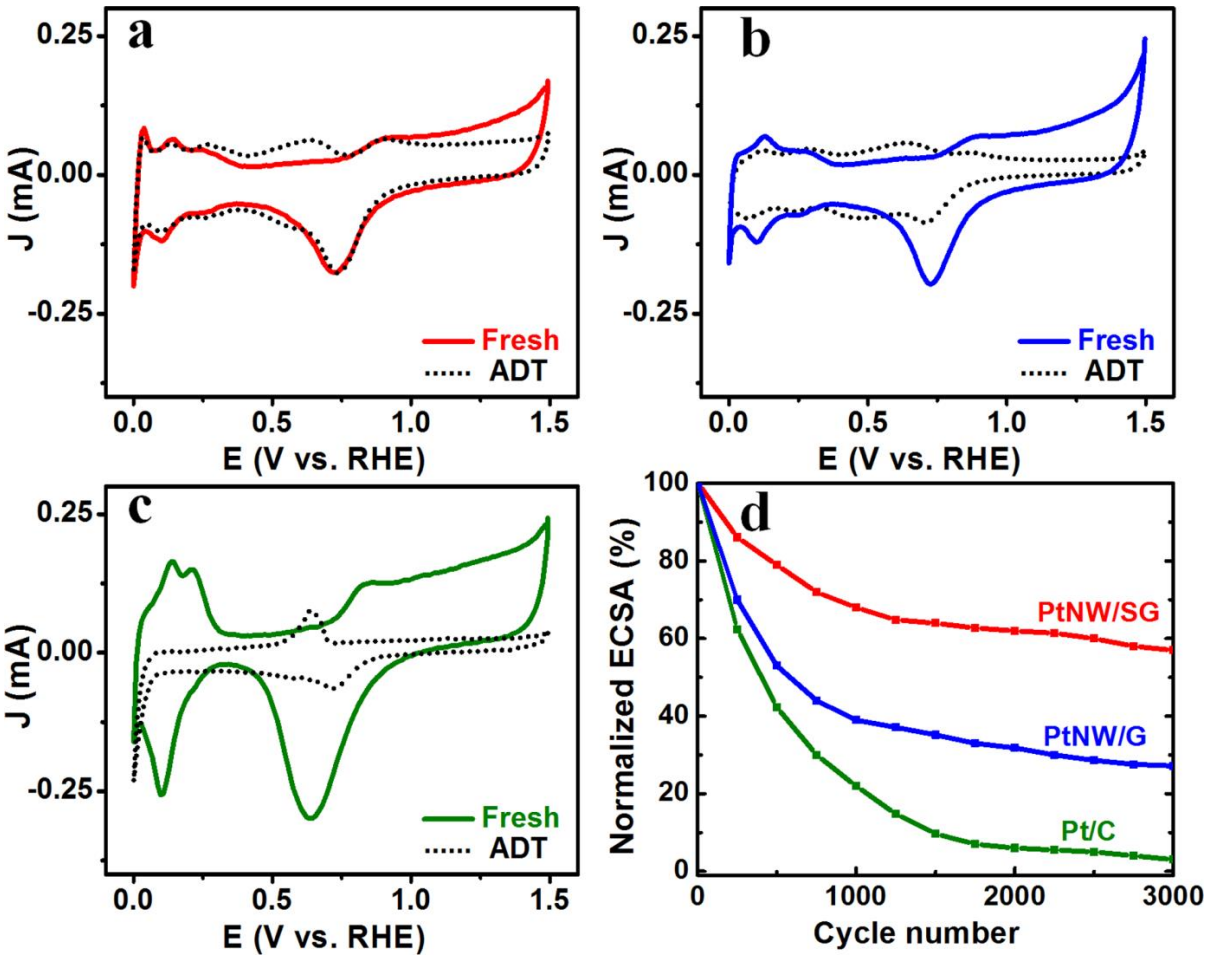

Figure 5-2 CV curves for (a) PtNW/SG, (b) PtNW/G, (c) Pt/C. (d) Effect of cycle number on normalized ECSA.

The ORR activity of PtNW/SG before and after ADT was investigated in oxygen saturated 0.1 M $HClO_4$. Initially at 0.9 V vs. RHE, an improved Pt-based mass activity of 167 mA mg_{Pt}^{-1} was observed for PtNW/SG in comparison to PtNW/G (132 mA mg_{Pt}^{-1}) and commercial Pt/C (125 mA mg_{Pt}^{-1}). Moreover, PtNW/SG showed a very high specific activity of 0.675 mA cm^{-2}_{Pt} **(Figure 5-3d-inset)**, approaching the U.S. Department of Energy (DOE) target of 0.720 mA cm^{-2}_{Pt}[167] while PtNW/G and Pt/C demonstrated specific activity values of 0.543 and 0.250 $mAcm^{-2}_{Pt}$, respectively. This specific activity enhancement is attributed to the preferential exposure of the (111) facet of the PtNWs that provides higher activity than the (100) facets[168-170] that are abundant in nanoparticle configurations.[3] Additionally, the 1D extended nanostructure of the PtNWs leads to a a reduced fraction of defect, step and edge sites that bond spectator species (OH_{ad}) too strongly, thereby

impeding the ORR kinetics.[170-173] On the other hand, it is very likely that the improved activity of PtNW/SG in comparison to PtNW/G arises due to the beneficial catalyst-support interactions occuring between Pt and the sulfur dopants present in SG.[160]

Polarization curves obtained before and after ADT are shown in **Figure 5-3a, b and c** for PtNW/SG, PtNW/G and Pt/C, respectively. After ADT, PtNW/SG shows only a 22 mV loss in half-wave potential, significantly better than the 86 mV half-wave potential loss for PtNW/G and almost complete loss of performance for commercial Pt/C. A comparison of Pt-based mass activities before and after ADT is given in **Figure 5-3d**. Notably, PtNW/SG demonstrated a mass activity of 112 $mAmg_{Pt}^{-1}$ at 0.9 V vs. RHE after ADT, representing 67% of its initial activity. PtNWG and Pt/C on the other hand showed mass activity values of 22 and 0.5 $mAmg_{Pt}^{-1}$ following ADT, corresponding to only 17% and < 1% of their initial activity, respectively. We additionally investigated the stability of PtNW/SG using the DOE recommended durability testing protocol that involves 30,000 potential cycles between 0.6 and 1.0 V vs. RHE in O_2 saturated 0.1M $HClO_4$ solution.[4, 154, 174] Once again, the ECSA and ORR activity retention of PtNW/SG was superior to that of commercial Pt/C **(Figure A-13 in the appendix)**. Following this testing, the ECSA retention for PtNW/SG and Pt/C were approximately 65 and 33%, respectively, and the losses in half-wave potential were approximately 50 and 250 mV, respectively. Moreover, we collected CV curves of PtNW/SG after 6000 cycles (**Figure A-13(inset) in the appendix**) and obseved only a 12% loss in ECSA. This is a significant improvement over the 30% ECSA loss observed by Lim *et al.*[175] for unique Pd-Pt nanodendrites after only 4000 cycles, although with a slightly higher upper potential limit (0.6 to 1.1 V vs. RHE). Our results are in more close agreement with the results of Ruan *et.al.*[176] who reported an ECSA loss of 14.2% after 6000 cycles for ultrathin Pt nanowire networks, although the Pt mass and specific activities of our PtNW/SG were significantly higher (16 and 385%, respectively).

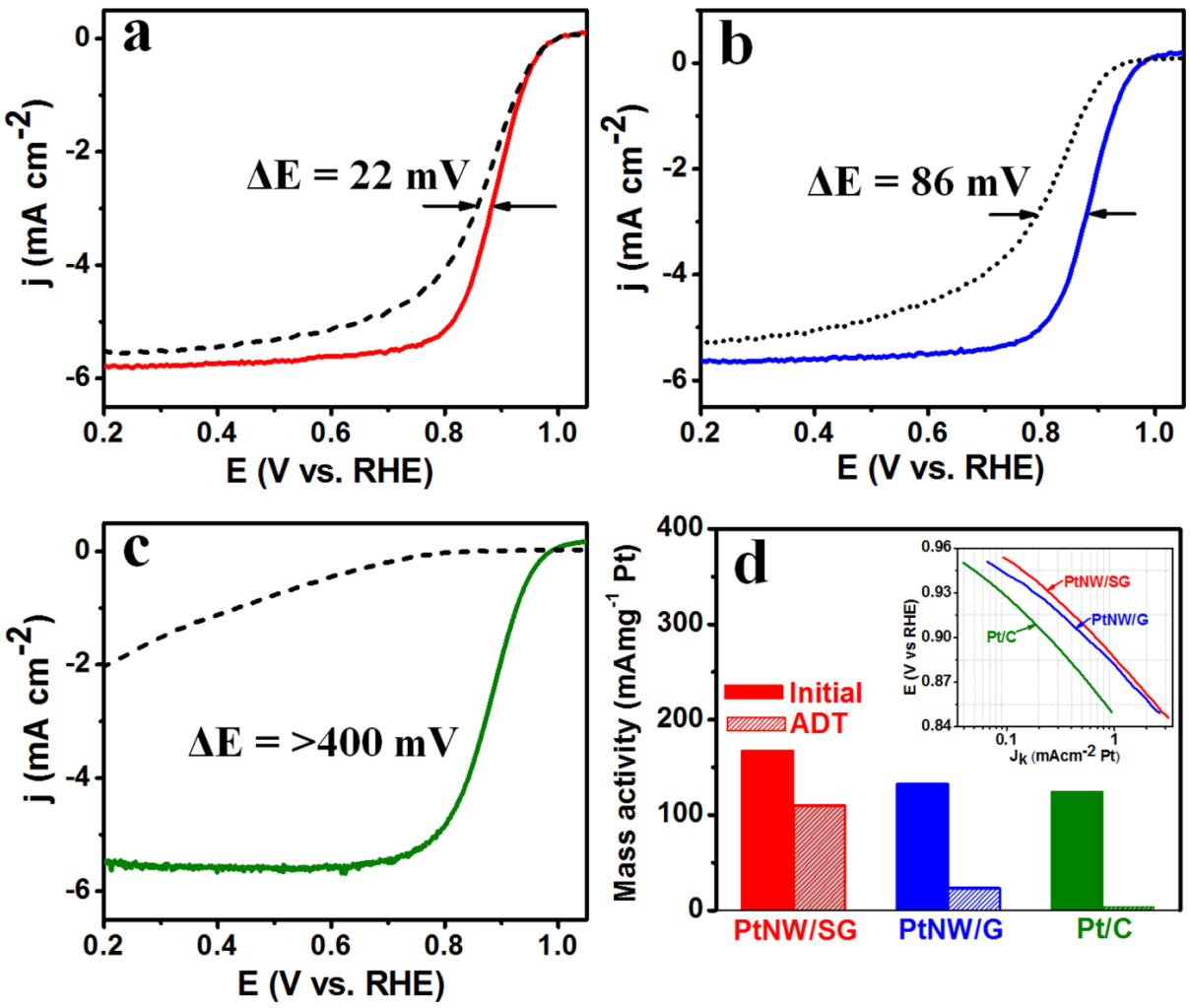

Figure 5-3 Voltammograms for the ORR on (a) PtNW/SG (b) PtNW/G and (c) Pt/C. (d) Comparison of Pt mass-based specific activity among the different catalysts.

Since the performance degradation of electrocatalyst materials is an important issue, we investigated the morphological and structural changes of the catalysts following ADT. After 3000 cycles, PtNWs were still observed to be anchored on the surface of SG **(Figure 5-4a)** with a crystallographic orientation in the <111> direction **(Figure 5-4b)**. An energy dispersive spectroscopy (EDS) elemental map of PtNW/SG after ADT is shown in **Figure 5-4c**, demonstrating the locations of carbon, sulfur and platinum species. To avoid interference of the sulfonate species present in Nafion, a binder-free ADT test was conducted for the purpose of elemental mapping. Interestingly, sulfur atoms are consistently observed to be well distributed along the lengths of the PtNWs, indicating that these sulfur species serve as anchors to adhere the nanowires to the surface of the SG.[177] This is supported

by our recent findings through an *ab initio* approach that highlighted stronger adsorption of Pt on SG (-2.68 eV) compared to pure graphene (-2.01 eV), and an enhanced Pt nanoparticle cohesive energy of -3.95 eV versus -3.67 eV, respectively.[160] For full details of the DFT calculations, please refer to the previously published manuscript and supporting information.[160] On the other hand, the structure of PtNW/G was more vulnerable to ADT conditions, with PtNW degradation and aggregation observed, along with the formation of nanoparticle agglomerates on the graphene surface **(Figure 5-4d)**. The harsh ADT conditions also had a significantly detrimental effect on the structure of Pt/C **(Figure A-14 in the appendix)**, demonstrating dramatic Pt nanoparticle growth and agglomeration.

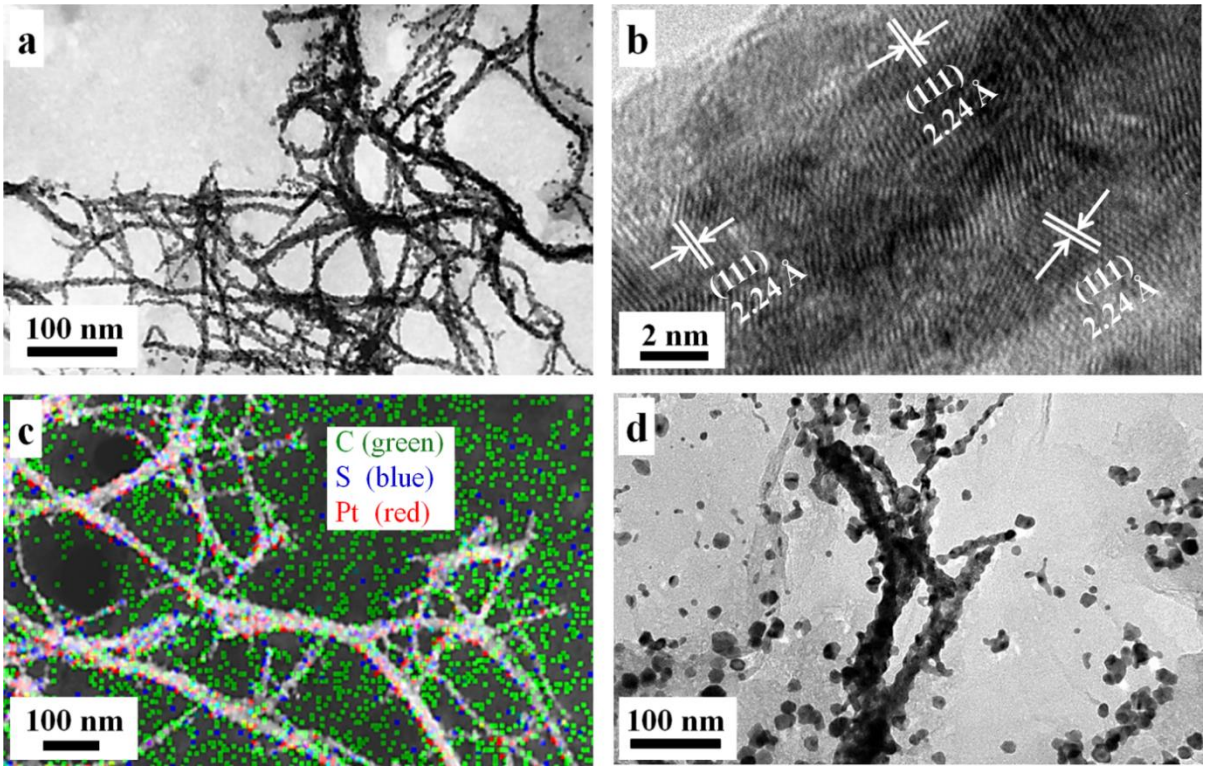

Figure 5-4 (a,b) TEM images and (c) EDS mapping of PtNW/SG, (d) TEM image of PtNW/G.

5.4 Conclusions

In conclusion, SG was prepared as a support for the direct growth of platinum nanowires. Investigation of the growth mechanism of Pt nanowires on SG revealed that the nanowires are comprised of numerous single crystalline nanoparticles attached and oriented along the <111> direction. Notably, PtNW/SG exhibited excellent electrochemical ORR activity and stability in comparison with PtNW/G and commercial Pt/C catalysts under harsh, potentiodynamic conditions.

After 3000 ADT cycles, PtNW/SG retained 58% of its initial ECSA, superior to only 28% and 1% retained by PtNW/G and commercial Pt/C, respectively. Additionally, PtNW/SG retained 67% of the Pt-based mass activity, whereas the mass activity retention of PtNW/G and commercial Pt/C were 17% and < 1%, respectively. PtNW/SG also exhibited increased Pt-mass based activity, with an excellent specific activity of 0.675 mA cm^{-2}_{Pt}, approaching the DOE recommended target of 0.720 mA cm^{-2}_{Pt}.

Chapter 6 Sensitivity Analysis of Sulfur-Doped Graphene

The following section is based on previously published work by **Hoque, M. A.,** Hassan, F., Seo, M. H., Choi, J-. Y., Pritzker, M., Knights S., Ye, S., and Chen, Z.

Nano Energy 2016, 19: 27-38

"Optimization of sulfur-doped graphene as an emerging platinum nanowires supports for oxygen reduction reaction"

Author contributions: H.M.A conducted the material preparations, characterizations and electrochemical tests. H.M.A wrote the manuscript. S.M.H performed the DFT analysis. C.Z. and P.M co-supervised the project. All authors reviewed the manuscript.

Reproduced with permission from Elsevier.

6.1 Introduction

The kinetic limitations of the cathodic oxygen reduction reaction (ORR) must be overcome to meet the practical demands for polymer electrolyte membrane fuel cells (PEMFCs) [172, 178-181]. The observed overpotential is attributed to the slow kinetics of ORR occurring on the conventional carbon supported platinum nanoparticle (Pt/C) catalysts [182-184]. These zero dimensional (0D) nanoparticulate electrocatalysts lack activity due to a high number of defect sites, lattice boundaries and low coordination atoms on the surface that results from their very small size. This leads to the strong adsorption of oxygen containing species (*i.e.*, OH groups) and thereby decreases the number of active platinum sites available for the ORR [154, 185-187]. Stability is another pertinent concern, whereby Pt/C degrades during PEMFC operation due to carbon corrosion and/or platinum nanoparticles agglomeration, dissolution and Ostwald ripening [166, 188, 189].

In contrast to nanoparticles, one dimensional (1D) nanostructures, such as platinum nanowires, have been highly touted as promising solutions to the inherent activity and durability issues associated with state-of-the-art nanoparticle catalysts [65, 152, 153, 190-192]. These 1D platinum morphologies provide significant advantages owing to their unique anisotropic structure and surface properties that lead to excellent electrocatalytic activity and durability [66, 154, 165]. In particular, platinum nanowire morphologies minimize the number of undesirable low-coordination defect sites due to their preferential exposure of smooth crystalline planes [193-195]. Therefore, the cathodic overpotential caused

by adsorbed oxygen-containing species can be significantly suppressed, leading to an increase in ORR kinetics [196, 197].

The performance of platinum nanoparticles or nanowires can be further improved by growing them onto a variety of stable supports, including mesoporous carbon, carbon nanofibers, carbon nanotubes and graphene [155-157, 159, 160, 198-200]. Among these supports, graphene has significant application potential owing to its unique properties[201]. The two dimensional sp^2 bonded hybridized carbon network in particular possesses outstanding mechanical, chemical and electrical properties that are ideal for electrochemical applications[158]. Both theoretical calculations and detailed experiments have shown that the intrinsic properties of graphene can be modified by the introduction of heteroatoms, such as sulfur, nitrogen, phosphorus or boron into the carbon framework [27, 160, 202]. A lot of research has been carried out to investigate nitrogen-doped carbon materials as platinum catalyst supports, with enhancements to both the ORR activity and electrochemical stability [203-207]. We were however the first to develop sulfur-doped graphene (SG) as a platinum catalyst support, capable of providing remarkable activity and durability improvements [160, 198]. Through detailed density functional theory (DFT) calculations and experimental investigations, we demonstrated that platinum binds strongly to SG. These strong catalyst-support interactions lead to an enhancement in Pt stabilization, along with modulated electronic properties that provide ORR activity enhancements. The amount of sulfur in SG very likely has a significant impact on the interactions with platinum, owing to its influence on the electrical and chemical properties of the resulting catalyst. Therefore, detailed knowledge of the sulfur concentration dependency of the electro-kinetic parameters for oxygen reduction, along with the physicochemical properties of the developed catalysts is of importance. This fundamental insight is essential to the design and development of optimal Pt-SG catalysts.

In this report, we provide an extensive investigation to elucidate the effect of sulfur concentration on the oxygen reduction performance of SG supported platinum nanowires (PtNW/SG). We examine the morphologies, structural and electrical properties of PtNW/SG with different sulfur contents, and then investigated the electrochemical kinetic parameters such as Tafel slope, exchange current density and activation energy towards oxygen reduction. These detailed experimental investigations are also linked to computational simulations to systematically elucidate the impact and contribution of sulfur on the ORR activity of PtNW catalysts.

6.2 Experimental Section

6.2.1 Synthesis of Graphene Oxide (GO)

Graphite powder (Alfa Aesar, natural, microcrystal grade, APS 2-15 micron, 99.9995%) was oxidized by an improved Hummers method in order to obtain GO [80]. Briefly, 2 g of graphite powder was added to a mixture of concentrated H_2SO_4/H_3PO_4 (360:40 mL) in a triangular shaped conical flask. After 30 minutes of magnetic stirring, 18 g of $KMnO_4$ was added very slowly and the reaction was heated to 50^{o}C and held for 16 hours. Once the reaction was completed, the temperature was cooled down to ca. 10^{o}C in an ice container and then 400 mL of DDI H_2O was added in a dropwise fashion. 15 mL of H_2O_2 (30%) was then added to complete the oxidation reaction. The final mixture was centrifuged and washed with water, ethanol and HCl (30%), and then freeze dried for 3-4 days.

6.2.2 Synthesis of SG and G

Graphene with different sulfur concentrations was prepared by a thermal shock/quench annealing process. Briefly, 120 mg of GO and the desired amount of phenyl disulfide (PDS, Sigma Aldrich) were mixed together by grinding. Different sulfur contents were achieved by adding 10, 60, 240 and 480 mg of PDS to the mixture. This mixture was then transferred into a quartz tube for annealing at 1000 °C for 30 min under Ar atmosphere [160]. This was accomplished by keeping the sample upstream (out of the heating zone) while the furnace reached the desired temperature, at which point it was inserted into the heating zone. After the desired reaction time, the sample was removed from the heating zone so that it would cool rapidly. Pure graphene was also synthesized by directly annealing GO under the same conditions.

6.2.3 Synthesis of PtNW/SG and PtNW/G

To grow platinum nanowires onto the SG, 20 mg of SG was first dispersed by ultrasonication for at least 2 hours in a mixture of 4 mL ethylene glycol (EG) and 6 mL of *N*,*N*-dimethyl formaide (DMF). 53 mg of $H_2PtCl_6.6H_2O$ was then added to the solution, followed by the addition of 0.5 g KOH. The resultant solution was magnetically stirred overnight and then transferred into a 20 mL Teflon-lined autoclave to heat in a convection oven at 170^{o}C for 8 hours. The final material was collected for thorough washing with ethanol and DDI water before drying in a vacuum oven at 80^{o}C. Using this method, a platinum loading of 50 wt% was achieved. The same procedure was applied to prepare platinum nanowires supported on pure graphene (PtNW/G).

6.2.4 Material characterization

The samples were characterized by transmission electron microscopy (TEM, Zeiss Libra 200 MC) equipped with EDX for elemental mapping, Raman spectroscopy (SENTERRA 314), XRD (Inel XRG 3000 diffractometer), X-ray photoelectron spectroscopy (XPS, PHI Quantera) and scanning electron microscopy (SEM, LEO FESEM 1530) equipped with EDX. The optical properties of the prepared SG samples were analyzed by UV-visible spectroscopy (Ocean Optics, DT-MINI-2-GS). Linear polarization (LPR) was carried out on a 2-point probe system to obtain the electrical conductivity of G, SGs and GO prepared under different conditions [208].

6.2.5 Electrochemical characterization

To conduct electrochemical testing of the catalyst materials, the electrode was prepared by dispersing 2 mg of catalyst materials in a solution containing 0.95 mL ethanol and 0.05 mL 5% Nafion. The electrode loading of the different nanowire catalysts and the commercial state-of-the-art Pt/C (TKK, 28.2 wt.% Pt) was controlled to be 22 μgPt cm^{-2}. Cyclic voltammetry (CV) curves were collected at a scan rate of 50 mV s^{-1} in N_2-saturated 0.1M $HClO_4$ and the ORR measurements were conducted at a scan rate of 5 mV s^{-1} in O_2-saturated 0.1M $HClO_4$ at room temperature. Accelerated durability testing (ADT) was performed by cycling the electrode potential 1000 times in a N_2-saturated electrolyte between 0.05 and 1.5 V vs. RHE at a scan rate of 50 mV/s. The temperature dependent kinetic parameters for ORR on oxide-covered and oxide-free platinum surfaces of the different catalysts were calculated at atmospheric pressure. Throughout the electrochemical investigations, the temperature was varied from 20 to 50°C using a water bath (Polystar®-Cole Polymer®) and the cell temperature was initially maintained at 20°C for at least 2 hours in order to ensure thermal equilibration [209]. A potential scan between 0.05 and 1.5 V vs RHE at a scan rate of 50 mV s^{-1} in O_2-saturated 0.1 M $HClO_4$ was applied during the equilibration period to maintain the electrode in an activated state. Then, slow scan voltamograms for oxygen reduction were collected by sweeping the potential from 0.3 to 1.2 V vs RHE at scan rate of 1 mV s^{-1} [210]. In this way, all the kinetic parameters were calculated at each temperature. Moreover, the temperature was subsequently lowered back to check for hysteresis. It should be noted that all of the results were electrolyte resistance corrected [211]. 20 wt% carbon black (Vulcan XC-720) was added to the suspension in order to improve the dispersion of the nanowire catalyst on the glassy carbon electrode.

6.2.6 Computational methods

The total internal energies of G and SG were calculated using the Vienna *ab initio* simulation package (VASP) program [212] with the implemented DFT method [82, 83]. The pseudo-potentials through the projector augmented wave (PAW) method were used to replace the interaction potential of the core electrons [88, 213]. The Perdew, Burke and Ernzerhof (PBE) functional was employed to describe the electron exchange-correlation energy [85], employing the spin-polarized generalized gradient approximation (GGA) [86, 214]. The valence electrons expressed by Kohn-Sham wave functions were expanded with a plane-wave basis set. A gamma point mesh with (9 × 9 × 1) k-points was employed for the G and SG unit cell to sample the Brillouin zone, and utilized the Methfessel-Paxton smearing method [215]. The energies were cut off at 520 eV. During optimizing structural, whole ions were completely relaxed until the internal energies were converged within 10^{-4} eV. To calculate DOS of surface, the surface of G and SG were generated through the expansion of the (1 × 1) unit cell, and a vacuum space of 13 Å was employed. The tetrahedron method was used with Blçchl's corrections [90] for the density of states (DOS) calculations.

6.3 Results and discussion

6.3.1 Physico-chemical characterization

Figure 6-1a depicts a TEM image that represents the general graphene morphology of all SG materials. An EDX elemental map was carried out on each sample and the distribution of sulfur species were depicted in **Figure 6-1b (i-iv)**. It was observed that sulfur atoms are well distributed and the amount of sulfur increases with increased amounts of PDS added during synthesis. Using both EDX and XPS (**Table A-2 in the appendix**), the sulfur contents of SG were 0.35, 1.40, 2.70 and 3.95 at%, corresponding to the addition of 10, 60, 240 and 480 mg of PDS during synthesis, respectively. These materials are named in order of increasing sulfur content as SG-1, SG-2, SG-3 and SG-4. The morphologies of the PtNW after deposition on SG-2 were investigated using TEM as shown in **Figure 6-1c**. The diameter of the nanowires was in the range of 3-30 nm, along with nanowire lengths in excess of 1 μm. We conducted elemental line scans to locate carbon, sulfur and platinum species along both the length and cross section of the nanowires, shown in **Figure 6-1d (i-ii)**. Interestingly, the composition profile of the sulfur atoms closely matched that of platinum. One may consider that this is due to the presence of free sulfur species "poisoning" the surface of the platinum nanowires, owing to the affinity between these two atoms. To exclude this, EDX spectra were

collected from a PtNW that extends beyond the surface of the underlying SG-2 support. No sulfur was detected during this scan, suggesting that the similar composition profile of sulfur and platinum is due to the sulfur species within SG acts as anchoring sites for the PtNWs. In our previous studies [198] it was shown that the Pt nanowires grow directly onto SG, and are comprised of numerous single crystalline nanoparticles oriented along the <111> direction. TEM images and the corresponding cross sectional diameter distribution of the nanowires obtained by PtNW/G, PtNW/SG-1, PtNW/SG-2, PtNW/SG-3 and PtNW/SG-4 are shown in **Figure A-15 to A-19 in the appendix**. Interestingly, a major portion of nanowires having small sized diameter was observed for PtNW/SG-2 in comparison to other catalysts. For example, the distribution of diameter of the nanowires was dominant in the range of 8-23 nm for PtNW/G (**Figure A-15**), 8-18 nm for PtNW/SG-1 (**Figure A-16**), and 4-16 nm for PtNW/SG-2 (**Figure A-17**). However, PtNW/SG-3 possess relatively larger diameters, (i.e., 20) nm along with some nanoparticles agglomerated in an elongated structure (**Figure A-18**) that we have previously shown as one of the steps of platinum nanowire growth [198]. On the other hand, the formation of nanowires was significantly interrupted in the case of PtNW/SG-4 and a high proportion of these elongated nanoparticle agglomerates was observed **(Figure A-19**). XRD was used to confirm that all of these structures were in fact fcc phase platinum (**Figure A-20 in the appendix**).

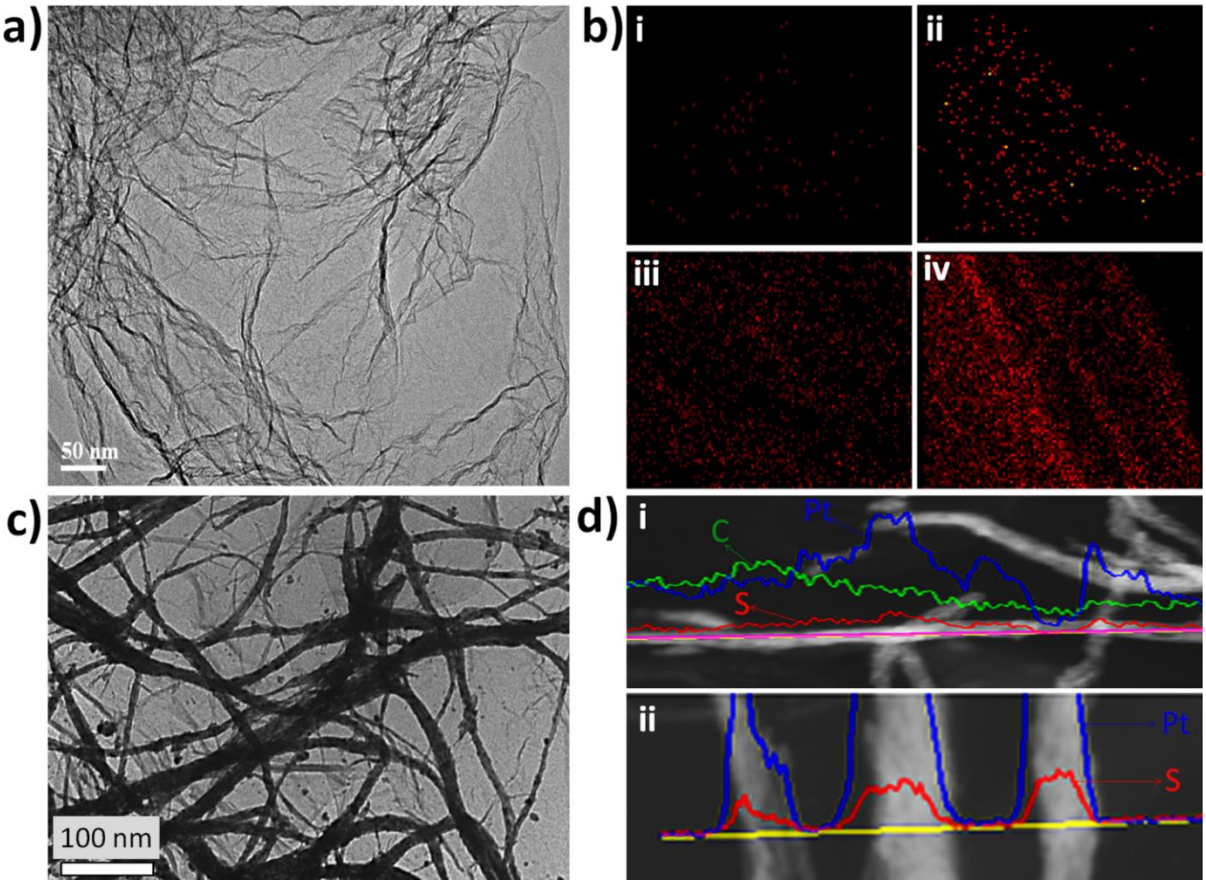

Figure 6-1 (a-b) TEM and S maps on SGs c) TEM image of PtNW/SG-2 and d) EDX line scans.

The nature of chemical bonding in SG was investigated by XPS. **Figure 6-2 (a-d)** show the characteristic C 1s peak obtained for the various SG materials. The typical C 1s region was deconvoluted into different envelopes, corresponding to the following bonds: sp^2 C=C (284.5 eV), sp^3 C-C (285.1 eV), C-O (286.2 eV), C=O (287.2), O-C-O (288.9 eV) and Π-Π* transitions in delocalized sp^2 bonded carbon structures (>290 eV) [216]. These peak deconvolutions allowed for measurement of the ratio of sp^2 to sp^3 bonded carbon contents [216-219] with the values of 2.05, 1.86, 1.45 and 1.1 for SG-1, SG-2, SG-3 and SG-4 respectively. It is interesting to note that the concentration ratio of sp2:sp3 carbon decreases significantly with increasing sulfur contents in SG. This is to be expected, as the content of dopant species is commonly linked to decreased degrees of graphitization [220, 221]. In reality, a fraction of edge/defect sites always exist in the graphene and with increasing amount of Phenyl disulfide (PDS) during synthesis, those fractions can be affected significantly that leads to higher amounts of sp3 bonded carbon. Also, the S 2p XPS spectra for SG-1,

SG-2, SG-3 and SG-4 are shown in **Figure A-21a in the appendix**. The peaks observed at 163.8 and 165.1 eV suggest the presence of thiophenic sulfur dopants, whereas the peaks above 165.5 eV are assigned to –C-SO_x- species [19, 159]. In addition with S peak analysis, the fitted Pt $4f_{7/2}$ and $4f_{5/2}$ peaks at 71.6 and 75.2 eV, respectively, for SG-1, SG-2, SG-3 and SG-4 are also shown in **Figure A-21b in the appendix**. It should be noted that no significant structural changes were observed in the S and Pt spectra of the different SG samples, in contrast to the noticeable changes in the carbon bonding configuration.

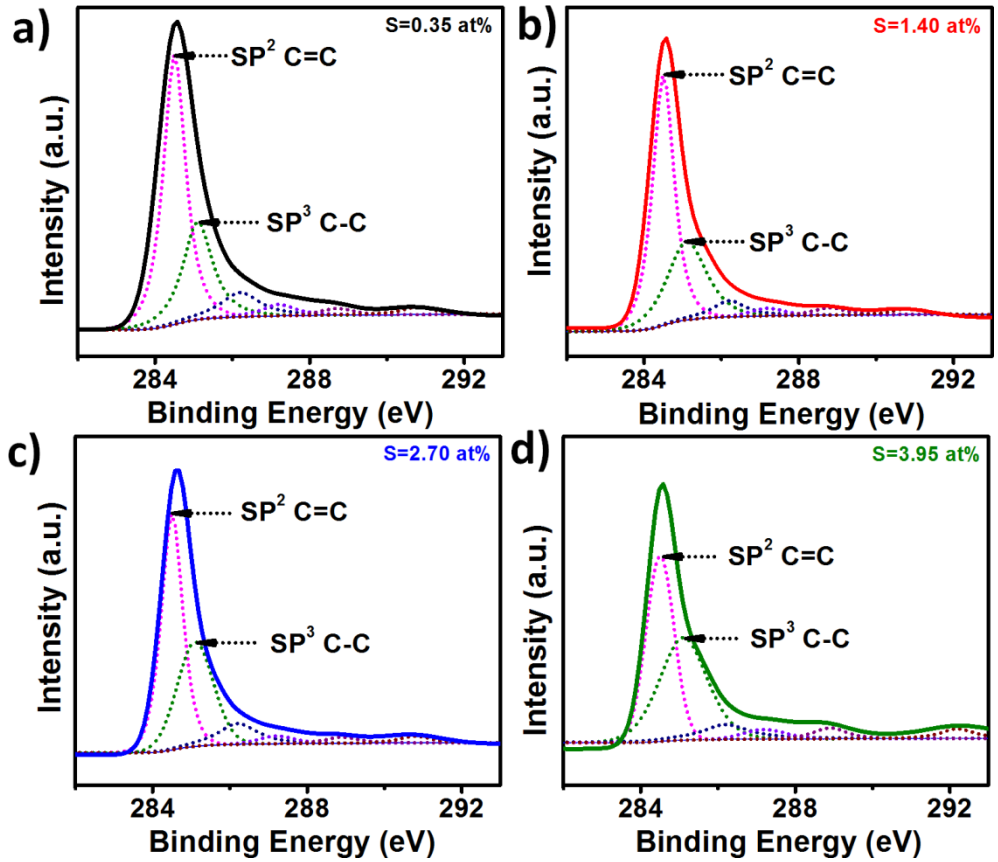

Figure 6-2 XPS high resolution C1s spectra for SG materials a) SG-1, b) SG-2, c) SG-3 and d) SG-4**.**

The structure of the different SG supports was analyzed by XRD, with results shown in **Figure 6-3a**. The average interlayer spacing corresponding to the (002) peak at ca. 25° were 3.49, 3.47, 3.41 and 3.38 Å for SG-1, SG-2, SG-3 and SG-4, respectively. It is clear that the d spacing values of various SG supports decrease with an increase in sulfur content. This is likely due to the fact that more oxygen functional species are removed with increasing amounts of sulfur [222]. In particular, the oxygen content of SG was found to decrease from 12.9 at% for SG-1 to 2.3 at% for SG-4 **(Table A-2 in the**

appendix). In addition, the thickness of the graphene platelets can be determined by calculating the crystallite sizes (L_c) in the (002) direction using the Scherrer equation:

$$L_c = A\lambda/B\cos\theta \quad (6\text{-}1)$$

where A is the shape factor (~0.9), λ is the X-ray wavelength, θ is the Bragg angle and B is the full width at half maximum (FWHM) of the (002) peak in radians. The crystallite size increases with an increase in sulfur concentration, with thicknesses of 18.1, 20.0, 35.1 and 43.8 Å for SG-1, SG-2, SG-3 and SG-4, respectively. The number of graphene layers can then be estimated [223, 224] by correlating L_c with the corresponding d spacing values to be 5.4, 6.2, 10.3 and 13.1, respectively. The d spacing and the number of layers were increased significantly for SG-3 and SG-4, which indicate that a high loading of sulfur precursor may enhance the restacking of graphene layers. This likely occurs due to increased removal of oxygen species that was found concurrently with higher sulfur contents.

Raman spectroscopy was used as a quantitative measure to estimate the degree of disorder in SG with different sulfur concentrations and results are shown in **Figure 6-3b**. In the spectra, the ratio of the D band intensity to the G band intensity (I_D/I_G) were ca. 1.10, 1.23, 1.35 and 1.43 for SG-1, SG-2, SG-3 and SG-4, respectively. All of these values for SG materials were higher than that of un-doped G (I_D/I_G: 0.96). This shows that the sulfur atoms present in SG are in the form of defects. This is to be expected considering that XPS indicated sulfur atoms are present in thiophenic form, which is a five ring structure that disrupts the crystalline planes of graphene.

Figure 6-3c shows the UV-vis absorption spectra of G, SG-1, SG-2, SG-3, SG-4 with a peak centered at 268 nm. To determine the energy band gap (E_g), Tauc's equation was applied [225]:

$$\omega^2\varepsilon = (h\omega - E_g)^2 \quad (6\text{-}2)$$

where ε is the absorbance, ω is the angular frequency of light which is 2π/λ, h is the Planck constant and λ is the wavelength. On plotting $\varepsilon^{1/2}/\lambda$ versus $1/\lambda$ (**Figure 6-3d**), a straight line intersecting with the x-axis is $1/\lambda_g$ (λ_g is the gap wave length) [226-228]. The energy band gap was calculated based on $E_g = hc/\lambda_g$ to be 0.45, 0.54, 0.61, 0.72 and 0.84 eV for of G, SG-1, SG-2, SG-3 and SG-4 respectively. It should be noted that the band gap increases in the order of SG-4 > SG-3 > SG-2 > SG-1 > G, suggesting a decrease in intrinsic conductivity due to an increasing amount of sulfur in graphene. The trend observed is likely due to the lower graphitic character of the SG materials with increased sulfur concentrations, confirmed both by XPS and Raman spectroscopy. The intrinsic conductivity of G and various SGs was in fact measured using the 2-point probe method [208] and the results obtained from

the LPR technique are shown in **Figure A-22 in the appendix**. The following equation was applied to measure the intrinsic conductivity of the materials.

$$\sigma = L/RA \qquad (6\text{-}3)$$

where σ is the conductivity in S/cm, L is the thickness of the electrode in cm, R is the resistance in Ω and A is the cross-sectional area of electrode in cm^2. From the LPR technique applied, the resistance decreases in the order of GO > SG-4 > SG-3 > SG-2 > SG-1 > G. Therefore, the intrinsic conductivities determined for G, SG-1, SG-2, SG-3, SG-4 and GO were 16.5, 13.9, 10.6, 7.3, 1.6 and 1.4×10^{-4} S cm^{-1}, respectively, values that are within the range of previously reported results from the literature [229]. The trends clearly show that the electrical conductivity of SG decreases with an increasing sulfur content. Despite the fact that conductivity plays an important role in electrocatalysis, the best ORR performance was achieved for PtNW/SG-2 with a sulfur content of 1.40 at% (vide infra). This suggests that at this content, conductivity limitations do not present a significant issue.

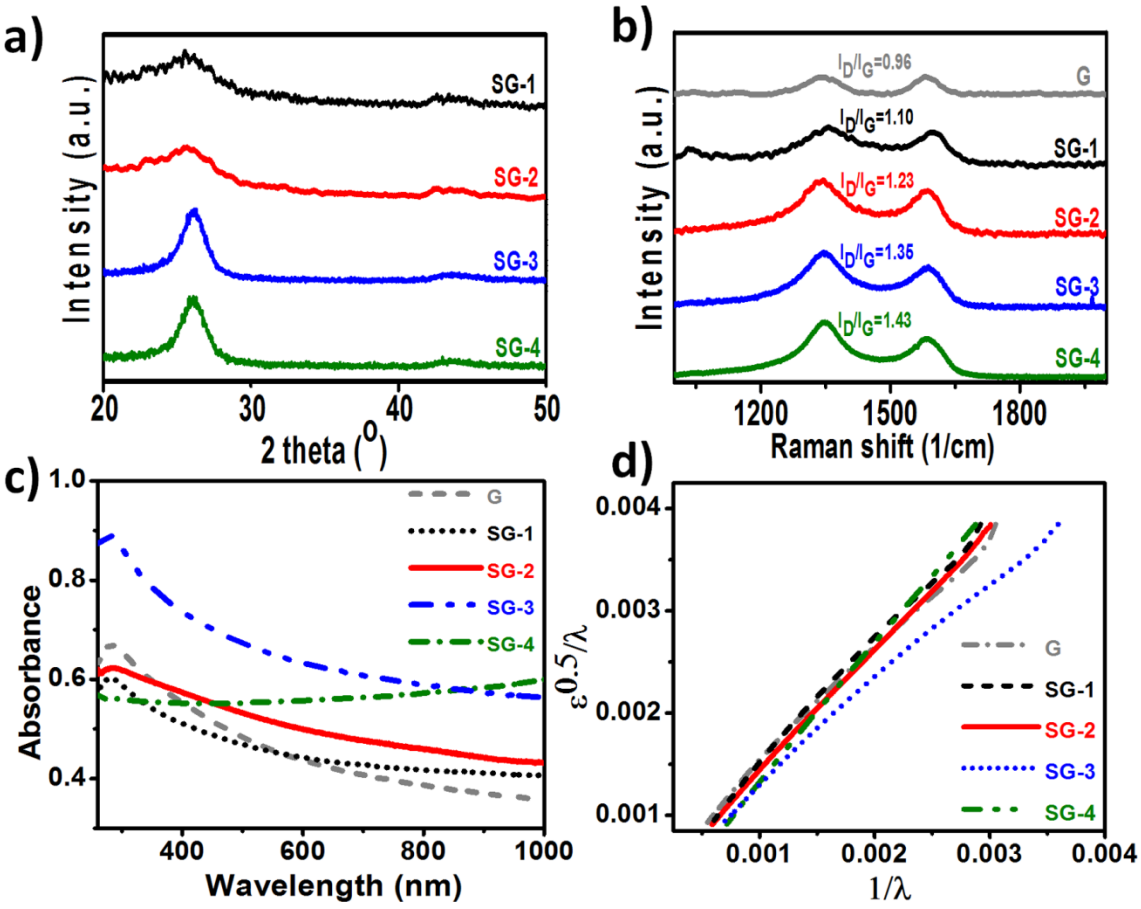

Figure 6-3 a) XRD for SG, b) Raman spectra of G and SG and c-d) UV absorption for G and SG.

6.3.2 Electrochemical characterization

Cyclic voltammetry (CV) was used to investigate the effect of sulfur concentration on the electrochemical properties of the PtNW/G and PtNW/SG. **Figure 6-4a** shows the steady state CVs of PtNW/G, PtNW/SG-1, PtNW/SG-2, PtNW/SG-3 and PtNW/SG-4 obtained in N_2-saturated 0.1 M $HClO_4$ solution. The typical hydrogen adsorption/desorption signature is observed in the 0.05 to 0.4 V vs RHE potential range. Electrochemical double layer capacitance is observed between 0.4 and 0.7 V vs RHE, and platinum oxidation/reduction occur in the range of 0.7 to 0.9 V vs RHE. ECSA values were determined based on the calculated charge for hydrogen adsorption/desorption of each voltamogram using the following equation [49, 230]:

$$ECSA = \mathbf{Q} / (0.21 * L) \quad (6\text{-}4)$$

where Q indicates the charge density for hydrogen adsorption (mC cm^{-2}) that can be calculated by integrating the hydrogen adsorption/desorption region and dividing by the potential scan rate, L is the mass loading of Pt on the electrode (mg cm^{-2}) and the factor 0.21 (mC cm^{-2}_{Pt}) is due to the charge required to reduce a monolayer of protons on Pt. The ECSA values determined for PtNW/G, PtNW/SG-1, PtNW/SG-2, PtNW/SG-3 and PtNW/SG-4 are 24.2, 26.3, 28.5, 19.7 and 18.8 $m^2\ g_{Pt}^{-1}$, respectively. **Figure 6-4b** shows the CV curves obtained for various catalyst materials subjected to 1000 potential cycles between 0.05 and 1.5 V vs RHE. After ADT, the ECSA values calculated for PtNW/G, PtNW/SG-1, PtNW/SG-2, PtNW/SG-3 and PtNW/SG-4 are 10.8, 14.1, 21.4, 10.8 and 9.5 $m^2\ g_{Pt}^{-1}$, respectively. However, ECSA values obtained for Pt/C before and after ADT are 54.5 and 13.1 $m^2\ g_{Pt}^{-1}$, respectively (**Figure A-23 in the appendix**). The reduced ECSA of the nanowire catalysts in comparison to Pt/C is expected due to the thicker diameter and anisotropic structure that results in a lower degree of Pt-atom exposure [165, 166]. A comparison of the ECSA values of various catalysts has been shown in **Figure 6-4c**. Normalized ECSA values obtained initially and after each 250 subsequent cycles are shown in **Figure 6-4d**. It can be seen that the ECSA retention of PtNW/SG-2 is higher, retaining 75% of its initial surface area whereas the retention was 45, 53, 55, 51 and 24% for PtNW/G, PtNWSG-1, PtNW/SG-3, PtNW/SG-4 and Pt/C, respectively. The least ECSA retention exhibited by Pt/C in comparison to the nanowire catalysts can be explained by the TEM images and the particle size distribution shown in **Figure A-24 in the appendix**. It can be seen that the nanoparticles are significantly affected and the average size is increased from 2.15 to 7.5 nm. These results indicate that PtNW/SG-2 has the highest electrochemical stability in terms of ECSA retention during potential cycling. Additionally, it was found that regardless of sulfur content, SG

supported PtNWs demonstrated increased electrochemical stability in comparison to PtNW/G, reasserting the beneficial impact of sulfur species in the catalyst supports.

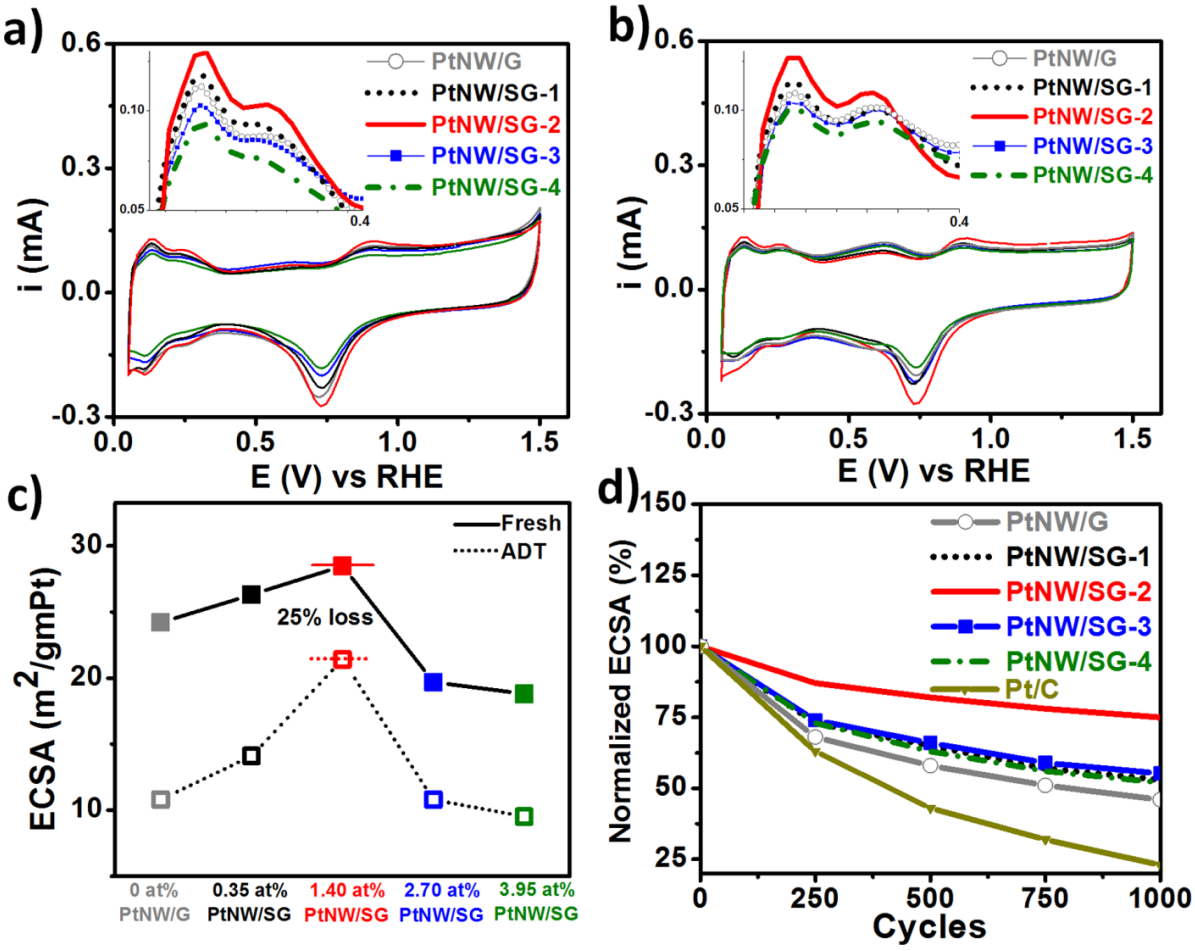

Figure 6-4 CV curves a) initially and b) after ADT. c) Comparison of ECSA for the various catalysts. d) Effect of cycle number on normalized ECSA of the various catalysts.

ORR measurements were carried out in O_2-saturated 0.1 M $HClO_4$ solution using a GC rotating disc electrode at room temperature in order to investigate the influence of sulfur on ORR activity of different nanowire catalysts. The polarization curves shown in **Figure 6-5 (a-b)** display the diffusing-limiting current region from ca. 0.05 to 0.65 V vs RHE and mixed kinetic-diffusion control region between ca. 0.7 and 1.05 V vs RHE. All polarization plots were collected using identical platinum loadings on the electrode. It is clear that the half-wave potential of PtNW/SG-2 before and after ADT was higher than the other catalysts, indicating in addition to improved electrochemical durability, PtNW/SG-2 also provides improved ORR activity. After ADT, the half wave potential loss was only

15 mV for PtNW/SG-2. On the other hand, the losses in half-wave potential were 48, 40, 38, 45 and 56 mV for PtNW/G, PtNW/SG-1, PtNW/SG-3, PtNW/SG-4 and Pt/C, respectively (**Figure 6-5c**). To compare the mass activity of the different catalysts, kinetic current densities were calculated from the polarization curves by correcting for mass transport and then normalizing with respect to platinum loading [154, 176]. The following Koutecky-Levich equation was applied to calculate the kinetic current density, j_k:

$$1/j = 1/j_k + 1/j_d \quad (6\text{-}5)$$

where j is the measured current density, j_k is the kinetic current density and j_d is the diffusion-limiting current density. From **Figure 6-5d**, it can be seen that the initial mass activity calculated at 0.9 V vs RHE for PtNW/SG-2 was 182 mA mg_{Pt}^{-1}, demonstrating excellent ORR activity in comparison with PtNW/G (125 mA mg_{Pt}^{-1}), PtNW/SG-1 (142 mA mg_{Pt}^{-1}), PtNW/SG-3 (108 mA mg_{Pt}^{-1}), PtNW/SG-4 (101 mA mg_{Pt}^{-1}) and Pt/C (127 mA mg_{Pt}^{-1}). After the ADT, PtNW/SG-2 also demonstrated superior ORR stability, providing a mass activity of 131 mA mg_{Pt}^{-1} at 0.9 V vs. RHE that represents 72% of its initial activity. Conversely, the mass activity retention after ADT for PtNW/G, PtNW/SG-1, PtNW/SG-3, PtNW/SG-4 and Pt/C were 43, 45, 48, 46 and 28%, respectively. Moreover, the specific activity determined at 0.9 V vs RHE shown in **Figure A-25 in the appendix** for PtNW/SG-2 was higher (662 μA cm^{-2}_{Pt}) in comparison to PtNW/G (530 μA cm^{-2}_{Pt}), PtNW/SG-1 (556 μA cm^{-2}_{Pt}), PtNW/SG-3 (567 μA cm^{-2}_{Pt}), PtNW/SG-4 (542 μA cm^{-2}_{Pt}) and Pt/C (244 μA cm^{-2}_{Pt}), respectively. These results clearly indicate that SG-2 can effectively increase the activity of PtNW/SG-2. Notably, the Pt mass and specific activity obtained by PtNW/SG-2 was higher than some other results reported in the literature. These include carbon supported multi-armed star-like platinum nanowires that shows a mass activity of 135 mA mg_{Pt}^{-1} and a specific activity of 611 μA cm^{-2}_{Pt}, ultrathin Pt multiple-twinned nanowire networks that shows a mass activity of 144 mA mg_{Pt}^{-1} and a specific activity of 139 μA cm^{-2}_{Pt}, platinum nanocrystal supported by reduced graphene oxide that shows a mass activity of 109 mA mg_{Pt}^{-1} and a specific activity of 212 μA cm^{-2}_{Pt}, and Pt-Pd bimetallic nanodendrites that shows a mass activity of 204 mA mg_{Pt}^{-1} and a specific activity of 422 μA cm^{-2}_{Pt} [166, 175, 176, 231]. It has been well established that ORR activity of Pt nanostructures increases accordingly with an appropriate decrease in the binding energy of oxygenated species to the Pt surface [170, 171, 173, 232]. This is because low coordination surface Pt atoms of nanoparticle structures that are prone to block the active sites by oxygenated species, i.e. OH_{ads} inducing higher binding energy than the optimal values (~ 0.2 eV) [171, 233]. However, Pt nanowires possess fewer undesirable low coordination sites that results in their improved catalytic activity. Additionally, we believe that sulfur with 1.40 at% is an ideal amount in

SG to achieve uniform Pt nanowire morphology and geometry leading to a higher ECSA, activity and stability of PtNW/SG-2. Based on measurement of over 50 individual nanowires, the nanowires supported by SG-2 are smaller than the nanowires supported by G and SG-1 and notably, the growth of nanowires was significantly interrupted onto SG-3 and SG-4. The presence of a high amount of sulfur in SG-3 and SG-4 might provide too many anchoring sites where nanoparticles nucleate and begin to elongate, leaving insufficient platinum precursors in solution to continue the formation of well-defined, smooth nanowires.

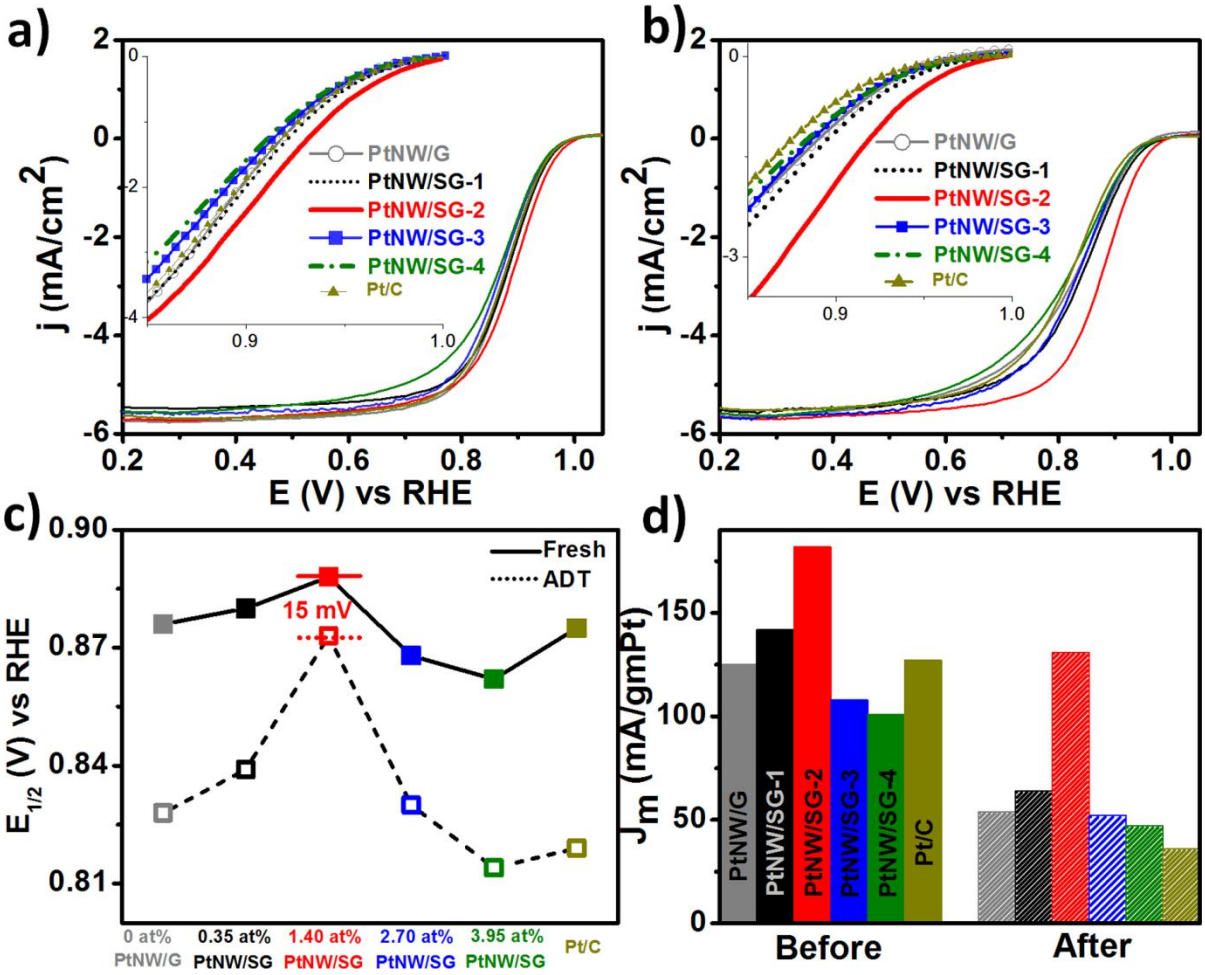

Figure 6-5 ORR curves a) initially and b) after ADT. Comparison of the c) $E_{1/2}$ and d) Pt mass activities obtained for the various catalysts.

Mass transport corrected Tafel plots at different temperatures for PtNW/G and PtNW/SG catalysts are shown in **Figure 6-6 (a-d)**. At any temperature, the low and the high Tafel slopes can be determined for each catalyst and correspond to the potential regime where oxygen reduction proceeds on oxide-

covered Pt surface (Temkin conditions) and on oxide-free Pt surface (Langmuir conditions), respectively[209]. The low and high Tafel slopes from the $\log J_k$-V plots calculated at different temperatures for PtNW/G, PtNW/SG-1, PtNW/SG-2 and PtNW/SG-3 catalysts remain essentially constant (low Tafel slope: 60 ± 5 mV dec^{-1} and high Tafel slope: 120 ± 5 mV dec^{-1}) [234]. The exchange current density (j_o) corresponding to each Tafel slope was calculated by extrapolating the potential to the temperature corrected reversible potential (E_r), with the determined values listed in **Table A-3 in the appendix** Note that, the dependence of E_r on temperature was evaluated using the following equations [209]:

$$\Delta G^0 = -70650 - 8.0T \ln T + 92.84\,T \quad (6\text{-}6)$$

$$E_r = -\Delta G^0/nF \quad (6\text{-}7)$$

where ΔG^0 is the free energy for O_2-H_2 reaction producing liquid water, n is the number of electrons transferred to produce one mole of water, n=2 and F is the Faraday's constant (96485 C mol^{-1}).

The temperature dependence exchange current densities in both Tafel regimes for each catalyst are plotted in **Figure 6-6e**, and the activation energy for oxygen reduction of the catalyst was determined using the following Arrhenius equation.

$$E_a = -2.303R\,[d\log j_k/d(1/T)] \quad (6\text{-}8)$$

where E_a is the activation energy in J mol^{-1}, R is the gas constant (8.314 J mol^{-1} K^{-1} and T is the temperature in K. **Figure 6-6f** shows the apparent activation energy diagram of various catalysts in both low and high current density regimes. The activation energy calculated for PtNW/G, PtNW/SG-1, PtNW/SG-2 and PtNW/SG-3 were 18.7, 17.3, 14.4, 22.1 kcal mol^{-1} in the low current density regime (at 0.95 V) and 7.31, 6.40, 5.94 and 8.23 kcal mol^{-1} in the high current density regime (at 0.85 V), respectively. These values are in close agreement with values reported in the literature for both the high current density regime [209] and the low current density regime [85, 235]. It should be noted that PtNW/SG-4 was omitted from temperature dependent studies owing to its relatively poor ORR performance in comparison to other catalysts. Interestingly, PtNW/SG-2 possesses significantly higher exchange current density and lower activation energy on both oxide-covered and oxide-free surfaces in comparison to other catalysts. This again demonstrates the high electrocatalytic activity of this catalyst towards the ORR. It has been shown experimentally and theoretically that the first electron transfer ($O_2 + H^+ + e^- \rightarrow O_2H_{ads}$) of the ORR is the rate determining step if the difference between the activation energies on oxide-covered and oxide-free Pt surface is 4 kcal mol^{-1} [236]. However, in our studies, the difference between the activation energies of each catalyst was above 8 kcal mol^{-1}, which might indicate the existence of a chemical step [172] following the first electron-

transfer on the Pt surface [210, 236]. Therefore, the following reaction mechanism can be considered to elucidate the catalytic properties of various catalyst materials:

$2Pt\ldots O_2 \leftrightarrow Pt_2O_{2ads}$ (6-9)

$Pt_2O_{2ads}+H^+ + e^- \leftrightarrow Pt_2O_2H_{ads}$ (first electron-transfer step) (6-10)

$Pt_2O_2H_{ads} \rightarrow Pt\text{-}O+Pt\text{-}OH$ (chemical step) (6-11)

$Pt\text{-}O+Pt\text{-}OH + H^+ + e^- \rightarrow Pt\text{-}OH+Pt\text{-}OH$ (6-12)

$Pt\text{-}OH+Pt\text{-}OH+2H^+ + 2e^- \rightarrow 2Pt+2H_2O$ (6-13)

While considering the reaction steps mentioned above, the fractional coverage of reaction intermediates in the rate determining step can be significantly reduced for PtNW/SG-2 due to its high exchange current density and low activation energy compare to other catalysts. This can be attributed to a weak binding between oxygenated species and the Pt surface atoms which is beneficial for enhancing ORR kinetics. Therefore, it is obvious that the amount of sulfur in graphene is a crucial parameter to tune the electrokinetics of nanowire catalysts. It is now demonstrated that 1.40 at% sulfur in graphene provides improved physico-chemical properties favorable to enhance Pt electrocatalytic activity and stability. To illustrate, based on our DFT analysis on various SG materials discussed in the next section it can be established that for SG with 0.35 at% sulfur (SG-1), the DOS of SG is almost equal to that of pristine graphene, showing a Dirac point which has no band gap and energy of states supposes to display a similar ORR activity in comparison with that on pure graphene. Interestingly, the performance observed was similar for both G and SG-1 supported PtNWs. On the other hand, at higher sulfur contents, the physico-chemical properties of SG-3 (2.70 at% sulfur) and SG-4 (3.95 at% sulfur) were adversely affected leading to an interruption on the growth of well-defined PtNWs that can potentially result in the reduced ORR activity and stability.

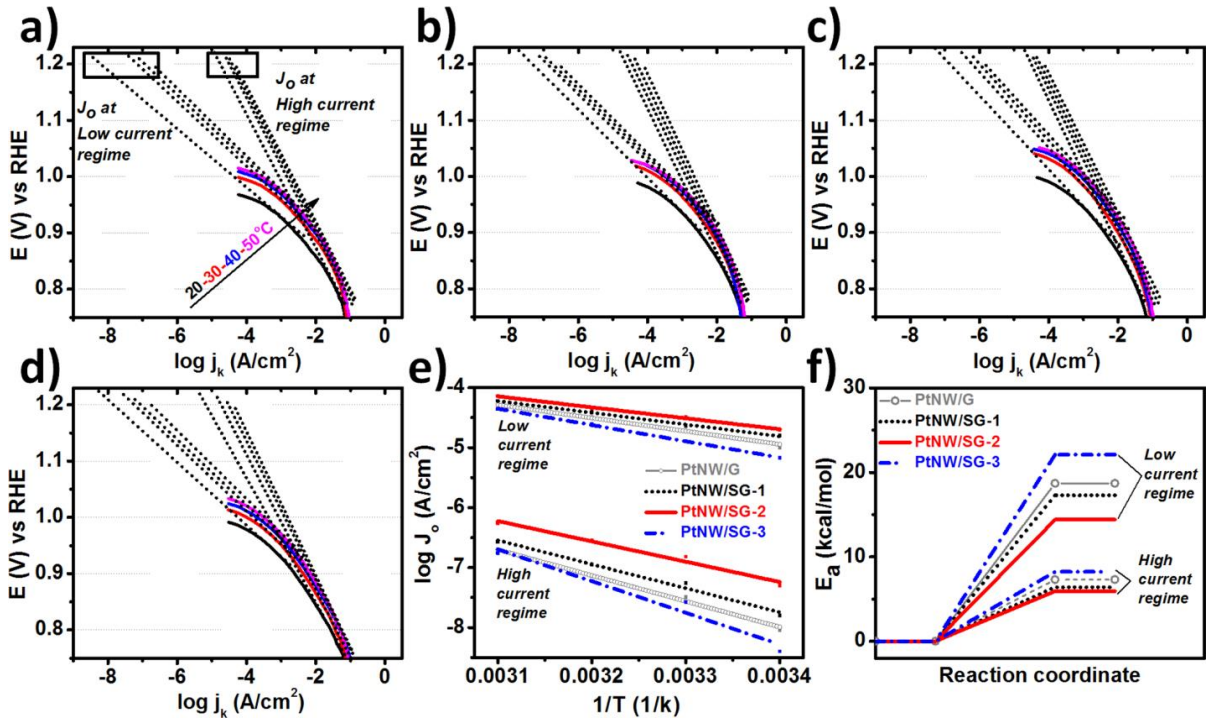

Figure 6-6 a-d) Mass transport-corrected Tafel plots for oxygen reduction as a function of temperature, e) Arrhenius plot and f) Exchange current density.

6.3.3 Computational investigations

It was well established that the support materials can significantly enhance the catalytic activity and stability of metallic nanoparticles such as Pt and Pd [112, 117, 118, 124, 237-244]. In the graphene framework, the heteroatoms change the electronic structure of graphene, providing sufficient anchoring sites for metal nanoparticles deposition leading to an improved catalytic activity [112, 117, 240-242, 244-246]. Previously, we reported that both N and S-doped graphene (NG and SG) significantly improve the activity and stability of Pt nanoparticles due to a downward shift in d-band center, reduced binding energy of oxygen intermediates, and increased cohesive energy and dissolution potentials [245, 246]. Therefore, the electronic structure of supporting materials (e.g., density of states, DOS) is an important parameter that help us to understand the interactions occurring between the support and nanoparticles, and also to investigate the alteration of intrinsic properties of the nanoparticles [120, 240, 242-244]. Owing to the advantages of sulfur doping into the graphene matrix and its beneficial impact on Pt nanoparticles, we were then motivated to elucidate the electronic structures of SG as a function of sulfur concentration. Note that DFT analysis was conducted on SG to see how the DOS changes with

a change in sulfur content. While this will have an effect on the electronic properties of the PtNWs, owing to the complex nature of this systems and intense computational facilities that would be required to investigate this, these investigations are not included. **Figure 6-7** demonstrates detailed DFT analysis on G and SG with different sulfur contents ranging from 0.35 to 3.23 at%. The calculated spin resolved density of states (DOS) of the valence electrons were calculated in G and SGs. As reported previously [20,21], graphene has a specific unique nature of semi-metal which appears conical shape near the Fermi energy in DOS at the point where no band gap and DOS exists with the electrical conductivity governed by Dirac's equation [123] (**Figure 6-7a**). Interestingly, SG with 0.35 at% sulfur displays no band gap and DOS similar to the pristine graphene (**Figure 6-7b**). However, further increasing the sulfur content of the graphene matrix, the disruption of the sp2 carbon hybridization occurs, resulting in a change of the Fermi level and DOS of graphene (**Figure 6-7c-e**). The total DOS for thiophene like SG reveals that no energy of densities are generated at Fermi level in both of spin up and down states, showing a well-defined band gap of 0.158, 0.323 and 0.476 eV for 1.02, 2.04 and 3.23 at% sulfur in graphene, respectively. The trend in band gap with increasing amount of sulfur in the graphene framework clearly indicates the lowering of electrical conductivity of SG materials which was also confirmed by the experimental investigations.

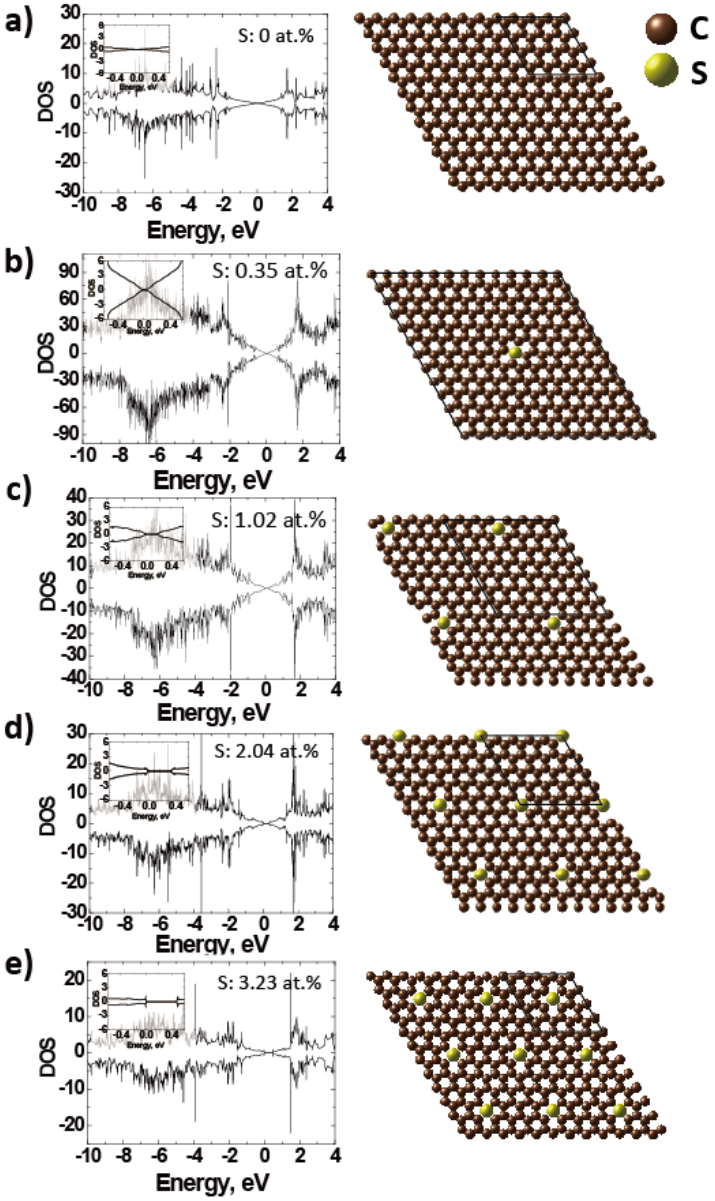

Figure 6-7 a-e) Calculated spin resolved density of states and their designed models for G and SGs.

6.4 Conclusions

Through experimental and computational investigations, we provide detail fundamental insight for designing PtNW/SGs as ORR catalysts in acidic electrolyte. A series of SG materials with varying sulfur contents ranging from 0.35 to 3.95 at% was prepared. We found that the amount of sulfur significantly affects the ORR kinetics of nanowire catalysts due to the influence of the sulfur dopants

present in SG. With increasing sulfur content, the number of graphene layers increased as determined by XRD. Furthermore, the ratio of sp^2 to sp^3 carbon decreases, indicating a less graphitic character of SG. Moreover, the results obtained from UV-Vis and LPR technique show that the band gap increases and the electrical conductivity decreases with an increase in the amount of sulfur in the graphene matrix. Both of these effects are consistent with the results obtained from DFT analysis. PtNW/SG-2 (1.40 at% sulfur) shows the best electrokinetic performance, with a mass activity of 182 mA mg_{Pt}^{-1} and a specific activity of 662 $\mu A cm^{-2}_{Pt}$ at 0.9 V vs. RHE. Moreover, PtNW/SG-2 shows a high exchange current density and low activation energy which leads to a weakened interaction between the nonreactive oxygenated species and Pt surface atoms that is beneficial for enhancing the kinetics of oxygen reduction.

Chapter 7 Platinum Nanowires on Sulfur-Doped CNT

The following section is based on our recent work by **Hoque, M. A.,** Hassan, M. F., Pritzker, M., Choi, J-. Y., Banham, D., Ye S., Knight S., and Chen, Z.
Angewandte Chemie International Edition (To be submitted)

"Web-like 3D architecture of platinum nanowires and sulfur-doped CNT with superior electrocatalytic performance"

Author contributions: H.M.A conducted the material preparations, characterizations and electrochemical tests. H.M.A wrote the manuscript. C.Z. and P.M co-supervised the project. All authors reviewed the manuscript.

7.1 Introduction

Long term durability of the platinum catalyst at the cathode is one of the critical challenges that have limited the widespread application of proton exchange membrane fuel cells (PEMFCs).[247] The loss of the electrochemical surface area of Pt during fuel cell operation due to corrosion of carbon supports and Pt dissolution/aggregation/Oswald ripening are mainly responsible for the rapid drop in the power output of fuel cells.[248] Up to now, platinum nanoparticles (2-5 nm) dispersed on carbon black supports (Pt/C) have been the most widely used catalysts in cathodes.[3] However, such nanoparticles undergo severe Oswald ripening and/or grain growth due to their high surface energy and zero-dimensional (0D) nanostructured characteristics.[166, 249, 250] In addition, carbon black undergoes electrochemical corrosion at low potentials that causes Pt nanoparticle migration, agglomeration and detachment from the catalyst structure.[165]

The control of Pt nanostructures is one of the effective strategies to improve the durability of Pt-based catalysts against the loss of ECSA.[152, 154, 249] For example, one-dimensional (1D) Pt nanostructures such as nanowires possess unique structural characteristics such as high stability and preferential exposure of highly active crystal facets and easy electron transfer compared to their 0D counterparts.[250, 251] The structural anisotropy of nanowires can slow down the ripening process and impede dissolution/aggregation, thereby improving catalytic durability and/or activity.[65] However, Pt nanowire catalysts grown onto stable supports such as carbon nanospheres (CNSs), carbon nanotubes (CNTs) and graphene have been shown to have significantly enhanced durability.[155, 156, 198] Among these support materials, CNTs possess outstanding properties such as high surface area, high

electrical conductivity, high tensile strength coupled with excellent mass transport ability.[252] It has been reported that doping CNTs with heteroatoms is an effective strategy to tune their intrinsic properties and improve electrocatalyst activity and durability.[49, 253] We previously demonstrated that the doping of graphene with sulfur (SG) is a very promising support material for Pt nanostructures that significantly improves stability compared to the state-of-the-art Pt/C.[160, 198] However, to our knowledge, the use of CNTs doped with sulfur (S-CNT) as Pt supports has not been reported in the literature. We have successfully synthesized S-CNT to support Pt nanowire electrocatalysts for the ORR and show that the newly developed materials will have impact for a wide range of applications.

Herein, we report an advanced and robust 3D electrocatalyst to address both the activity and durability problems associated with using 1D S-CNT-supported Pt nanowires (PtNW/S-CNT). We provide details concerning the structure, properties and characteristics of S-CNT. We optimize and investigate the role of precursor materials on the formation of Pt nanowires on S-CNT. Our electrochemical studies show that PtNW/S-CNT exhibits exceptional activity retention over 3000 accelerated durability test (ADT) cycles over the potential range from 0.05 to 1.5 V vs RHE. The unique 3D features of PtNW/S-CNT will have a significant role in the promotion of future cathode electrocatalysts for practical application.

7.2 Experimental

7.2.1 Functionalization of CNT (F-CNT)

In a typical experiment, 500 mg of commercially available MWCNTs (cheatubes.com) were added to 100 mL of a 3:1 mixture of concentrated H_2SO_4 and HNO_3.The mixture was treated in an ultrasonic bath for 20 min and refluxed while being constantly stirred at 60^{o}C for 1 h. The solid phase was removed by centrifugation and washed with de-ionized water until pH of the filtrate was 7. The filter cake was dried under vacuum at 80^{o}C for 24 h to obtain F-CNT.

7.2.2 Synthesis of S-doped CNT (S-CNT)

To synthesize S-CNT, 100 mg of functionalized CNT (F-CNT) and 50 mg of phenyl disulfide (PDS) were ultrasonically dispersed in 5 mL acetone for 1 h. The residual was then evaporated to obtain a uniform solid mixture by maintaining it at 50°C on a hot plate. The solid mixture was then transferred into a small quartz tube which was then placed inside a larger quartz tube for annealing. The sample was not introduced inside the furnace until it reached a temperature of 1000^{o}C. Once the furnace

temperature was 1000^{o}C, the sample was placed at the center of the furnace for 30 minutes. Then, the sample was removed from the tube furnace and cooled to room temperature in ambient Ar. The S-CNT was washed with DDI water and acetone to remove any organic impurities and dried overnight at 80°C in a vacuum oven.

7.2.3 Synthesis of S-doped CNT supported platinum nanowires (PtNW/S-CNT)

The synthesis of PtNW/S-CNT was accomplished by a modification of our previously published method of synthesis.[198] In a typical synthesis, 15 mL ethylene glycol (EG) and 15 mL *N*,*N*-dimethyl formaide (DMF), 1.5 gm KOH and 26.5 mg $H_2PtCl_6.6H_2O$ (10 mg Pt) were mixed together and stirred for 1 h to obtain a homogeneous solution. Then, 10 mg of S-CNT were added and stirred for 23 h. The final solution was transferred to a 50 mL teflon-lined autoclave for heating at 170°C for 8 h. The black product was finally collected and washed several times with ethanol and DDI water before drying in a vacuum oven at 80°C. Using this method, a platinum loading of 50% was achieved. The same procedure was applied to synthesize platinum nanowires on F-CNT (PtNW/F-CNT).

7.2.4 Materials characterization

The samples were characterized using scanning electron microscopy (SEM, LEO FESEM 1530), transmission electron microscopy (TEM, JEOL 2010F), Raman spectroscopy (SENTERRA 314) and X-ray photoelectron spectroscopy (XPS). Energy dispersive X-ray spectroscopy (EDX) and electron energy loss spectroscopy (EELS) were used in conjunction with TEM to map the elemental analysis over the sample surfaces.

7.2.5 Electrochemical characterization

For electrochemical testing, 2 mg of catalyst materials were dispersed in 2 mL of 1-propanol containing 10 μL (5 wt.%) Nafion solution by sonication for at least 1 h. The loading of catalyst materials onto glassy carbon electrode (5 nm diameter) was controlled to be 22 μg cm^{-2}. Cyclic voltammetry (CV) scans between 0.05 and 1.5 V RHE at a rate of 50 mV s^{-1} were conducted in a N_2-saturated 0.1 M $HClO_4$. Polarization curves were obtained by CV cycling between 0.05 and 1.2 V RHE at a scan rate of 5 mV s^{-1} in O_2-saturated 0.1M $HClO_4$. The positive-going scans during these cycles were used to evaluate the electrocatalysis toward the ORR. All testing was conducted at room temperature and the internal resistance (IR) drop was compensated to account for the effect of electrolyte resistance on potential measurements.

7.3 Results and Discussion

Figure 7-1 illustrates the flash heat treatment (FHT) process of as-prepared S-CNT and solvothermal synthesis of Pt nanowires on S-CNT. More details on the experimental procedure is provided in the supporting information. Briefly, the FHT process involves mixing F-CNT and phenyl disulfide (PDS) and heating the solid mixture at high temperature (1000°C). At this temperature, FDS decomposes to form carbonaceous gases and sulfur-free radicals, leading to the incorporation of sulfur atoms in the carbon framework of F-CNT. To grow and support the Pt nanowires onto S-CNT, we followed a simple solvothermal procedure without surfactant which is harmful to catalytic activity.

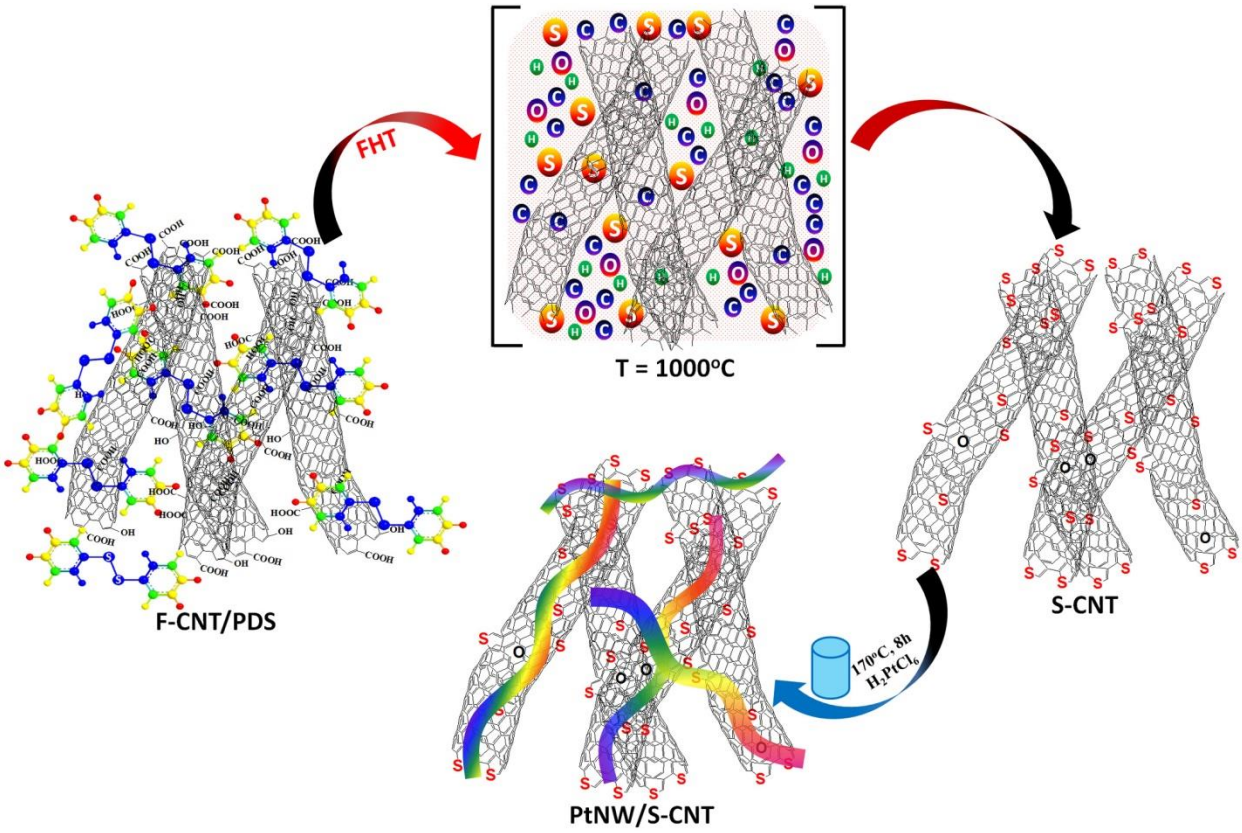

Figure 7-1 A schematic showing the simple process of synthesizing S-CNT and PtNW/S-CNT.

Figure 7-2a presents TEM images of F-CNT collected at low magnification. F-CNTs have diameters of 25 ± 8 nm and can be as long as several microns. An energy dispersive spectroscopy (EDS) elemental map of carbon and oxygen in F-CNT **(Figure 7-2b)** reveals that oxygen functional groups have been incorporated into the CNTs by contact with a HNO_3/H_2SO_4 mixture. High resolution TEM (HRTEM) was used to count the number of walls in F-CNT, measure the inner and outer diameters,

investigate structural integrity and identify structural changes (e.g., sidewall damage) caused by surface modification.[254] The F-CNT in **Figure7-2c** has a 6.2 nm inner diameter, 14.7 nm outer diameter and consists of approximately 20 layers. The HRTEM image of S-CNT in **Figure 7-2d** clearly indicates that the incorporation of S species by FHT does not alter the structural integrity of F-CNT. EDS mapping of carbon and sulfur in S-CNT **(Figure 7-2e)** shows that sulfur species are homogeneously distributed over the carbon network in the F-CNT. Used in conjunction with TEM, EELS can generate sulfur elemental maps of S-CNT in F-CNT. As observed in **Figure 7-2f**, sulfur atoms are clearly incorporated into the carbon matrix.

Raman spectroscopy was used to give a quantitative measure of the defect density in the CNT materials. The spectra in **Figure 7-2g** show that the ratios of D-band intensity to G-band intensity (ID/IG) are 0.68, 0.82 and 1.05 in CNT, F-CNT and S-CNT, respectively. This result indicates that the sulfur atoms are present in S-CNT as defects replacing carbon atoms via the reaction between oxygen-containing groups in F-CNT and PDS. Using XPS, the identity and concentration of the surface species of F-CNT and S-CNT was confirmed. **Figure 7-2h** displays the full range spectra of F-CNT and S-CNT, while their corresponding surface atomic concentrations are provided in **Table A-4 in the appendix**. Analysis of the S2p sulfur signal centered at 161.1 eV for S-CNT reveals a surface concentration of 1.02 at%. This indicates the effectiveness of applying the FHT on a mixture of F-CNT and PDS to incorporate sulfur dopants into the final F-CNT structure. **Figure 7-2i** presents high resolution XPS scan of the S2p region deconvoluted into two major peaks located at 163.93 and 165.10 eV and four minor peaks located at energies above165.92 eV. The two major peaks appear to result from the S2p spin-orbit doublet ($S2p_{1/2}$ and $S2p_{3/2}$, respectively) that can be attributed to sulfur directly bonded to carbon atoms in the form of C-S-C.[19] We speculate that these C-S-C species exist in the thiophene form, as supported by previously reported investigations and our formation energy calculations.[160] Furthermore, the pentagonal structured thiophene species reside on the edge plane and defect sites of S-CNT and most likely give rise to the appearance of the D band in the Raman spectra. The four minor peaks observed in the spectra can be assigned to carbon bonded SO_x species.[19]

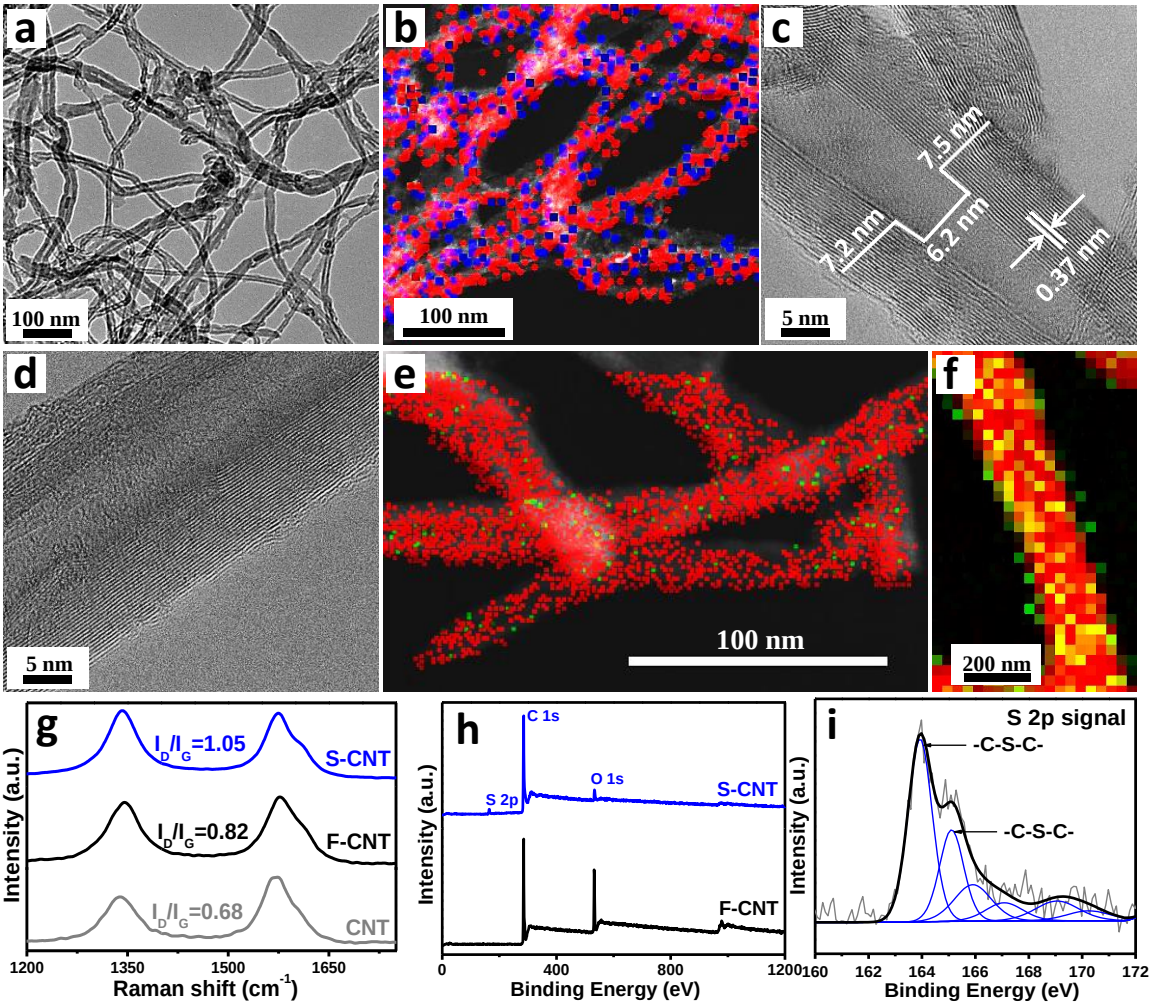

Figure 7-2 a-c) TEM and EDX on F-CNT, d-f) TEM and EELS on S-CNT, g) Raman and h-i) XPS.

Figures 7-3a and b show representative scanning electron microscope (SEM) and transmission electron microscope (TEM) images that reveal the interconnected 3D architecture of PtNW/S-CNT. The nanowires have a range of diameters from 4 to 28 nm, while their lengths exceed 1 μm. Our previous investigation on the growth of Pt nanowires on the surface of SG shows that the nanowires are composed of numerous Pt nanoparticles linked together.[198] The nanowires supported by S-CNT also appear to be composed of nanosized Pt particles joined together, with a crystallographic orientation along the <111> direction, a distance of approximately 0.23 nm between (111) planes, as shown by the HRTEM image in **Figure 7-3c**. Apart from our previous studies, we modified the

synthesis and investigated the role of precursor materials in the formation of Pt nanowires in the presence of S-CNT (**Figure A-26 to A-31 in the appendix**). We found that an ideal condition to obtain the desired nanowire morphology can be achieved using 15 mL ethylene glycol, 15 mL DMF, 1.5 g KOH, 10 mg Pt and 10 mg S-CNT during synthesis. This leads to growth of small-diameter Pt nanowires primarily in the range of 4-12 nm onto 1D nanostructured carbon supports such as S-CNT. However, the nanowires grown on undoped F-CNT tend to have larger diameters mostly in the range of 8-20 nm **(see Figure 7-3d and Figure A-32 in the appendix)**. Sulfur in F-CNT appears to play a key role in anchoring the direction of nanowire formation, binding the nanowires very tightly and thereby avoiding their agglomeration/detachment. BET analysis **(Figure 7-3e)** shows that PtNW/S-CNT possesses a specific surface area of 125 m^2g^{-1} which is higher than that of PtNW/F-CNT (101 m^2g^{-1}). The pore size distribution clearly shows the presence of multiple porosities (micro/meso/macro) in the catalyst materials. It is interesting to note that PtNW/S-CNT is highly porous (total pore volume: 0.6 cm^3g^{-1}) and contains predominantly macropores (65%), whereas only 45% of the overall pore volume in PtNW/F-CNT (total pore volume: 0.38 cm^3g^{-1}) involves macropores. It has been reported that ORR performance can be improved by the presence of macropores that shorten the diffusion length of reactive molecules.[255] Therefore, it is expected that the presence of numerous large pores should promote the efficient electrocatalysis by PtNW/S-CNT. The Pt4f spectra of PtNW/S-CNT and PtNW/F-CNT in **Figure 7-3f-top** show that both materials exhibit the characteristic doublet of zero-valence Pt with the Pt4f7/2 and Pt4f5/2 located at 71.56 and 75.80 eV in PtNW/S-CNT and 71.25 and 74.58 eV in PtNW/F-CNT. It is important to note that the peak position in PtNW/S-CNT is shifted by 0.31 eV in the positive direction in comparison to that observed for PtNW/F-CNT, providing a clear indication of an enhanced interaction between Pt and S-CNT. Moreover, a noticeable negative peak shift in the S2p peak for PtNW/S-CNT by 0.33 eV relative to that observed in S-CNT is observed **(Figure 7-3f-bottom)**, indicating a transfer of electrons from S-CNT to Pt.

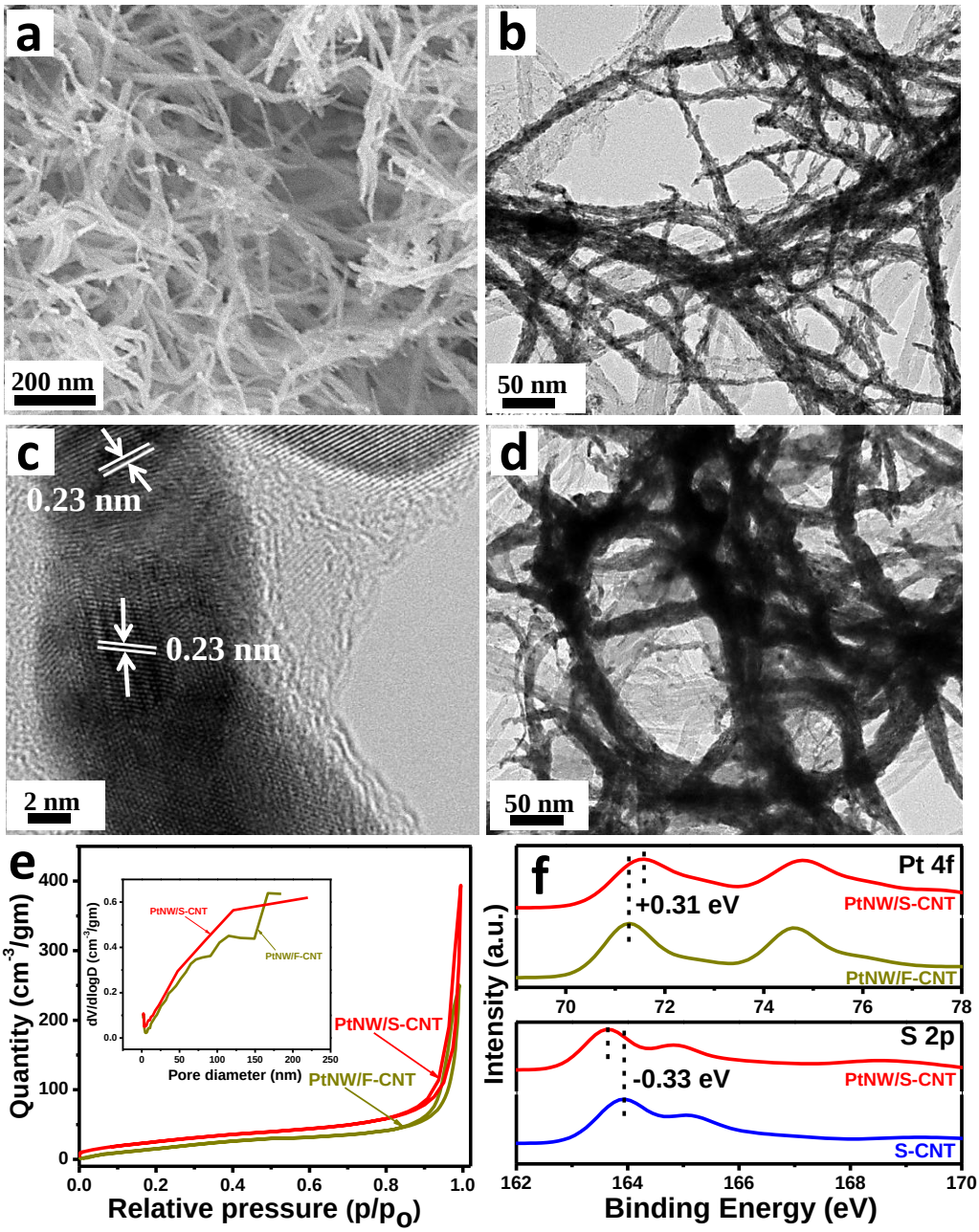

Figure 7-3 a-c) Micrographs of PtNW/S-CNT, d) TEM image of PtNW/F-CNT, e) BET and f) XPS.

Figure 7-4a shows cyclic voltammograms (CV) of PtNW/S-CNT immersed in N_2-saturated $HClO_4$ (0.1M) obtained at a sweep rate of 50 mV s^{-1}. CV curves before and after cycling for up to 3000 cycles between 0.05 and 1.5 V RHE were collected to evaluate the long-term electrochemical stability

of the catalysts. The electrochemical active surface area (ECSA) was estimated by integrating the hydrogen adsorption/desorption region between 0 and 0.4 V RHE and assuming Q_{ref} = 0.21 mC cm^{-2} for the adsorption of a hydrogen monolayer.[49] The ECSA values obtained for PtNW/S-CNT before and after ADT were measured to be 17.2 and 16.0 m^2g^{-1}, respectively. For comparison, the stabilities of PtNW/F-CNT and commercial Pt/C catalyst (TKK, 28.2% Pt loading) were also evaluated, as shown in **Figure A-33 in the appendix**. Under identical conditions, the ECSA values were found to be 15.7 and 9.7 m^2g^{-1}, respectively, for PtNW/F-CNT and 55.4 and 0.1 m^2g^{-1}, respectively for Pt/C. The reduced ECSA of PtNW/S-CNT and PtNW/F-CNT in comparison to Pt/C is to be expected due to the larger diameter and the structural anisotropy of the nanowires that lowers the degree of Pt atom exposure.[165, 166, 176] **Figure 7-4b** shows typical ORR polarization curves of the PtNW/S-CNT obtained at room temperature in O_2-saturated $HClO_4$ (0.1M) at a sweep rate of 5 mV s^{-1}. The electrochemical reduction reaches the mass transfer limit below 0.8 V RHE and a mixed kinetic-diffusion control region between 0.8 and 1.0 V RHE. The polarization curves in **Figure 7-4b** obtained before and after ADT shows only a 7 mV loss in the half-wave potential ($E_{1/2}$) for PtNW/S-CNT. At the same time, a loss of 54 mV in $E_{1/2}$ for PtNW/F-CNT and >400 mV loss for Pt/C was observed under identical conditions (see **Figure A-34 in the appendix**). The variation of the normalized ECSA of the catalysts with the number of ADT cycles is plotted in **Figure 7-4c**. After 3000 cycles, PtNW/S-CNT has lost only 7% of the initial ECSA, while PtNW/F-CNT and Pt/C lost 38% and >99% of their initial ECSA, respectively. Clearly, these ADT results demonstrate that PtNW/S-CNT has significantly higher stability after 3000 cycles.

The specific and mass activities are good indicators of the quality of an electrocatalyst. As shown in **Figure 7-4d (inset)**, PtNW/S-CNT achieved a specific activity of 1.61 mA cm^{-2}Pt, which is higher than that of PtNW/F-CNT (1.37 $mAcm^{-2}$Pt) and Pt/C (0.244 $mAcm^{-2}$Pt). A comparison of the Pt-based mass activities before and after ADT is also shown in **Figure 7-4d**. Prior to the ADT, PtNW/S-CNT showed an improved mass activity of 272 mA mg^{-1}Pt in comparison to PtNW/F-CNT (204 mA mg^{-1}Pt) and Pt/C (130 mA mg^{-1}Pt). After the ADT, PtNW/S-CNT was able to maintain a mass activity as high as 220 mA mg^{-1}Pt, which is 81% of the initial value. On the other hand, the mass activities of PtNW/F-CNT and Pt/C dropped to 67 and 0.2 mA mg^{-1}Pt following the ADT, only 33% and <1% of their initial activity, respectively. The improved stability and activity for the PtNW/S-CNT could be attributed to several factors: 1) 1D nature of S-CNT and Pt nanowires that facilitates easy mass/electron transport of reactants in the 3D architecture of PtNW/S-CNT; 2) fewer surface defects and preferential exposure of the (111) facets that exhibit higher specific activities; 3)

interaction of chemically bonded sulfur species in F-CNT with Pt nanowires that leads to stronger attraction and binding of nanowires and increased stability. Additionally, the adsorbed OH_{ad} species tend to bond strongly on the defect, step and edge sites of nanoparticles, which would have a negative impact on the ORR.[172] On the other hand, the 1D extended nanostructure of Pt nanowires should have a fewer number of these undesired sites. We also investigated the morphology of PtNW/S-CNT following the ADT and observed no visible morphology change **(Figure 7-4e)**. After 3000 cycles, Pt nanowires are still anchored on the S-CNT surface. An energy dispersive spectroscopy (EDS) color map of PtNW/S-CNT in **Figure 7-4f** indicates that sulfur atoms are well distributed along the length of the F-CNTs. Moreover, PtNWs tend to reside in areas rich in sulfur content, reflecting the affinity and strong binding between Pt nanowires and S-CNT. This clearly confirms the beneficial impact of S-CNT in hindering the dissolution, ripening and aggregation of Pt nanowires, which would otherwise reduce both ORR activity and stability. On the other hand, the morphologies of PtNW/F-CNT and Pt/C were significantly affected by the harsh ADT conditions, leading to severe catalyst degradation and aggregation along with nanoparticle agglomerates (see **Figure A-35** in the appendix).

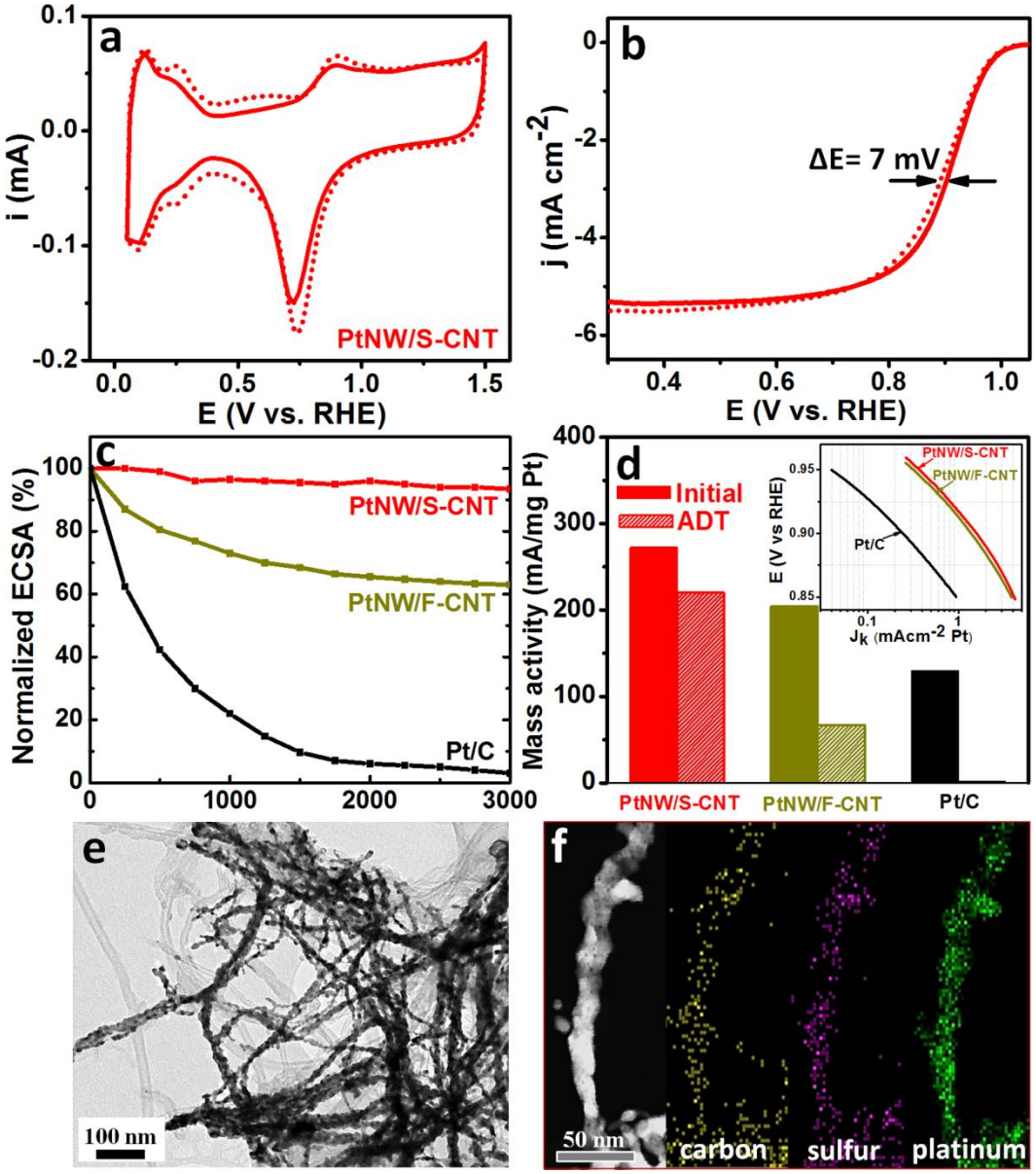

Figure 7-4 a-b) CVs and ORR, c) ECSA, d) Pt mass activities, e-f) TEM/EDX on PtNW/S-CNT.

7.4 Conclusions

In conclusion, novel 1D S-CNT materials were prepared to support 1D Pt nanowires for ORR. The interconnected 3D nano-assemblies of Pt nanowires and S-CNT show higher electrochemical activity and a remarkable long-term stability compared to the commercial Pt/C catalyst. After 3000 cycles of ADT, PtNW/S-CNT demonstrated outstanding stability, retaining 93% of its initial ECSA, while

PtNW/CNT and Pt/C retained only 62 and <1% of their initial ECSA, respectively. Additionally, PtNW/S-CNT displayed only a 7 mV decrease in half-wave potential, a dramatic improvement over PtNW/CNT and commercial Pt/C, which demonstrated 54 and >400 mV losses in half-wave potential, respectively. The Pt-based mass activity retention of PtNW/S-CNT was superior to that of PtNW/CNT and commercial Pt/C. PtNW/S-CNT also exhibited an excellent specific activity of 1.61 mA cm^{-2}, suppressing the DOE recommended target of 0.72 mA cm^{-2}_{Pt}. The performance enhancement exclusively illustrates the beneficial impact of S-CNT as a new class of supports for PtNWs for the ORR and, the catalyst will have potential to replace the conventional cathode catalysts for practical applications.

Chapter 8 Summary and Future Work

8.1 Summary

The objectives of this thesis are to deliver advanced electrode materials with excellent ORR activity and stability for PEMFC cathodes. The specific approaches include: (i) development of unique support materials such as SG and S-CNT and (ii) deposition of Pt nanoparticles and nanowires onto these support materials. These approaches are based on the hypothesis that the proper combination of Pt nanostructures with stable supports will provide unique functionality to address the technical targets set for PEMFC electrocatalysts.

In Chapter 4, SG-supported Pt nanoparticles (Pt/SG) were prepared. The materials were extensively characterized both physicochemically and electrochemically to determine their activity towards the ORR. Based on half-cell investigations, Pt/SG demonstrated improved ORR activity and excellent stability through the ADT, superior to that of Pt/G and commercial Pt/C and revealed the beneficial effects of sulfur dopants in graphene supports. Computational simulations which were conducted to help explain the outstanding electrochemical stability of Pt/SG showed that sulfur doping of graphene can provide stronger interactions with Pt and enhance the nanoparticle cohesive energies. Furthermore, the sulfur dopants modulate the electronic properties of Pt by causing a negative shift in its d-band which in turn would be expected to enhance ORR kinetics as observed experimentally. By effectively coupling experimental and computational investigations, we have demonstrated that SG materials can be considered a very promising new class of catalyst support materials that enhance ORR activity and catalyst stability and so significantly advance the current state of PEMFC catalyst technology.

The beneficial impacts of SG were utilized by growing extended surface Pt nanowires in order to achieve further improvement of catalytic activity and stability. In Chapter 5, SG-supported Pt nanowires (PtNW/SG) were prepared by a simple solvothermal technique. An investigation of the growth mechanism of PtNW/SG revealed that nanowires are comprised of numerous single crystalline nanoparticles attached and oriented along the <111> crystallographic direction. PtNW/SG exhibited an improved ORR activity and a remarkable stability in comparison with PtNW/G and commercial Pt/C catalysts under harsh, potentiodynamic conditions (potential range: 0.05 to 1.5 V vs RHE). After 3000 cycles of ADT, PtNW/SG retained 58% of its initial ECSA, superior to the 28%

and less than 1% retention by PtNW/G and commercial Pt/C, respectively. The Pt-based mass activity retention of PtNW/SG was also superior to that of PtNW/G and commercial Pt/C.

Chapter 6 focused further on the very important role of sulfur in SG-supported Pt nanowires catalysts. To elucidate this, a series of SG materials with varying sulfur contents ranging from 0.35 to 3.95 at% were prepared. We found that the amount of sulfur significantly affected the ORR kinetics of nanowire catalysts due to the influence of the sulfur dopants present in SG. PtNW/SG with 1.40 at% sulfur showed the best electrode kinetic performance with a high exchange current density and low activation energy. This leads to a weakened interaction between the nonreactive oxygenated species and Pt surface atoms that is beneficial for enhancing ORR kinetics.

In Chapter 7, S-CNT-supported Pt nanowires (PtNW/S-CNT) were prepared for the ORR. PtNW/S-CNT possesses unique interconnecting three-dimensional scaffolds that can facilitate the reactant molecule and electron transfer beneficial for ORR. PtNW/S-CNT exhibited an increased ORR activity and outstanding stability compared to the PtNW/F-CNT and commercial Pt/C catalyst. After 3000 cycles of ADT over a potential range of 0.05 to 1.5 V vs RHE, PtNW/S-CNT retained 93% of its initial ECSA, while PtNW/F-CNT and Pt/C retained only 62 and <1% of their initial ECSA, respectively. Moreover, the Pt-based mass activity retention achieved by PtNW/S-CNT was exceptional in comparison with PtNW/F-CNT and commercial Pt/C. The performance enhancement demonstrates the beneficial impact of S-CNT as a new class of supports for Pt nanowires for the ORR which can be integrated into MEAs.

8.2 Future work

It is recommended that future projects be rationally designed to leverage the progress and catalyst technologies developed throughout the present thesis. These projects should focus on: (i) rigorous durability investigation of Pt/SG, PtNW/SG and PtNW/S-CNT under PEMFC conditions and elucidation of the mechanistic pathways of performance loss, (ii) integration of Pt/SG, PtNW/SG and PtNW/S-CNT into MEAs and optimization of the developed catalysts for practical PEMFC demonstration.

(i) Rigorous durability investigations

It is highly desirable to rigorously evaluate the durability capabilities of the developed catalyst materials. For example, Pt/SG was subjected to ADT over a potential range from 0.05 to 1.3 V vs RHE for only 1500 cycles in a nitrogen-saturated electrolyte. However, Pt/SG should be subjected to

ADT between 0.05 and 1.6 V for 5000 cycles to elucidate both the catalytic activity and structure and the corrosion resistance of the graphene/CNT support materials. Moreover, different ADT protocols should be coupled with post-testing characterization of the developed catalysts. For example, catalysts subjected to various ADT protocols designed to induce different degradation pathways can then be investigated by TEM and EDX to elucidate the change in the properties and structure of the materials.

(ii) MEA integration

From a practical point of view, successful integration of Pt/SG, PtNW/SG and PtNW/S-CNT catalysts into an MEA is the ultimate objective and is necessary if the findings presented here are to have any impact on the real world application of PEMFCs. The electrode integration studies involve optimization of catalyst layer preparation by investigating the impact of catalyst ink solvent, concentration and deposition methods such as spraying, decal, etc. on MEA performance. The electrode thickness and the loading of developed catalysts can be varied to determine the impact on resulting PEMFC performance. A strategy that may be beneficial is to have platinum loading the catalyst layer that varies with electrode thickness (**Figure 8-1**).[256] Understanding and control of the thickness, structure and properties of electrode and maximization of the Pt utilization are necessary to improve the performance of PEMFCs. Also, correlation of the structural properties of the electrode (e.g., porosity and ionomer distribution) to MEA performance data will be important for a better understanding of their impacts and obtaining the best performing MEA catalyst for practical PEMFC applications.

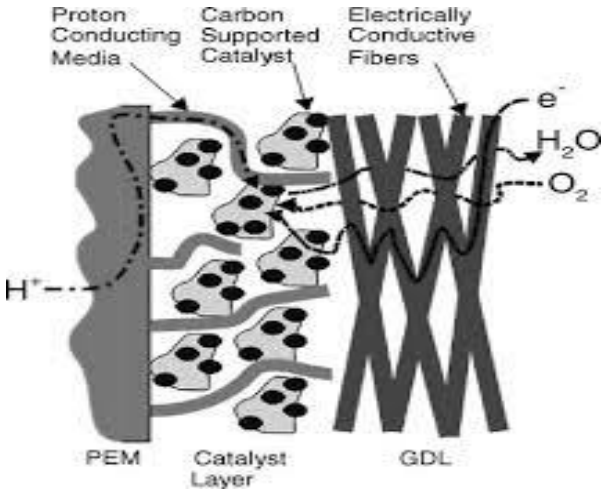

Figure 8-1. Method of integrating Pt/SG, PtNW/SG and PtNW/S-CNT catalysts for MEA evaluation.

References

1. L. Chen, D. Chen, M. Tong, H. Y. Leng, D. M. Chen, H. M. Cheng and K. Yang, *Rare Metal Mat Eng*, 2001, **30**, 196-198.
2. D. Lee, H. C. Lee, K. H. Lee, E. Y. Ko, Y. H. Kim and E. D. Park, *Abstr Pap Am Chem S*, 2007, **234**.
3. Y. H. Bing, H. S. Liu, L. Zhang, D. Ghosh and J. J. Zhang, *Chem Soc Rev*, 2010, **39**, 2184-2202.
4. United States Deparment of Energy: Technical Plan – Fuel Cells (2012) http://www1.eere.energy.gov/hydrogenandfuelcells/mypp/pdfs/fuel_cells.pdf.
5. L. Carrette, K. A. Friedrich and U. Stimming, *Chemphyschem*, 2000, **1**, 162-193.
6. H. A. Gasteiger, S. S. Kocha, B. Sompalli and F. T. Wagner, *Appl Catal B-Environ*, 2005, **56**, 9-35.
7. R. Borup, J. Meyers, B. Pivovar, Y. S. Kim, R. Mukundan, N. Garland, D. Myers, M. Wilson, F. Garzon and D. Wood, *Chemical Reviews (Washington, DC, United States)*, 2007, **107**, 3904-3951.
8. Y. Shao, S. Zhang, C. Wang, Z. Nie, J. Liu, Y. Wang and Y. Lin, *J Power Sources*, 2010, **195**, 4600-4605.
9. Z. Luo, D. Li, H. Tang, M. Pan and R. Ruan, *Int J Hydrogen Energ*, 2006, **31**, 1831-1837.
10. N. Jha, A. L. M. Reddy, M. M. Shaijumon, N. Rajalakshmi and S. Ramaprabhu, *Int J Hydrogen Energ*, 2008, **33**, 427-433.
11. A. L. Dicks, *J Power Sources*, 2006, **156**, 128-141.
12. R. Ryoo, S. H. Joo and S. Jun, *J Phys Chem B*, 1999, **103**, 7743-7746.
13. S. Q. Song, Y. R. Liang, Z. H. Li, Y. Wang, R. W. Fu, D. C. Wu and P. Tsiakaras, *Appl Catal B-Environ*, 2010, **98**, 132-137.
14. J. R. C. Salgado, F. Alcaide, G. Alvarez, L. Calvillo, M. J. Lazaro and E. Pastor, *J Power Sources*, 2010, **195**, 4022-4029.
15. K. S. Novoselov, A. K. Geim, S. V. Morozov, D. Jiang, M. I. Katsnelson, I. V. Grigorieva, S. V. Dubonos and A. A. Firsov, *Nature*, 2005, **438**, 197-200.
16. H. L. Guo, X. F. Wang, Q. Y. Qian, F. B. Wang and X. H. Xia, *Acs Nano*, 2009, **3**, 2653-2659.
17. L. T. Qu, Y. Liu, J. B. Baek and L. M. Dai, *Acs Nano*, 2010, **4**, 1321-1326.
18. R. T. Lv and M. Terrones, *Mater Lett*, 2012, **78**, 209-218.
19. Z. Yang, Z. Yao, G. F. Li, G. Y. Fang, H. G. Nie, Z. Liu, X. M. Zhou, X. Chen and S. M. Huang, *Acs Nano*, 2012, **6**, 205-211.
20. D. B. Mawhinney, V. Naumenko, A. Kuznetsova, J. T. Yates, J. Liu and R. E. Smalley, *J Am Chem Soc*, 2000, **122**, 2383-2384.
21. T. W. Ebbesen, H. Hiura, M. E. Bisher, M. M. J. Treacy, J. L. ShreeveKeyer and R. C. Haushalter, *Adv Mater*, 1996, **8**, 155-&.
22. F. Coloma, A. Sepulvedaescribano, J. L. G. Fierro and F. Rodriguezreinoso, *Langmuir*, 1994, **10**, 750-755.
23. Z. Lin, L. W. Ji, W. E. Krause and X. W. Zhang, *J Power Sources*, 2010, **195**, 5520-5526.
24. J. S. Zheng, X. S. Zhang, P. Li, J. Zhu, X. G. Zhou and W. K. Yuan, *Electrochem Commun*, 2007, **9**, 895-900.
25. P. A. Denis, R. Faccio and A. W. Mombru, *Chemphyschem*, 2009, **10**, 715-722.
26. J. H. Kwak, J. Z. Hu, D. Mei, C. W. Yi, D. H. Kim, C. H. F. Peden, L. F. Allard and J. Szanyi, *Science*, 2009, **325**, 1670-1673.

27. H. T. Liu, Y. Q. Liu and D. B. Zhu, *J Mater Chem*, 2011, **21**, 3335-3345.
28. R. L. Liu, D. Q. Wu, X. L. Feng and K. Mullen, *Angew Chem Int Edit*, 2010, **49**, 2565-2569.
29. Z. H. Sheng, L. Shao, J. J. Chen, W. J. Bao, F. B. Wang and X. H. Xia, *Acs Nano*, 2011, **5**, 4350-4358.
30. J. P. Paraknowitsch, A. Thomas and J. Schmidt, *Chem Commun*, 2011, **47**, 8283-8285.
31. K. Y. Chan, J. Ding, J. W. Ren, S. A. Cheng and K. Y. Tsang, *J Mater Chem*, 2004, **14**, 505-516.
32. Y. J. Wang, D. P. Wilkinson and J. J. Zhang, *Chem Rev*, 2011, **111**, 7625-7651.
33. S. Sharma and B. G. Pollet, *Journal of Power Sources*, 2012, **208**, 96-119.
34. S. Shrestha, Y. Liu and W. E. Mustain, *Cat. Rev.*, 2011, **53**, 256-336.
35. Y. Sun, Q. Wu and G. Shi, *Energ Environ Sci*, 2011, **4**, 1113-1132.
36. M. K. Debe, *Nature*, 2012, **486**, 43-51.
37. E. Antolini, *Applied Catalysis, B: Environmental*, 2012, **123–124**, 52-68.
38. D. U. Lee, H. W. Park, D. Higgins, L. Nazar and Z. Chen, *J Electrochem Soc*, 2013, **160**, F910-F915.
39. D. Higgins, Z. Chen, D. U. Lee and Z. Chen, *J Mater Chem A*, 2013, **1**, 2639-2645.
40. D. Geng, Y. Chen, Y. Chen, Y. Li, R. Li, X. Sun, S. Ye and S. Knights, *Energ Environ Sci*, 2011, **4**, 760-764.
41. D. Higgins, Z. Chen and Z. Chen, *Electrochim Acta*, 2011, **56**, 1570-1575.
42. D. C. Higgins, J. Wu, W. M. Li and Z. W. Chen, *Electrochim Acta*, 2012, **59**, 8-13.
43. Z. Chen, D. Higgins, H. Tao, R. S. Hsu and Z. Chen, *J Phys Chem C*, 2009, **113**, 21008-21013.
44. K. Gong, F. Du, Z. Xia, M. Durstock and L. Dai, *Science*, 2009, **323**, 760-764.
45. L. Qu, Y. Liu, J.-B. Baek and L. Dai, *Acs Nano*, 2010, **4**, 1321-1326.
46. G. Wu, N. H. Mack, W. Gao, S. Ma, R. Zhong, J. Han, J. K. Baldwin and P. Zelenay, *Acs Nano*, 2012, **6**, 9764-9776.
47. Y. Chen, J. Wang, H. Liu, M. N. Banis, R. Li, X. Sun, T.-K. Sham, S. Ye and S. Knights, *J Phys Chem C*, 2011, **115**, 3769-3776.
48. Y. Chen, J. Wang, H. Liu, R. Li, X. Sun, S. Ye and S. Knights, *Electrochem Commun*, 2009, **11**, 2071-2076.
49. D. C. Higgins, D. Meza and Z. W. Chen, *J Phys Chem C*, 2010, **114**, 21982-21988.
50. R. Imran Jafri, N. Rajalakshmi and S. Ramaprabhu, *J Mater Chem*, 2010, **20**, 7114-7117.
51. S. Sun, G. Zhang, Y. Zhong, H. Liu, R. Li, X. Zhou and X. Sun, *Chem Commun*, 2009, 7048-7050.
52. M. N. Banis, S. Sun, X. Meng, Y. Zhang, Z. Wang, R. Li, M. Cai, T.-K. Sham and X. Sun, *J Phys Chem C*, 2013, **117**, 15457-15467.
53. D. Geng, Y. Hu, Y. Li, R. Li and X. Sun, *Electrochem Commun*, 2012, **22**, 65-68.
54. Y. Zhou, K. Neyerlin, T. S. Olson, S. Pylypenko, J. Bult, H. N. Dinh, T. Gennett, Z. Shao and R. O'Hayre, *Energ Environ Sci*, 2010, **3**, 1437-1446.
55. Y.-H. Li, T.-H. Hung and C.-W. Chen, *Carbon*, 2009, **47**, 850-855.
56. M. N. Groves, A. S. W. Chan, C. Malardier-Jugroot and M. Jugroot, *Chem Phys Lett*, 2009, **481**, 214-219.
57. M. N. Groves, C. Malardier-Jugroot and M. Jugroot, *J Phys Chem C*, 2012, **116**, 10548-10556.
58. T. Holme, Y. Zhou, R. Pasquarelli and R. O'Hayre, *Phys Chem Chem Phys*, 2010, **12**, 9461-9468.
59. J. Liang, Y. Jiao, M. Jaroniec and S. Z. Qiao, *Angewandte Chemie*, 2012, **51**, 11496-11500.

60. S. Yang, L. Zhi, K. Tang, X. Feng, J. Maier and K. Müllen, *Adv Funct Mater*, 2012, **22**, 3634-3640.
61. R. Wang, D. C. Higgins, M. A. Hoque, D. Lee, F. Hassan and Z. Chen, *Sci. Rep.*, 2013, **3**.
62. S. M. Choi, J. H. Kim, J. Y. Jung, E. Y. Yoon and W. B. Kim, *Electrochim Acta*, 2008, **53**, 5804-5811.
63. E. P. Lee, Z. M. Peng, W. Chen, S. W. Chen, H. Yang and Y. N. Xia, *Acs Nano*, 2008, **2**, 2167-2173.
64. K. Lee, J. J. Zhang, H. J. Wang and D. P. Wilkinson, *J Appl Electrochem*, 2006, **36**, 507-522.
65. S. J. Guo, D. G. Li, H. Y. Zhu, S. Zhang, N. M. Markovic, V. R. Stamenkovic and S. H. Sun, *Angew Chem Int Edit*, 2013, **52**, 3465-3468.
66. B. Y. Xia, H. B. Wu, Y. Yan, X. W. Lou and X. Wang, *J Am Chem Soc*, 2013, **135**, 9480-9485.
67. B. Li, D. C. Higgins, S. M. Zhu, H. Li, H. J. Wang, J. X. Ma and Z. W. Chen, *Catal Commun*, 2012, **18**, 51-54.
68. F. Jaouen, E. Proietti, M. Lefevre, R. Chenitz, J.-P. Dodelet, G. Wu, H. T. Chung, C. M. Johnston and P. Zelenay, *Energ Environ Sci*, 2011, **4**, 114-130.
69. Z. Chen, D. Higgins, A. Yu, L. Zhang and J. Zhang, *Energ Environ Sci*, 2011, **4**, 3167-3192.
70. http://www1.eere.energy.gov/hydrogenandfuelcells/mypp/pdfs/fuel_cells.pdf.
71. R. Borup, J. Meyers, B. Pivovar, Y. S. Kim, R. Mukundan, N. Garland, D. Myers, M. Wilson, F. Garzon and D. Wood, *Chem Rev*, 2007, **107**, 3904-3951.
72. D. C. Higgins, J.-Y. Choi, J. Wu, A. Lopez and Z. Chen, *J Mater Chem*, 2012, **22**, 3727-3732.
73. R. S. Hsu, D. Higgins and Z. Chen, *Nanotechnology*, 2010, **21**, 165705-165710.
74. Y.-J. Wang, D. P. Wilkinson and J. Zhang, *Chem Rev*, 2011, **111**, 7625-7651.
75. S.-Y. Huang, P. Ganesan, S. Park and B. N. Popov, *J Am Chem Soc*, 2009, **131**, 13898-13899.
76. Y. Shao, J. Sui, G. Yin and Y. Gao, *Applied Catalysis, B: Environmental*, 2008, **79**, 89-99.
77. J. Zhou, X. Zhou, X. Sun, R. Li, M. Murphy, Z. Ding, X. Sun and T.-K. Sham, *Chem Phys Lett*, 2007, **437**, 229-232.
78. C. T. Campbell, *Nat. Chem.*, 2012, **4**, 597-598.
79. S. Sharma and B. G. Pollet, *J Power Sources*, 2012, **208**, 96-119.
80. D. C. Marcano, D. V. Kosynkin, J. M. Berlin, A. Sinitskii, Z. Z. Sun, A. Slesarev, L. B. Alemany, W. Lu and J. M. Tour, *Acs Nano*, 2010, **4**, 4806-4814.
81. B. P. Vinayan, R. Nagar, N. Rajalakshmi and S. Ramaprabhu, *Adv Funct Mater*, 2012, **22**, 3519-3526.
82. P. Hohenberg and W. Kohn, *Phys. Rev.*, 1964, **136**, B864–B871.
83. W. Kohn and L. J. Sham, *Phys. Rev. A*, 1965, **140**, 1133–A1138.
84. G. Kresse and J. Furthmüller, *Phys. Rev. B*, 1996, **54**, 11169-11186.
85. J. P. Perdew, K. Burke and M. Ernzerhof, *Phys. Rev. Lett.*, 1996, **77**, 3865-3868.
86. G. Kresse and J. Furthmuller, *Comput. Mater. Sci.*, 1996, **6**, 15-50.
87. P. E. Blöchl, *Phys. Rev. B*, 1994, **50**, 17953-17979.
88. G. Kresse and D. Joubert, *Phys. Rev. B*, 1999, **59**, 1758 -1775.
89. M. Methfessel and A. T. Paxton, *Phys. Rev. B*, 1989, **40**, 3616−3621.
90. P. E. Blöchl, O. Jepsen and O. K. Andersen, *Phys. Rev. B*, 1994, **49**, 16223–16233.
91. J. Steidel, J. Pickardt and R. Steudel, *Z. Naturforsch.B*, 1978, **33**, 1554-1555.
92. W. Li, X. Wang, Z. Chen, M. Waje and Y. Yan, *J Phys Chem B*, 2006, **110**, 15353-15358.
93. A. C. Ferrari and D. M. Basko, *Nature Nanotechnology*, 2013, **8**, 235-246.
94. S. M. Choi, M. H. Seo, H. J. Kim and W. B. Kim, *Carbon*, 2011, **49**, 904-909.

95. J.-D. Qiu, G.-C. Wang, R.-P. Liang, X.-H. Xia and H.-W. Yu, *J Phys Chem C*, 2011, **115**, 15639-15645.
96. B. Seger and P. V. Kamat, *J Phys Chem C*, 2009, **113**, 7990-7995.
97. C. H. Choi, S. H. Park and S. I. Woo, *Green Chemistry*, 2011, **13**, 406-412.
98. A. Barrie, I. W. Drummond and Q. C. Herd, *Journal of Electron Spectroscopy and Related Phenomena*, 1974, **5**, 217-225.
99. M. E. Labib, J. H. Thomas Iii and D. D. Embert, *Carbon*, 1984, **22**, 445-451.
100. Y. Chang, F. Hong, C. He, Q. Zhang and J. Liu, *Adv Mater*, 2013, **25**, 4794-4799.
101. I. Herrmann, U. I. Kramm, J. Radnik, S. Fiechter and P. Bogdanoff, *J Electrochem Soc*, 2009, **156**, B1283-B1292.
102. S. Sun, G. Zhang, N. Gauquelin, N. Chen, J. Zhou, S. Yang, W. Chen, X. Meng, D. Geng, M. N. Banis, R. Li, S. Ye, S. Knights, G. A. Botton, T.-K. Sham and X. Sun, *Sci. Rep.*, 2013, **3**, 1775-1784.
103. G. Wu, Y.-S. Chen and B.-Q. Xu, *Electrochem Commun*, 2005, **7**, 1237-1243.
104. R. Ahmadi and M. K. Amini, *Int J Hydrogen Energ*, 2011, **36**, 7275-7283.
105. D. He, K. Cheng, H. Li, T. Peng, F. Xu, S. Mu and M. Pan, *Langmuir*, 2012, **28**, 3979-3986.
106. R. Kou, Y. Shao, D. Wang, M. H. Engelhard, J. H. Kwak, J. Wang, V. V. Viswanathan, C. Wang, Y. Lin, Y. Wang, I. A. Aksay and J. Liu, *Electrochem Commun*, 2009, **11**, 954-957.
107. J. Fu, M. Hou, C. Du, Z. Shao and B. Yi, *J Power Sources*, 2009, **187**, 32-38.
108. K. Hartl, M. Hanzlik and M. Arenz, *Energ Environ Sci*, 2011, **4**, 234-238.
109. D. C. Higgins, S. Ye, S. Knights and Z. Chen, *Electrochemical and Solid-State Letters*, 2012, **15**, B83-B85.
110. B. Han, V. Viswanathan and H. Pitsch, *J. Phys. Chem. C*, 2012, **116**, 6174−6183.
111. Y. Okamoto, *Appl. Surf. Sci.*, 2009, **256** 335–341.
112. E. Cruz-Silva, D. A. Cullen, L. Gu, J. M. Romo-Herrera, E. Muñoz-Sandoval, F. López-Urías, B. G. Sumpter, V. Meunier, J.-C. Charlier, D. J. Smith, H. Terrones and M. Terrones, *Acs Nano*, 2008, **2**, 441-448.
113. E. Cruz-Silva, F. Lopez-Urias, E. Munoz-Sandoval, B. G. Sumpter, H. Terrones, J. C. Charlier, V. Meunier and M. Terrones, *Nanoscale*, 2011, **3**, 1008-1013.
114. M. Endo, T. Hayashi, S.-H. Hong, T. Enoki and M. S. Dresselhaus, *J. Appl. Phys.*, 2001, **90**, 5670-5674.
115. H. Kim, K. Lee, S. I. Woo and Y. Jung, *Phys. Chem. Chem. Phys.*, 2011, **13**, 17505-17510.
116. K. R. Lee, K. U. Lee, J. W. Lee, B. T. Ahn and S. I. Woo, *Electrochem. Commun.*, 2010, **12**, 1052-1055.
117. Z. W. Liu, F. Peng, H. J. Wang, H. Yu, W. X. Zheng and J. Yang, *Angew. Chem. Int. Ed.*, 2011, **123**, 3315-3319.
118. B. Shan and K. Cho, *Chem. Phys. Let.*, 2010, **492**, 131-136.
119. L. Zhang and Z. Xia, *J. Phys. Chem. C*, 2011, **115**, 11170–11176.
120. Y. Wang, Y. Shao, D. W. Matson, J. Li and Y. Lin, *Acs Nano*, 2010, **4**, 1790-1798.
121. M. I. Katsnelson, *Mater. Today*, 2007, **10**, 20–27.
122. R. Lv and M. Terrones, *Mater Lett*, 2012, **78** 209–218.
123. K. S. Novoselov, A. K. Geim, S. V. Morozov, D. Jiang, M. I. Katsnelson, I. V. Grigorieva, S. V. Dubonos and A. A. Firsov, *Nature*, 2004, **438**, 197-200.
124. S. M. Choi, M. H. Seo, H. J. Kim and W. B. Kim, *Carbon*, 2011, **49**, 904–909.
125. R. F. W. Bader, *Atoms in Molecules: A Quantum Theory*, Oxford University Press, USA, 1994.
126. J. H. Kim, S. M. Choi, S. H. Nam, M. H. Seo, S. H. Choi and W. B. Kim, *Appl. Catal. B: Environ.*, 2008, **82**, 89–102.

127. S. Mukerjee, S. Srinivasan and M. P. Soriaga, *J. Electrochem. Soc.*, 1995 **142**, 1409-1422.
128. M. H. Seo, S. M. Choi, J. K. Seo, S. H. Noh, W. B. Kim and B. Hana, *Appl. Catal. B: Environ.*, 2013, **129** 163– 171.
129. D. R. Lide, *CRC handbook of chemistry and physics (86th edition)*, CRC Press, 2005.
130. S. H. Joo, S. J. Choi, I. Oh, J. Kwak, Z. Liu, O. Terasaki and R. Ryoo, *Nature*, 2001, **412**, 169-172.
131. M. H. Seo, S. M. Choi, H. J. Kim and W. B. Kim, *Electrochem. Commun.*, 2011, **13** 182-185.
132. U. B. Demirci, *J. Power Sources*, 2007, **173** 11–18.
133. J. Greeley and M. Mavrikakis, *Nat. Mater.*, 2004, **3**, 810–815.
134. J. Greeley, I. E. L. Stephens, A. S. Bondarenko, T. P. Johansson, H. A. Hansen, T. F. Jaramillo, J. Rossmeisl, I. Chorkendorff and J. K. Nørskov, *Nature Chem.*, 2009, **1**, 552–556.
135. B. Hammer and J. K. Norskov, *Nature*, 1995, **376**, 238–240
136. B. Hammer and J. K. Norskov, *Surf. Sci.*, 1995, **343**, 211–220.
137. M. Shao, K. Sasaki, N. S. Marinkovic, L. Zhang and R. R. Adzic, *Electrochem. Commun.*, 2007, **9**, 2848–2853.
138. M. H. Shao, T. Huang, P. Liu, J. Zhang, K. Sasaki, M. B. Vukmirovic and R. R. Adzic, *Langmuir*, 2006, **22**, 10409–10415.
139. M. H. Shao, P. Liu, J. Zhang and R. R. Adzic, *J. Phys. Chem. B*, 2007, **111**, 6772-6775.
140. Z. Chen, M. Waje, W. Li and Y. Yan, *Angewandte Chemie*, 2007, **46**, 4060-4063.
141. D. F. van der Vliet, C. Wang, D. Tripkovic, D. Strmcnik, X. F. Zhang, M. K. Debe, R. T. Atanasoski, N. M. Markovic and V. R. Stamenkovic, *Nat Mater*, 2012, **11**, 1051-1058.
142. C. Wang, M. Chi, D. Li, D. Strmcnik, D. van der Vliet, G. Wang, V. Komanicky, K.-C. Chang, A. P. Paulikas, D. Tripkovic, J. Pearson, K. L. More, N. M. Markovic and V. R. Stamenkovic, *J Am Chem Soc*, 2011, **133**, 14396-14403.
143. H. Zhu, S. Zhang, S. Guo, D. Su and S. Sun, *J Am Chem Soc*, 2013, **135**, 7130-7133.
144. B. C. Han, C. R. Miranda and G. Ceder, *Phys. Rev. B*, 2008, **77**, 75410-75419
145. S. H. Noh, M. H. Seo, J. K. Seo, P. Fischer and B. C. Han, *Nanoscale*, 2013, **5**, 8625-8633.
146. P. Kratzer, B. Hammer and J. K. Nørskov, *J. Chem. Phys.*, 1996, **105** 5595-6005.
147. L. Li, S. G. Chen, Z. D. Wei, X. Q. Qi, M. R. Xia and Y. Q. Wang, *Phys Chem Chem Phys*, 2012, **14**, 16581-16587.
148. J. K. Seo, A. Khetan, M. H. Seo, H. Kim and B. Han, *J.Power Sources*, 2013, **238** 137-143.
149. W. H. Qi and M. P. Wang, *J. Mater. Sci. Lett.*, 2002, **21**, 1743-1745.
150. L. Tang, B. Han, K. Persson, C. Friesen, T. He, K. Sieradzki and G. Ceder, *J Am Chem Soc*, 2010, **132**, 596–600.
151. S. M. Alia, K. Jensen, C. Contreras, F. Garzon, B. Pivovar and Y. S. Yan, *Acs Catal*, 2013, **3**, 358-362.
152. Z. W. Chen, M. Waje, W. Z. Li and Y. S. Yan, *Angew Chem Int Edit*, 2007, **46**, 4060-4063.
153. D. C. Higgins, S. Y. Ye, S. Knights and Z. W. Chen, *Electrochem Solid St*, 2012, **15**, B83-B85.
154. C. Koenigsmann, A. C. Santulli, K. P. Gong, M. B. Vukmirovic, W. P. Zhou, E. Sutter, S. S. Wong and R. R. Adzic, *J Am Chem Soc*, 2011, **133**, 9783-9795.
155. S. H. Sun, F. Jaouen and J. P. Dodelet, *Adv Mater*, 2008, **20**, 3900-3904.
156. S. H. Sun, G. X. Zhang, D. S. Geng, Y. G. Chen, M. N. Banis, R. Y. Li, M. Cai and X. L. Sun, *Chem-Eur J*, 2010, **16**, 829-835.
157. S. H. Sun, G. X. Zhang, Y. Zhong, H. Liu, R. Y. Li, X. R. Zhou and X. L. Sun, *Chem Commun*, 2009, 7048-7050.
158. V. Chabot, D. Higgins, A. P. Yu, X. C. Xiao, Z. W. Chen and J. J. Zhang, *Energ Environ Sci*, 2014, **7**, 1564-1596.

159. J. E. Park, Y. J. Jang, Y. J. Kim, M. S. Song, S. Yoon, D. H. Kim and S. J. Kim, *Phys Chem Chem Phys*, 2014, **16**, 103-109.
160. D. Higgins, M. A. Hoque, M. H. Seo, R. Wang, F. Hassan, J.-Y. Choi, M. Pritzker, A. Yu, J. Zhang and Z. Chen, *Adv Funct Mater*, 2014, **24**, 4325-4336.
161. D. S. Li, M. H. Nielsen, J. R. I. Lee, C. Frandsen, J. F. Banfield and J. J. De Yoreo, *Science*, 2012, **336**, 1014-1018.
162. Z. Y. Tang and N. A. Kotov, *Adv Mater*, 2005, **17**, 951-962.
163. D. Azulai, E. Cohen and G. Markovich, *Nano Lett*, 2012, **12**, 5552-5558.
164. X. Xie, Y. Xue, L. Li, S. Chen, Y. Nie, W. Ding and Z. Wei, *Nanoscale*, 2014.
165. H. W. Liang, X. A. Cao, F. Zhou, C. H. Cui, W. J. Zhang and S. H. Yu, *Adv Mater*, 2011, **23**, 1467-1471.
166. S. H. Sun, G. X. Zhang, D. S. Geng, Y. G. Chen, R. Y. Li, M. Cai and X. L. Sun, *Angew Chem Int Edit*, 2011, **50**, 422-426.
167. L. Su, S. Shrestha, Z. H. Zhang, W. Mustain and Y. Lei, *J Mater Chem A*, 2013, **1**, 12293-12301.
168. N. Markovic, H. Gasteiger and P. N. Ross, *J Electrochem Soc*, 1997, **144**, 1591-1597.
169. D. F. van der Vliet, C. Wang, D. Tripkovic, D. Strmcnik, X. F. Zhang, M. K. Debe, R. T. Atanasoski, N. M. Markovic and V. R. Stamenkovic, *Nat. Mater.*, 2012, **11**, 1051-1058.
170. J. L. Zhang, M. B. Vukmirovic, Y. Xu, M. Mavrikakis and R. R. Adzic, *Angew Chem Int Edit*, 2005, **44**, 2132-2135.
171. J. Greeley, I. E. L. Stephens, A. S. Bondarenko, T. P. Johansson, H. A. Hansen, T. F. Jaramillo, J. Rossmeisl, I. Chorkendorff and J. K. Norskov, *Nat Chem*, 2009, **1**, 552-556.
172. V. R. Stamenkovic, B. Fowler, B. S. Mun, G. F. Wang, P. N. Ross, C. A. Lucas and N. M. Markovic, *Science*, 2007, **315**, 493-497.
173. I. E. L. Stephens, A. S. Bondarenko, F. J. Perez-Alonso, F. Calle-Vallejo, L. Bech, T. P. Johansson, A. K. Jepsen, R. Frydendal, B. P. Knudsen, J. Rossmeisl and I. Chorkendorff, *J Am Chem Soc*, 2011, **133**, 5485-5491.
174. Y. Kim, J. W. Hong, Y. W. Lee, M. Kim, D. Kim, W. S. Yun and S. W. Han, *Angew Chem Int Edit*, 2010, **49**, 10197-10201.
175. B. Lim, M. J. Jiang, P. H. C. Camargo, E. C. Cho, J. Tao, X. M. Lu, Y. M. Zhu and Y. N. Xia, *Science*, 2009, **324**, 1302-1305.
176. L. Y. Ruan, E. B. Zhu, Y. Chen, Z. Y. Lin, X. Q. Huang, X. F. Duan and Y. Huang, *Angew Chem Int Edit*, 2013, **52**, 12577-12581.
177. R. Y. Wang, D. C. Higgins, M. A. Hoque, D. Lee, F. Hassan and Z. W. Chen, *Sci Rep-Uk*, 2013, **3**.
178. D. Strmcnik, M. Escudero-Escribano, K. Kodama, V. R. Stamenkovic, A. Cuesta and N. M. Markovic, *Nat Chem*, 2010, **2**, 880-885.
179. A. Holewinski, J. C. Idrobo and S. Linic, *Nat Chem*, 2014, **6**, 941-941.
180. C. Wang, N. M. Markovic and V. R. Stamenkovic, *Acs Catal*, 2012, **2**, 891-898.
181. D. Zhao and B. Q. Xu, *Angewandte Chemie*, 2006, **118**, 5077-5081.
182. A. A. Topalov, I. Katsounaros, M. Auinger, S. Cherevko, J. C. Meier, S. O. Klemm and K. J. J. Mayrhofer, *Angew Chem Int Edit*, 2012, **51**, 12613-12615.
183. L. Tang, B. Han, K. Persson, C. Friesen, T. He, K. Sieradzki and G. Ceder, *J. Am. Chem. Soc.*, 2010, **132**, 596-600.
184. X. W. Yu and S. Y. Ye, *J Power Sources*, 2007, **172**, 145-154.
185. N. M. Markovic, T. J. Schmidt, V. Stamenkovic and P. N. Ross, *Fuel Cells*, 2001, **1**, 105-116.

186. L. J. Yang, M. B. Vukmirovic, D. Su, K. Sasaki, J. A. Herron, M. Mavrikakis, S. J. Liao and R. R. Adzic, *J Phys Chem C*, 2013, **117**, 1748-1753.
187. A. Holewinski and S. Linic, *J Electrochem Soc*, 2012, **159**, H864-H870.
188. J. X. Chen, J. B. Siegel, T. Matsuura and A. G. Stefanopoulou, *J Electrochem Soc*, 2011, **158**, B1164-B1174.
189. R. Y. Wang, C. X. Xu, X. X. Bi and Y. Ding, *Energ Environ Sci*, 2012, **5**, 5281-5286.
190. S. J. Guo, S. Zhang, D. Su and S. H. Sun, *J Am Chem Soc*, 2013, **135**, 13879-13884.
191. D. C. Higgins, R. Y. Wang, M. A. Hoque, P. Zamani, S. Abureden and Z. W. Chen, *Nano Energy*, 2014, **10**, 135-143.
192. R. Wang, D. C. Higgins, M. A. Hoque, D. Lee, F. Hassan and Z. Chen, *Sci Rep*, 2013, **3**, 2431.
193. C. Koenigsmann and S. S. Wong, *Energ Environ Sci*, 2011, **4**, 1161-1176.
194. Y. N. Xia, P. D. Yang, Y. G. Sun, Y. Y. Wu, B. Mayers, B. Gates, Y. D. Yin, F. Kim and Y. Q. Yan, *Adv Mater*, 2003, **15**, 353-389.
195. L. Cademartiri and G. A. Ozin, *Adv Mater*, 2009, **21**, 1013-1020.
196. Y. Y. Shao, G. P. Yin and Y. Z. Gao, *J Power Sources*, 2007, **171**, 558-566.
197. C. Wang, M. Waje, X. Wang, J. M. Tang, R. C. Haddon and Y. S. Yan, *Nano Lett*, 2004, **4**, 345-348.
198. M. A. Hoque, F. M. Hassan, D. Higgins, J. Y. Choi, M. Pritzker, S. Knights, S. Ye and Z. Chen, *Adv Mater*, 2015, **27**, 1229-1234.
199. M. A. Hogue, D. C. Higgins, F. M. Hassan, J. Y. Choi, M. D. Pritzker and Z. W. Chen, *Electrochim Acta*, 2014, **121**, 421-427.
200. Y. Jiang, J. Zhang, Y. H. Qin, D. F. Niu, X. S. Zhang, L. Niu, X. G. Zhou, T. H. Lu and W. K. Yuan, *J Power Sources*, 2011, **196**, 9356-9360.
201. M. M. Liu, R. Z. Zhang and W. Chen, *Chem Rev*, 2014, **114**, 5117-5160.
202. D. W. Kim, O. L. Li and N. Saito, *Phys Chem Chem Phys*, 2015, **17**, 407-413.
203. K. P. Gong, F. Du, Z. H. Xia, M. Durstock and L. M. Dai, *Science*, 2009, **323**, 760-764.
204. D. S. Yu, Q. Zhang and L. M. Dai, *J Am Chem Soc*, 2010, **132**, 15127-15129.
205. Y. Li, Y. Zhao, H. H. Cheng, Y. Hu, G. Q. Shi, L. M. Dai and L. T. Qu, *J Am Chem Soc*, 2012, **134**, 15-18.
206. C. H. Hsu, J. Y. Jan, H. P. Lin and P. L. Kuo, *New J Chem*, 2014, **38**, 5521-5526.
207. R. I. Jafri, N. Rajalakshmi and S. Ramaprabhu, *J Mater Chem*, 2010, **20**, 7114-7117.
208. S. H. Park, S. M. Bak, K. H. Kim, J. P. Jegal, S. I. Lee, J. Lee and K. B. Kim, *J Mater Chem*, 2011, **21**, 680-686.
209. A. Parthasarathy, S. Srinivasan, A. J. Appleby and C. R. Martin, *J Electrochem Soc*, 1992, **139**, 2530-2537.
210. A. Parthasarathy, C. R. Martin and S. Srinivasan, *J Electrochem Soc*, 1991, **138**, 916-921.
211. D. van der Vliet, D. S. Strmcnik, C. Wang, V. R. Stamenkovic, N. M. Markovic and M. T. M. Koper, *J Electroanal Chem*, 2010, **647**, 29-34.
212. G. Kresse and J. Furthmuller, *Phys Rev B*, 1996, **54**, 11169-11186.
213. P. E. Blochl, *Physical review. B, Condensed matter*, 1994, **50**, 17953-17979.
214. J. P. Perdew, K. Burke and Y. Wang, *Phys Rev B*, 1996, **54**, 16533-16539.
215. M. Methfessel and A. T. Paxton, *Phys. Rev. B*, 1989, **40**, 3616-3621.
216. X. H. Yang, J. W. Guo, S. Yang, Y. Hou, B. Zhang and H. G. Yang, *J Mater Chem A*, 2014, **2**, 614-619.
217. J. M. Gonzalez-Dominguez, P. Castell, S. Bespin-Gascon, A. Anson-Casaos, A. M. Diez-Pascual, M. A. Gomez-Fatou, A. M. Benito, W. K. Maser and M. T. Martinez, *J Mater Chem*, 2012, **22**, 21285-21297.

218. F. Guzman, M. Favre, H. M. Ruiz, S. Hevia, L. S. Caballero, E. S. Wyndham, H. Bhuyan, M. Flores and S. Mandl, *J Phys D Appl Phys*, 2013, **46**, 215202.
219. W. S. Tseng, C. Y. Tseng and C. T. Kuo, *Nanoscale Res Lett*, 2009, **4**, 234-239.
220. Z. Chen, D. Higgins and Z. W. Chen, *Carbon*, 2010, **48**, 3057-3065.
221. Z. Chen, D. Higgins, H. S. Tao, R. S. Hsu and Z. W. Chen, *J Phys Chem C*, 2009, **113**, 21008-21013.
222. F. M. Hassan, V. Chabot, J. D. Li, B. K. Kim, L. Ricardez-Sandoval and A. P. Yu, *J Mater Chem A*, 2013, **1**, 2904-2912.
223. B. K. Saikia, R. K. Boruah and P. K. Gogoi, *J Chem Sci*, 2009, **121**, 103-106.
224. C. F. Yuan, W. F. Chen and L. F. Yan, *J Mater Chem*, 2012, **22**, 7456-7460.
225. J. Tauc, Grigorov.R and A. Vancu, *Phys Status Solidi*, 1966, **15**, 627-637.
226. J. Tauc, *Science*, 1967, **158**, 1543-1548.
227. L. Ci, L. Song, C. H. Jin, D. Jariwala, D. X. Wu, Y. J. Li, A. Srivastava, Z. F. Wang, K. Storr, L. Balicas, F. Liu and P. M. Ajayan, *Nat Mater*, 2010, **9**, 430-435.
228. A. Mathkar, D. Tozier, P. Cox, P. J. Ong, C. Galande, K. Balakrishnan, A. L. M. Reddy and P. M. Ajayan, *J Phys Chem Lett*, 2012, **3**, 986-991.
229. S. Stankovich, D. A. Dikin, R. D. Piner, K. A. Kohlhaas, A. Kleinhammes, Y. Jia, Y. Wu, S. T. Nguyen and R. S. Ruoff, *Carbon*, 2007, **45**, 1558-1565.
230. Y. G. Chen, J. J. Wang, X. B. Meng, Y. Zhong, R. Y. Li, X. L. Sun, S. Y. Ye and S. Knights, *Int J Hydrogen Energ*, 2011, **36**, 11085-11092.
231. Y. J. Li, Y. J. Li, E. B. Zhu, T. McLouth, C. Y. Chiu, X. Q. Huang and Y. Huang, *J Am Chem Soc*, 2012, **134**, 12326-12329.
232. V. R. Stamenkovic, B. S. Mun, K. J. J. Mayrhofer, P. N. Ross and N. M. Markovic, *J Am Chem Soc*, 2006, **128**, 8813-8819.
233. J. K. Norskov, J. Rossmeisl, A. Logadottir, L. Lindqvist, J. R. Kitchin, T. Bligaard and H. Jonsson, *J Phys Chem B*, 2004, **108**, 17886-17892.
234. W. E. Ogrady, E. J. Taylor and S. Srinivasan, *J Electroanal Chem*, 1982, **132**, 137-150.
235. U. A. Paulus, A. Wokaun, G. G. Scherer, T. J. Schmidt, V. Stamenkovic, V. Radmilovic, N. M. Markovic and P. N. Ross, *J Phys Chem B*, 2002, **106**, 4181-4191.
236. D. B. Sepa, M. V. Vojnovic, L. M. Vracar and A. Damjanovic, *Electrochim Acta*, 1984, **29**, 1169-1170.
237. M. H. Seo, S. M. Choi, J. K. Seo, S. H. Noh, W. B. Kim and B. Han, *Appl. Catal. B: Environ.*, 2013, **129** 163– 171.
238. M. H. Seo, S. M. Choi, H. J. Kim and W. B. Kim, *Electrochem. Commun.*, 2011, **13**, 182-185.
239. M. H. Seo, S. M. Choi, H. J. Kim, J. H. Kim, B. K. Cho and W. B. Kim, *J Power Sources*, 2008, **179**, 81-86.
240. Y. Okamoto, *Appl. Surf. Sci.*, 2009, **256**, 335–341.
241. M. Endo, T. Hayashi, S.-H. Hong, T. Enoki and M. S. Dresselhaus, *J. Appl. Phys.*, 2001, **90**, 5670-5674.
242. H. Kim, K. Lee, S. I. Woo and Y. Jung, *PCCP*, 2011, **13**, 17505-17510.
243. K. R. Lee, K. U. Lee, J. W. Lee, B. T. Ahn and S. I. Woo, *Electrochem. Commun.*, 2010, **12**, 1052-1055.
244. L. Zhang and Z. Xia, *J. Phys. Chem. C.*, 2011, **115**, 11170–11176.
245. M. H. Seo, S. M. Choi, E. J. Lim, I. H. Kwon, J. K. Seo, S. H. Noh, W. B. Kim and B. Han, *Chemsuschem*, 2014, **7**, 2609-2620.
246. D. Higgins, M. A. Hoque, M. H. Seo, R. Wang, F. Hassan, J.-Y. Choi, M. Pritzker, A. Yu, J. Zhang and Z. Chen, *Adv. Funct. Mater.*, 2014, **24**, 4325–4336.

247. Y. Nie, L. Li and Z. D. Wei, *Chem Soc Rev*, 2015, **44**, 2168-2201.
248. Z. M. Peng and H. Yang, *J Am Chem Soc*, 2009, **131**, 7542-7543.
249. B. Y. Xia, W. T. Ng, H. B. Wu, X. Wang and X. W. Lou, *Angew Chem Int Edit*, 2012, **51**, 7213-7216.
250. C. Koenigsmann, W. P. Zhou, R. R. Adzic, E. Sutter and S. S. Wong, *Nano Lett*, 2010, **10**, 2806-2811.
251. Y. Liu, D. G. Li and S. S. Sun, *J Mater Chem*, 2011, **21**, 12579-12587.
252. W. M. Zhang, P. Sherrell, A. I. Minett, J. M. Razal and J. Chen, *Energ Environ Sci*, 2010, **3**, 1286-1293.
253. Y. G. Chen, J. J. Wang, H. Liu, R. Y. Li, X. L. Sun, S. Y. Ye and S. Knights, *Electrochem Commun*, 2009, **11**, 2071-2076.
254. K. A. Wepasnick, B. A. Smith, J. L. Bitter and D. H. Fairbrother, *Anal Bioanal Chem*, 2010, **396**, 1003-1014.
255. J. Liang, Y. Zheng, J. Chen, J. Liu, D. Hulicova-Jurcakova, M. Jaroniec and S. Z. Qiao, *Angew Chem Int Edit*, 2012, **51**, 3892-3896.
256. S. Litster and G. McLean, *J Power Sources*, 2004, **130**, 61-76.
257. B. Y. Xia, H. B. Wu, Y. Yan, H. B. Wang and X. Wang, *Small*, 2014, **10**, 2336-2339.

Appendix A

Additional Figures, Schematics and Tables

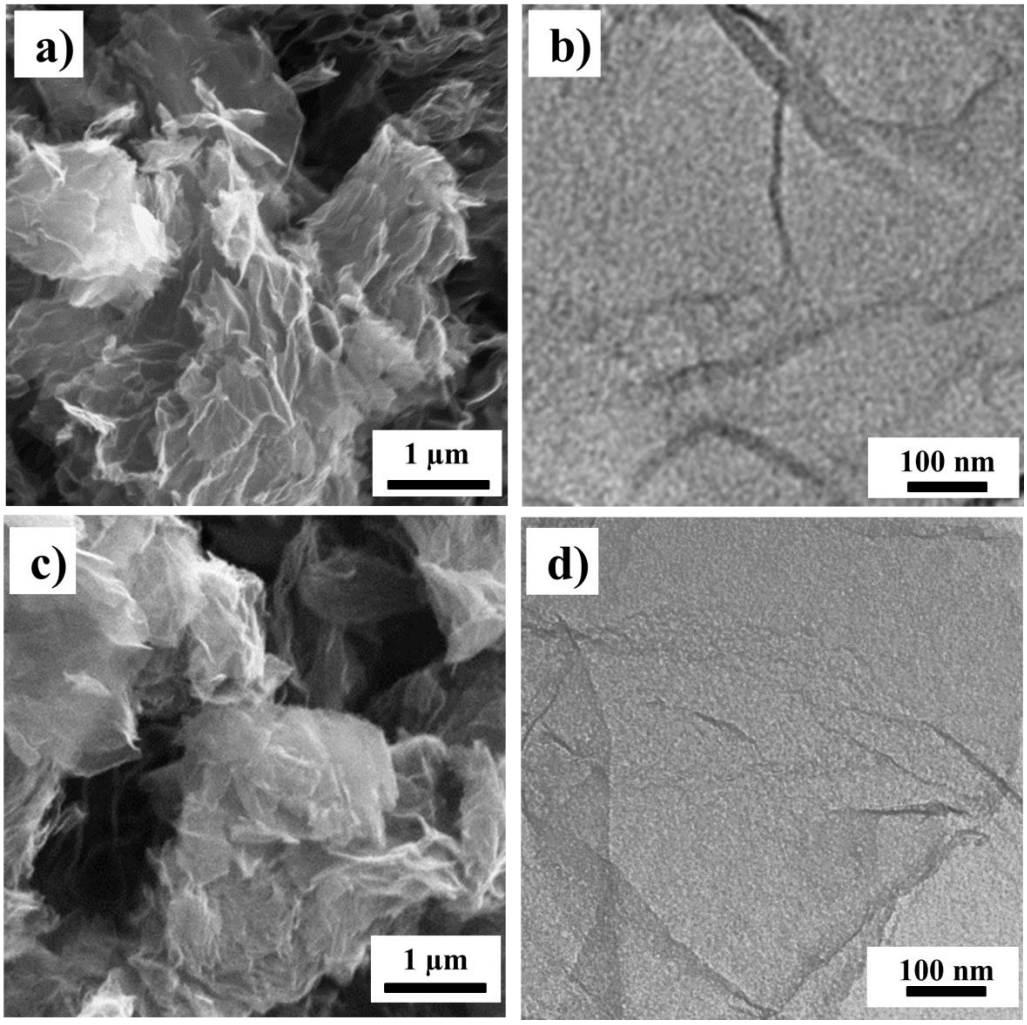

Figure A-1 SEM and TEM images of (a, b) SG and (c, d) G.

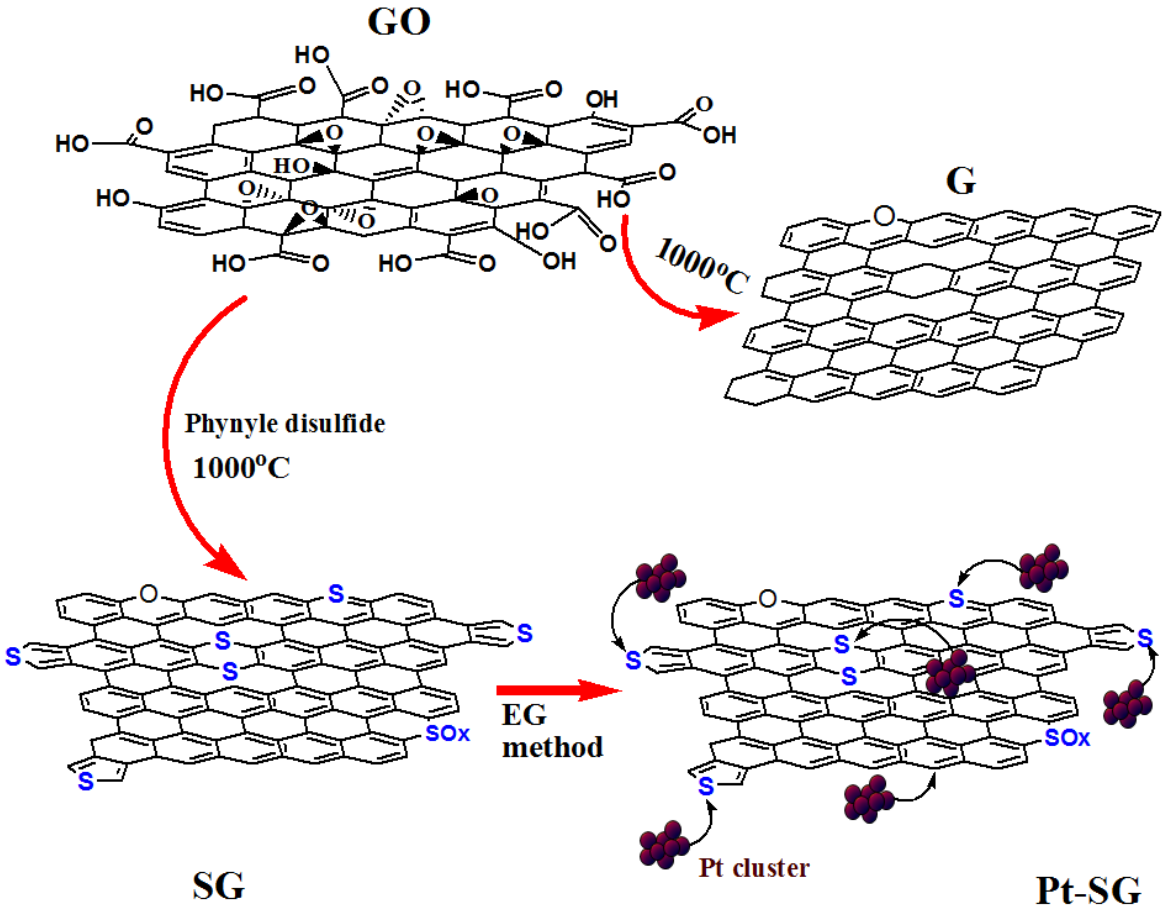

Figure A-2 Schematic diagram illustrating the fabrication process of Pt/SG.

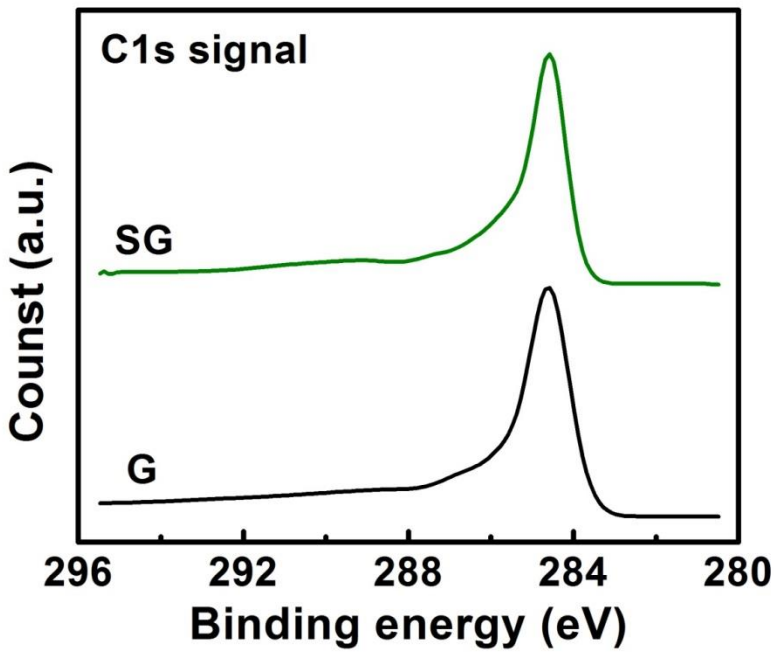

Figure A-3 XPS high resolution C1s scan spectra for SG and G.

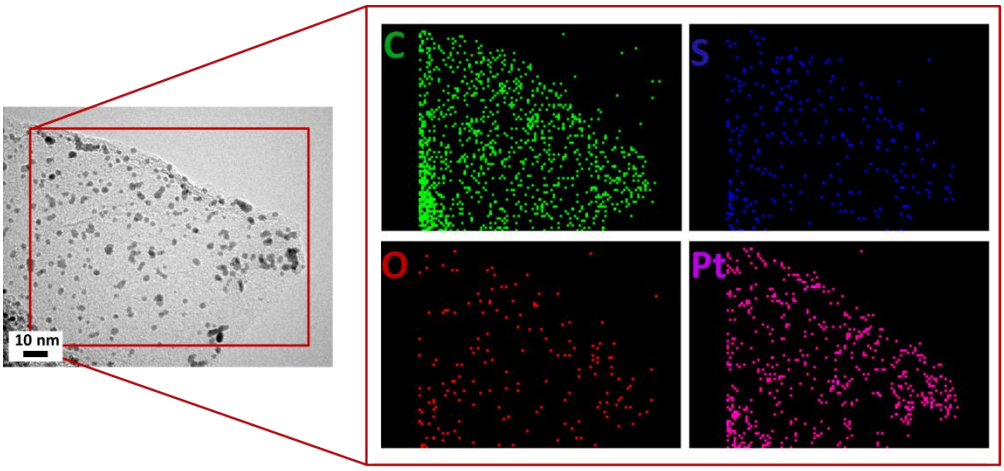

Figure A-4 TEM image of Pt/SG (left) and corresponding elemental color maps for carbon, sulfur, oxygen and platinum.

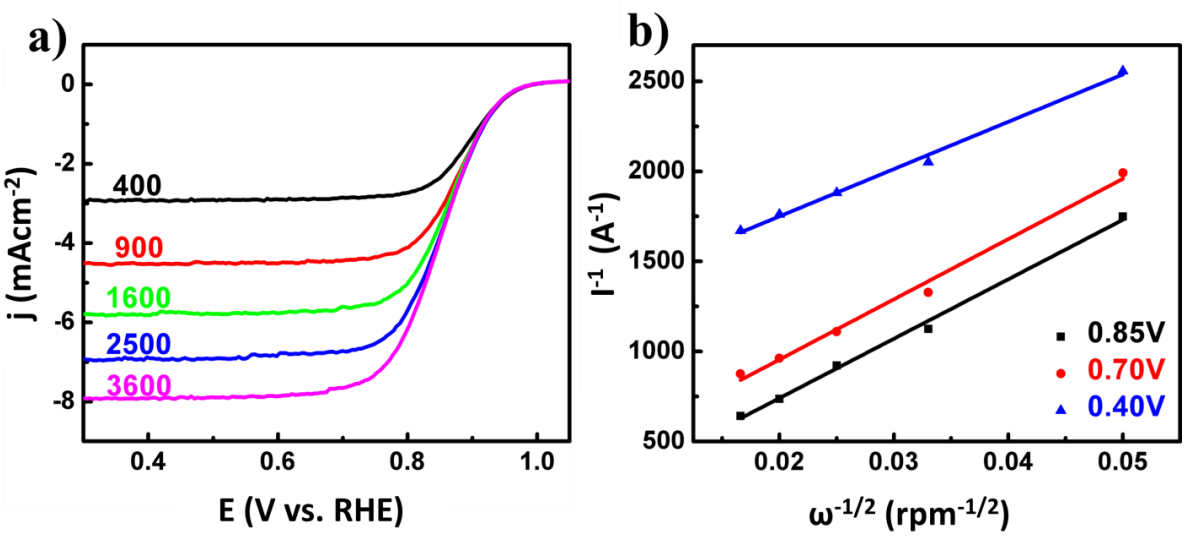

Figure A-5 (a) ORR polarization curves of Pt/SG at various electrode rotation rates and (b) corresponding Koutecky-Levich plot.

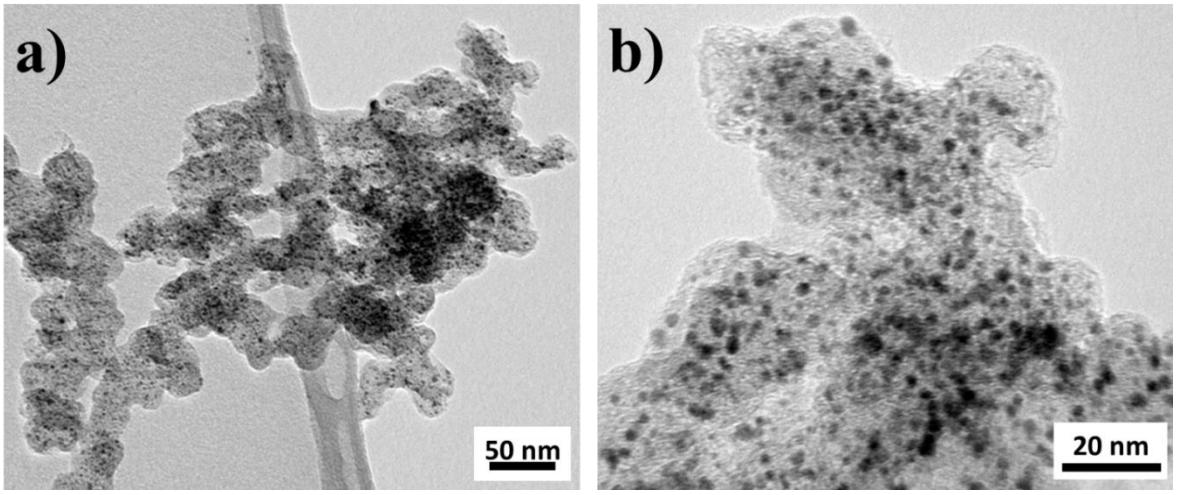

Figure A-6 TEM images of commercial Pt/C.

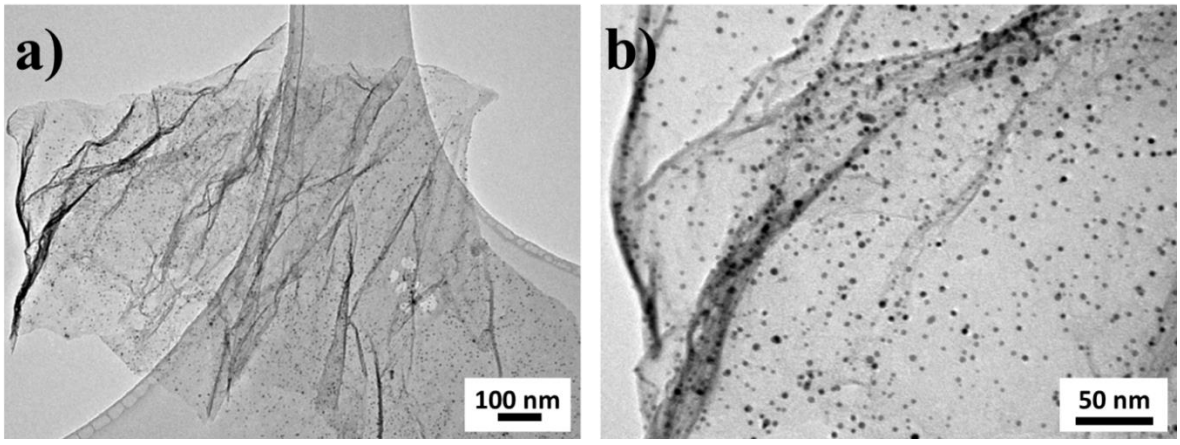

Figure A-7 TEM images of Pt/SG after ADT.

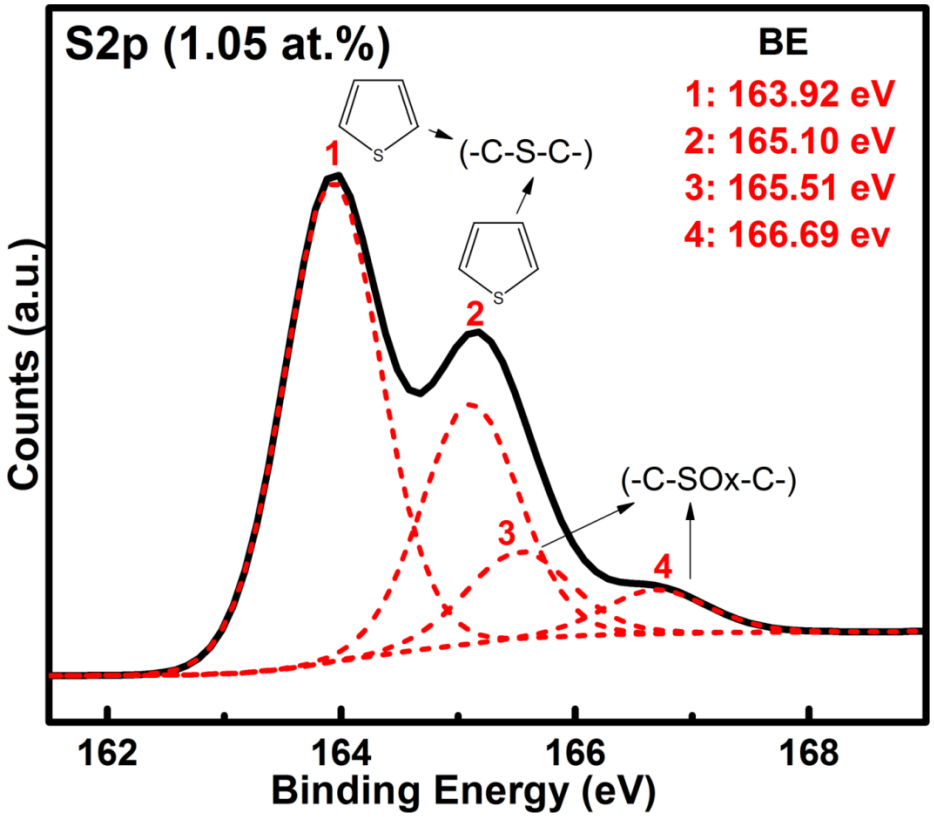

Figure A-8 XPS analysis showing the S 2p peak for SG.

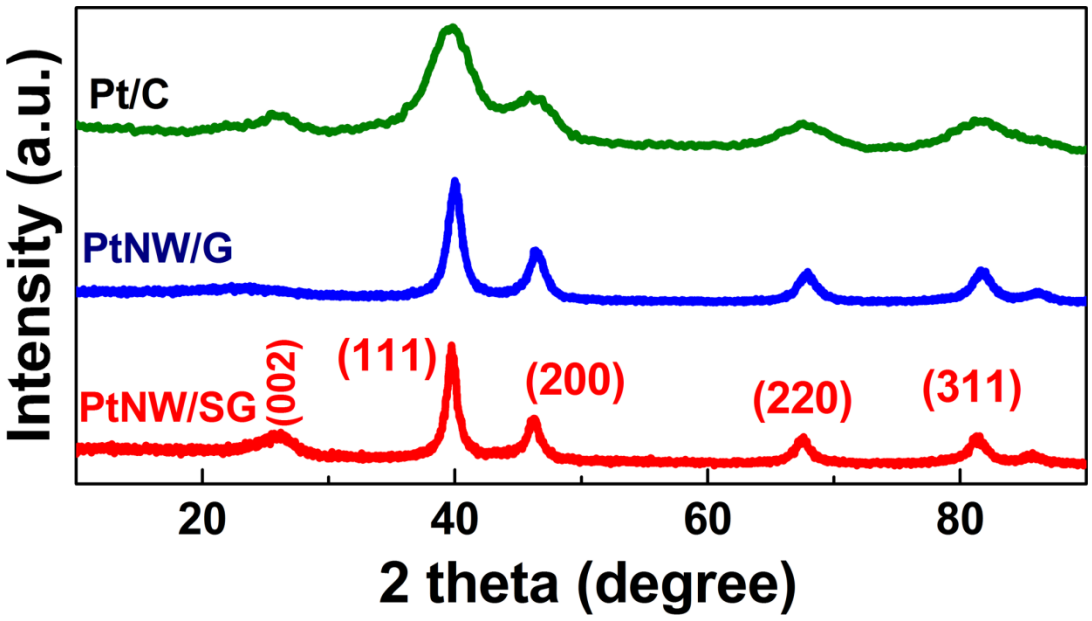

Figure A-9 XRD pattern of commercial Pt/C, PtNW/G and PtNW/SG.

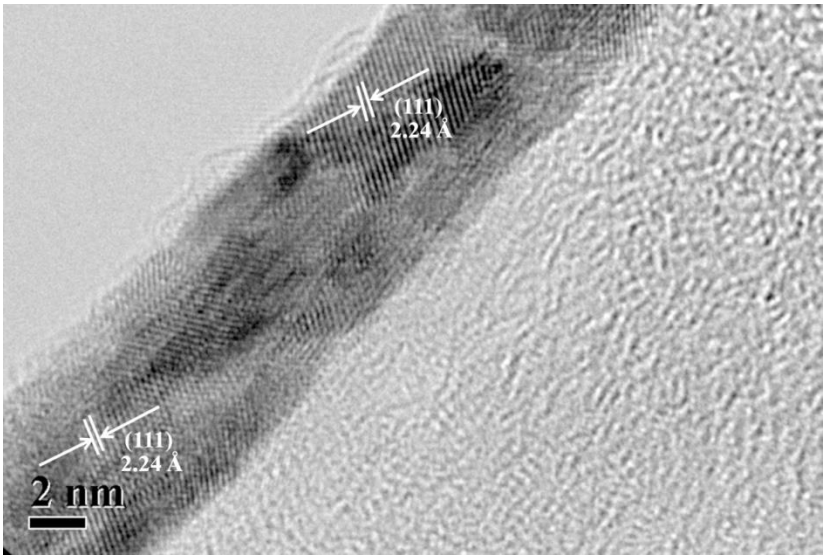

Figure A-10 HR-TEM image with d-spacing measurements of a small diameter platinum nanowire grown on SG.

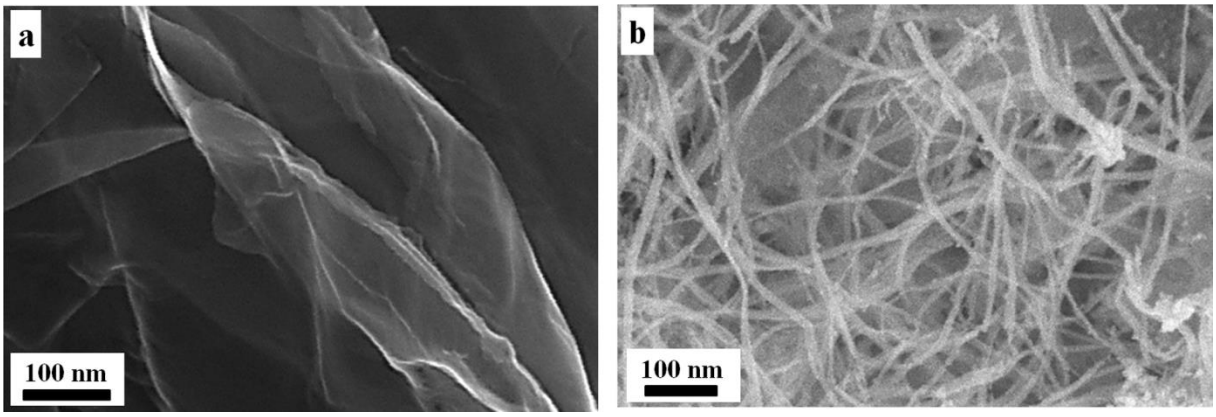

Figure A-11 SEM images of (a) graphene and (b) PtNW/G.

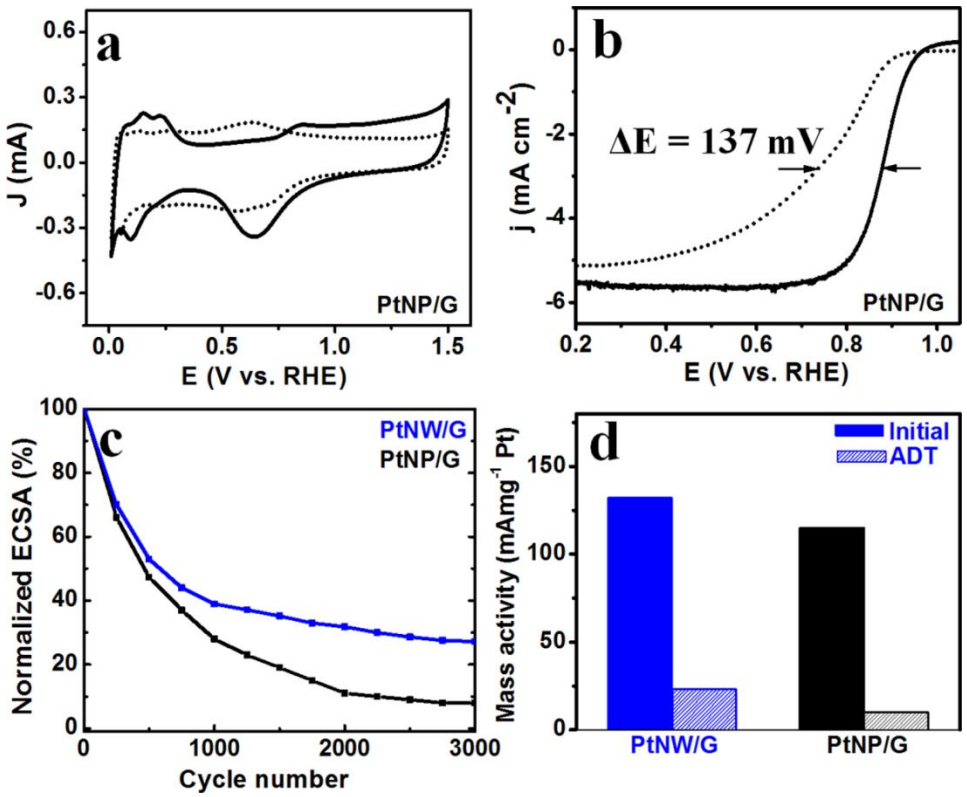

Figure A-12 Electrochemical results of Pt nanoparticles supported by graphene (PtNP/G) and comparison with Pt nanowires supported by graphene (PtNW/G); (a) CV of PtNP/G before and after 3000 cycles (b) ORR of PtNP/G before and after 3000 cycles, (c) comparison of ECSA and (d) comparison of Pt-based mass activity.

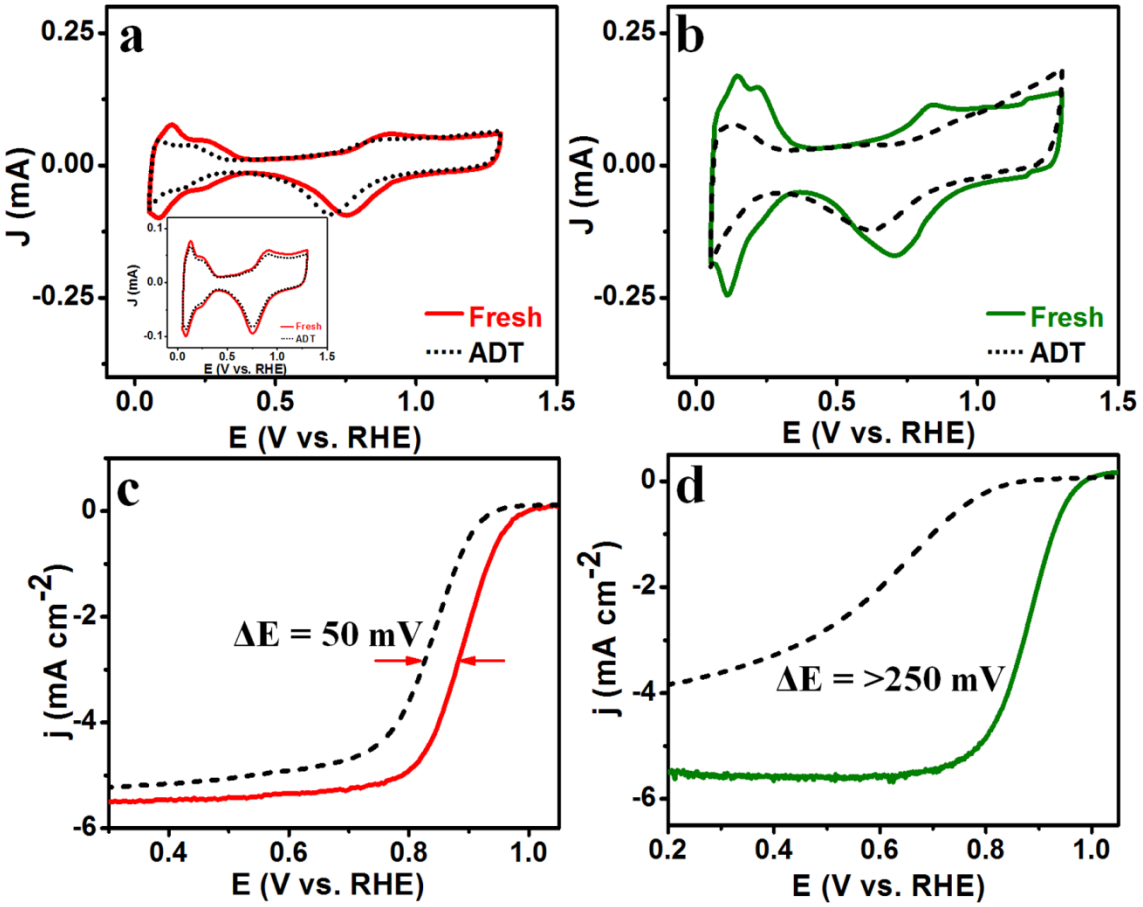

Figure A-13 Electrochemical results obtained before and after the durability test using the DOE recommended durability testing protocol: (30,000 cycles, potential range: 0.6-1.0, in O_2-saturated solution); (a) CV for PtNW/SG (inset-CV collected after 6000 cycles) and (b) Pt/C; (c) ORR activity for PtNW/SG and (d) Pt/C.

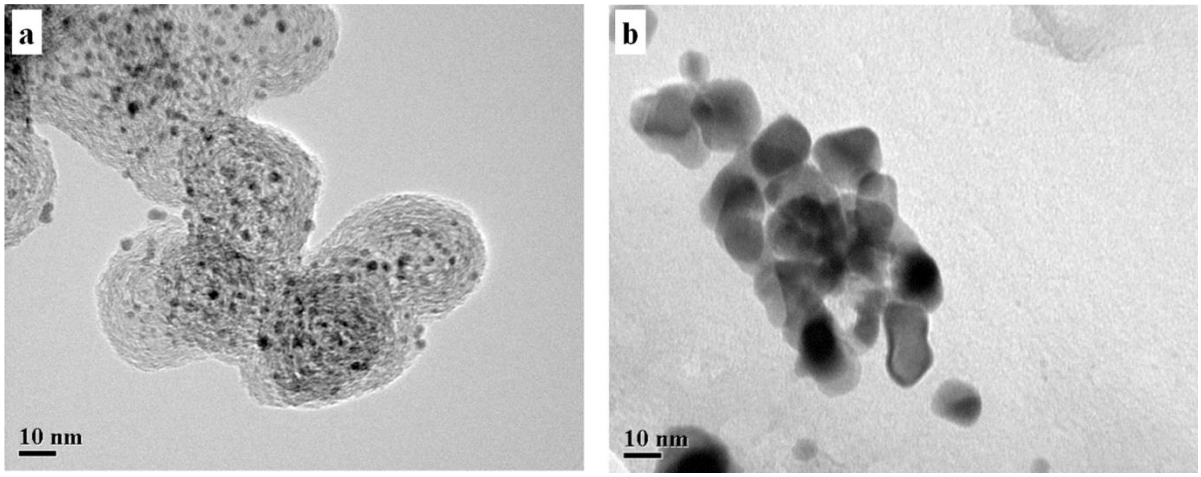

Figure A-14 TEM images of Pt/C: (a) fresh and (b) after 3000 cycles.

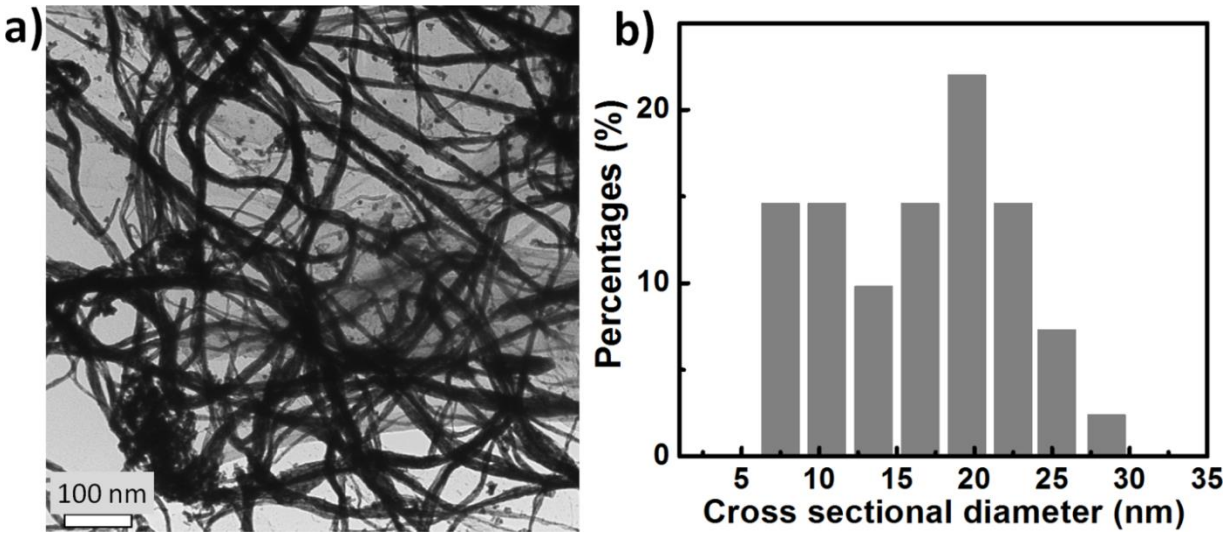

Figure A-15 TEM image and particle size histogram of PtNW/G.

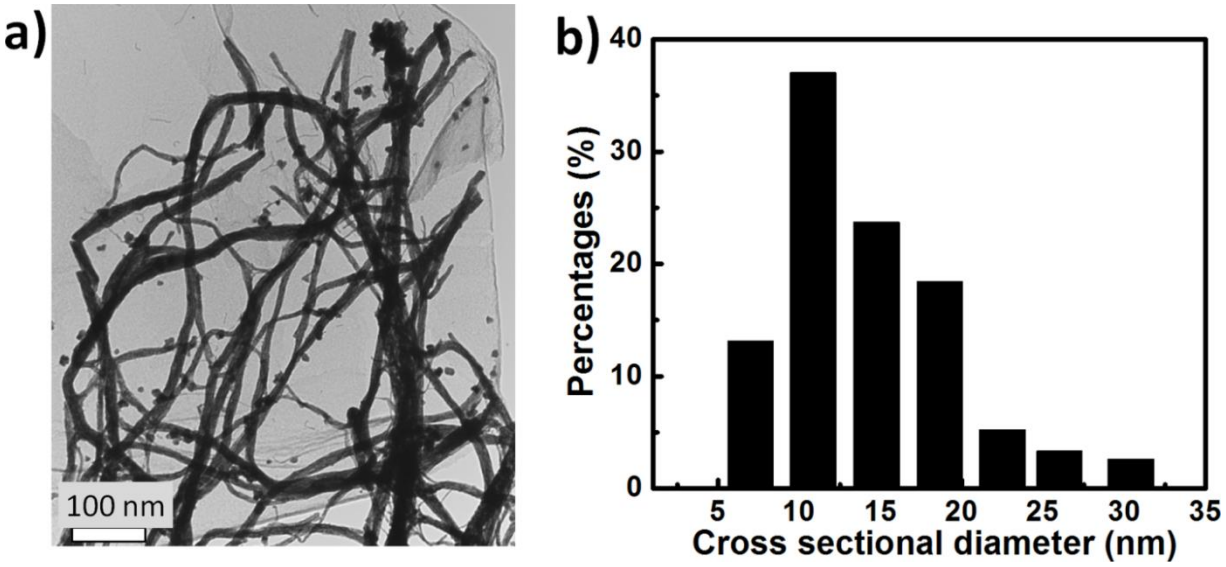

Figure A-16 TEM image and particle size histogram of PtNW/SG-1.

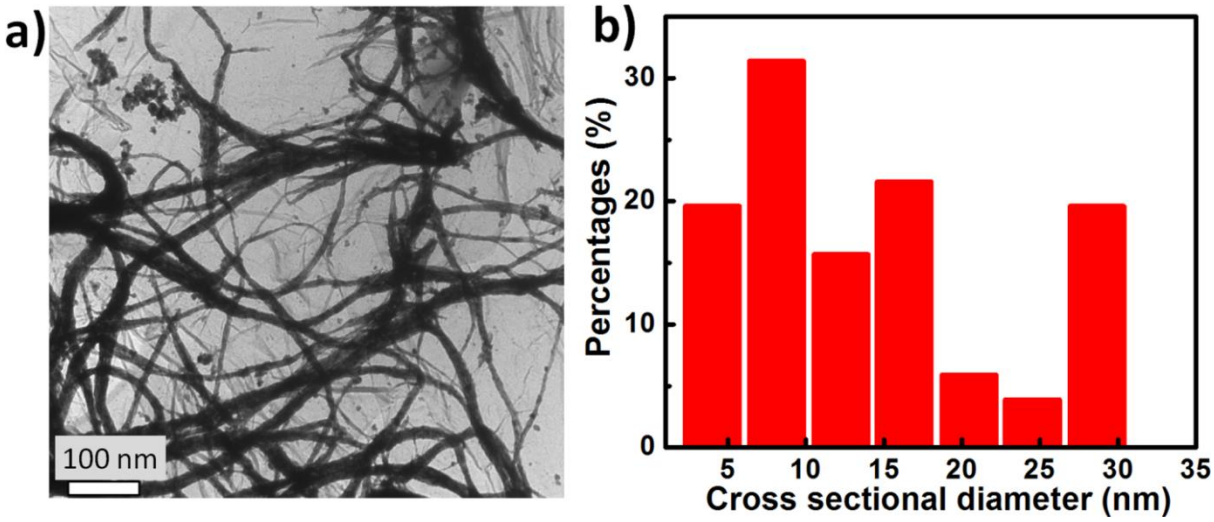

Figure A-17 TEM image and particle size histogram of PtNW/SG-2.

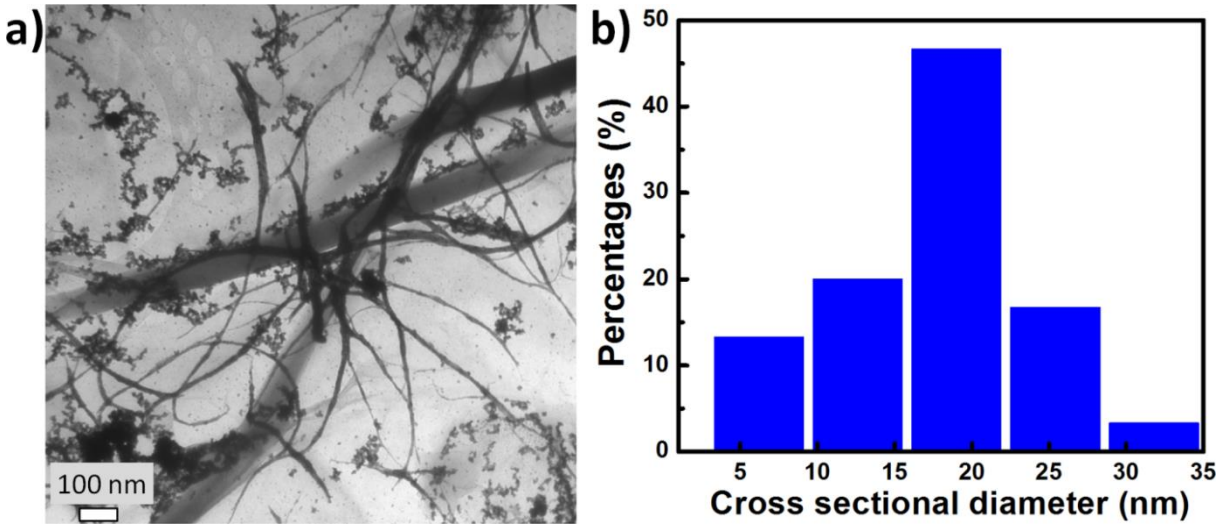

Figure A-18 TEM image and particle size histogram of PtNW/SG-3.

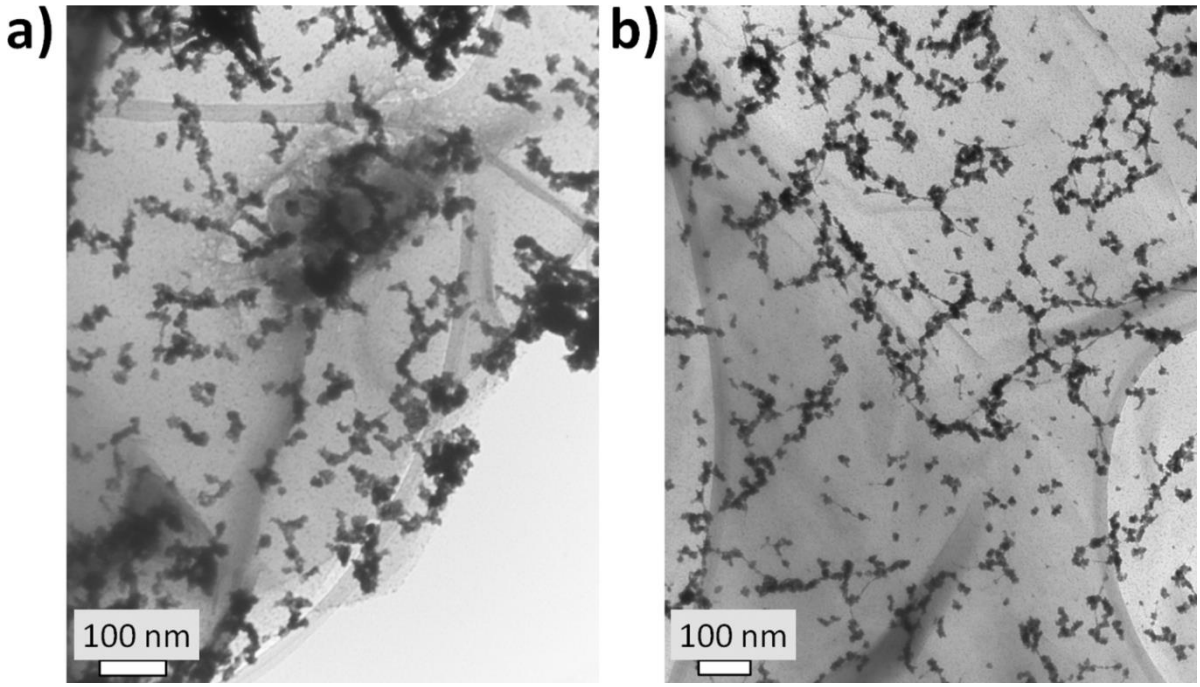

Figure A-19 TEM image and particle size histogram of PtNW/SG-4.

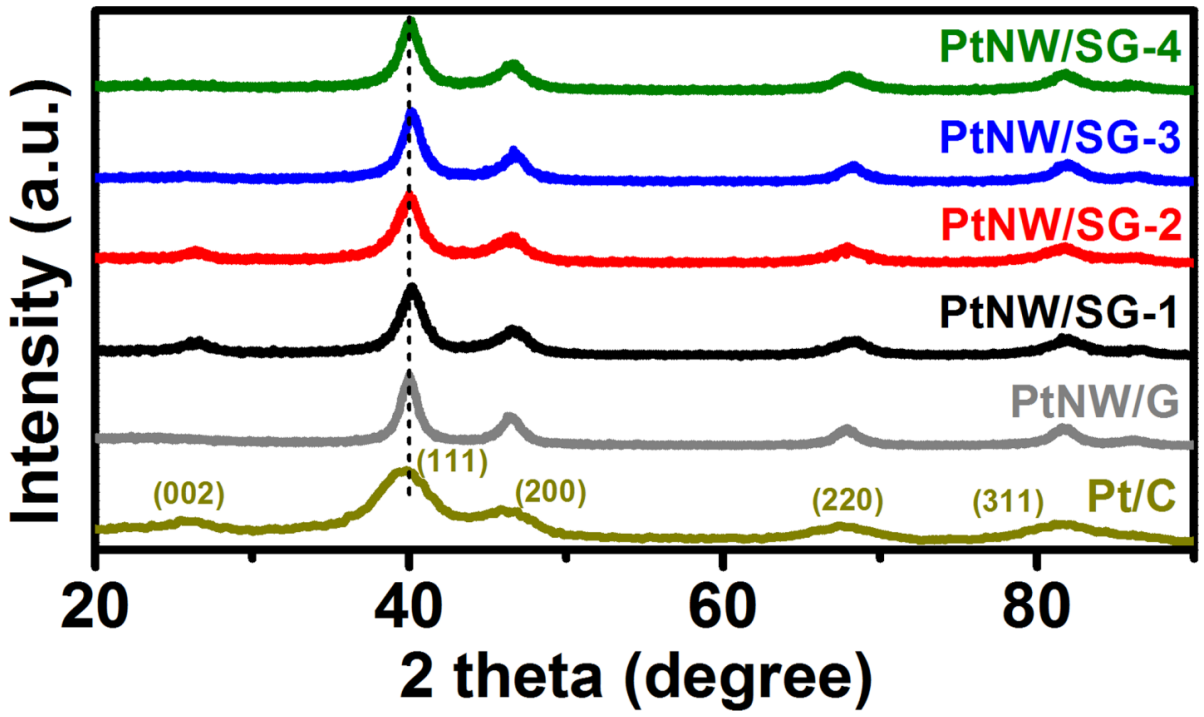

Figure A-20 XRD pattern of Pt/C, PtNW/G, PtNW/SG-1, PtNW/SG-2, PtNW/SG-3 and PtNW/SG-4.

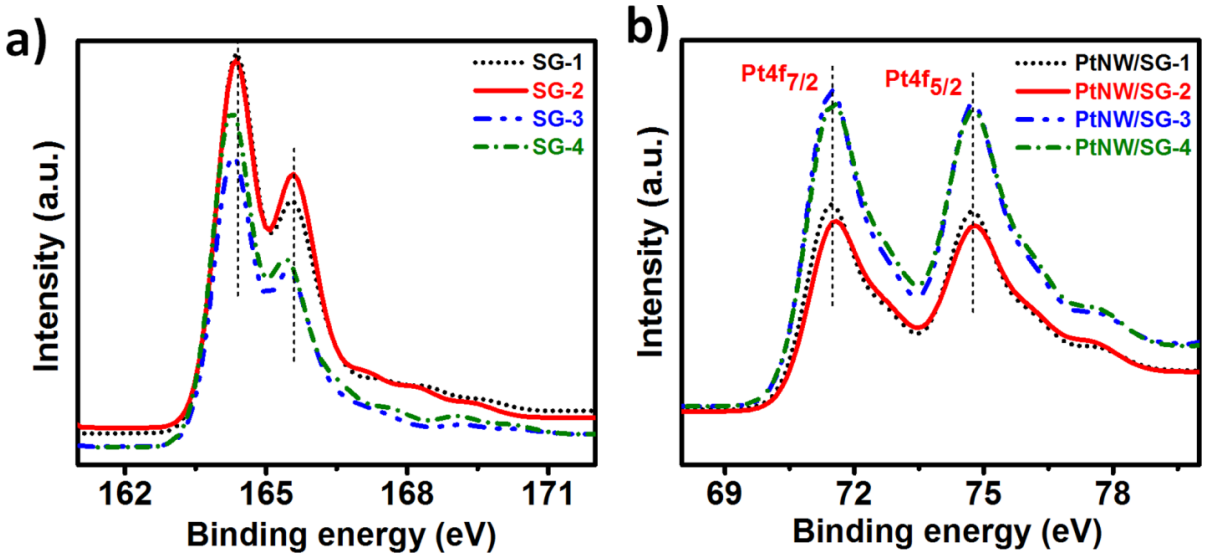

Figure A-21 a) XPS high resolution S2p scan spectra of SG-1, SG-2, SG-3 and SG-4, b) XPS high resolution Pt4f scan spectra for PtNW/SG-1, PtNW/SG-2, PtNW/SG-3 and PtNW/SG-4.

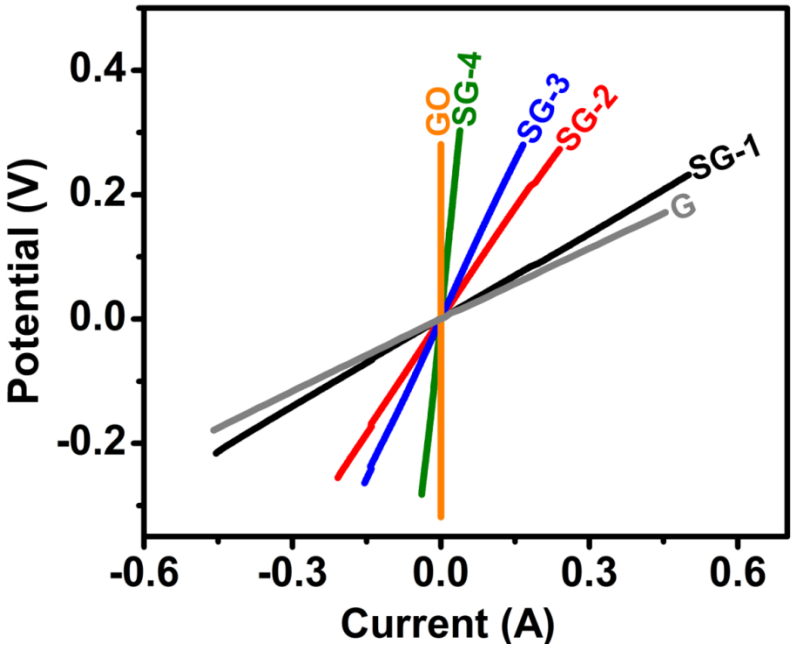

Figure A-22 V vs I plots for G, SGs and GO to obtain resistance using linear polarization technique (LPR).

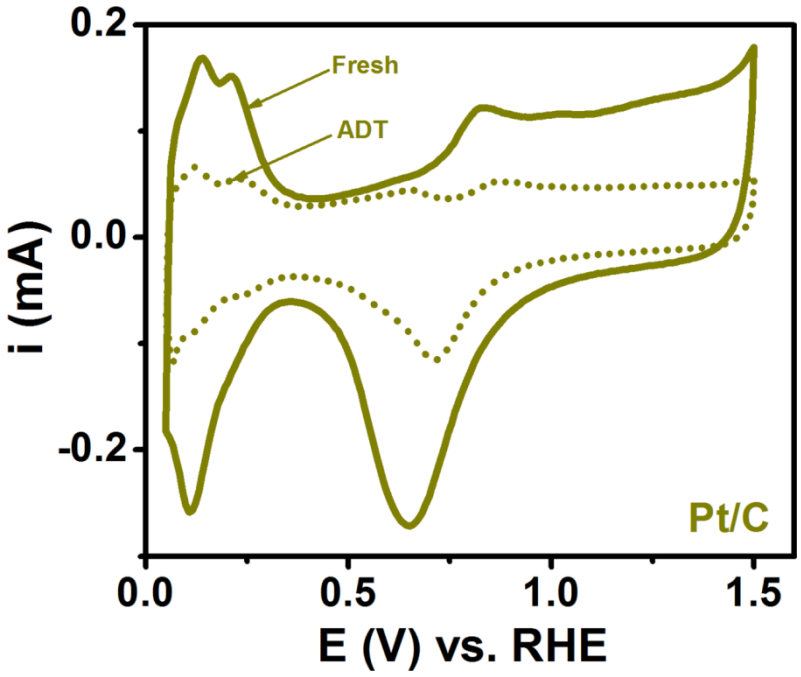

Figure A-23 CV curves of Pt/C obtained before and after ADT.

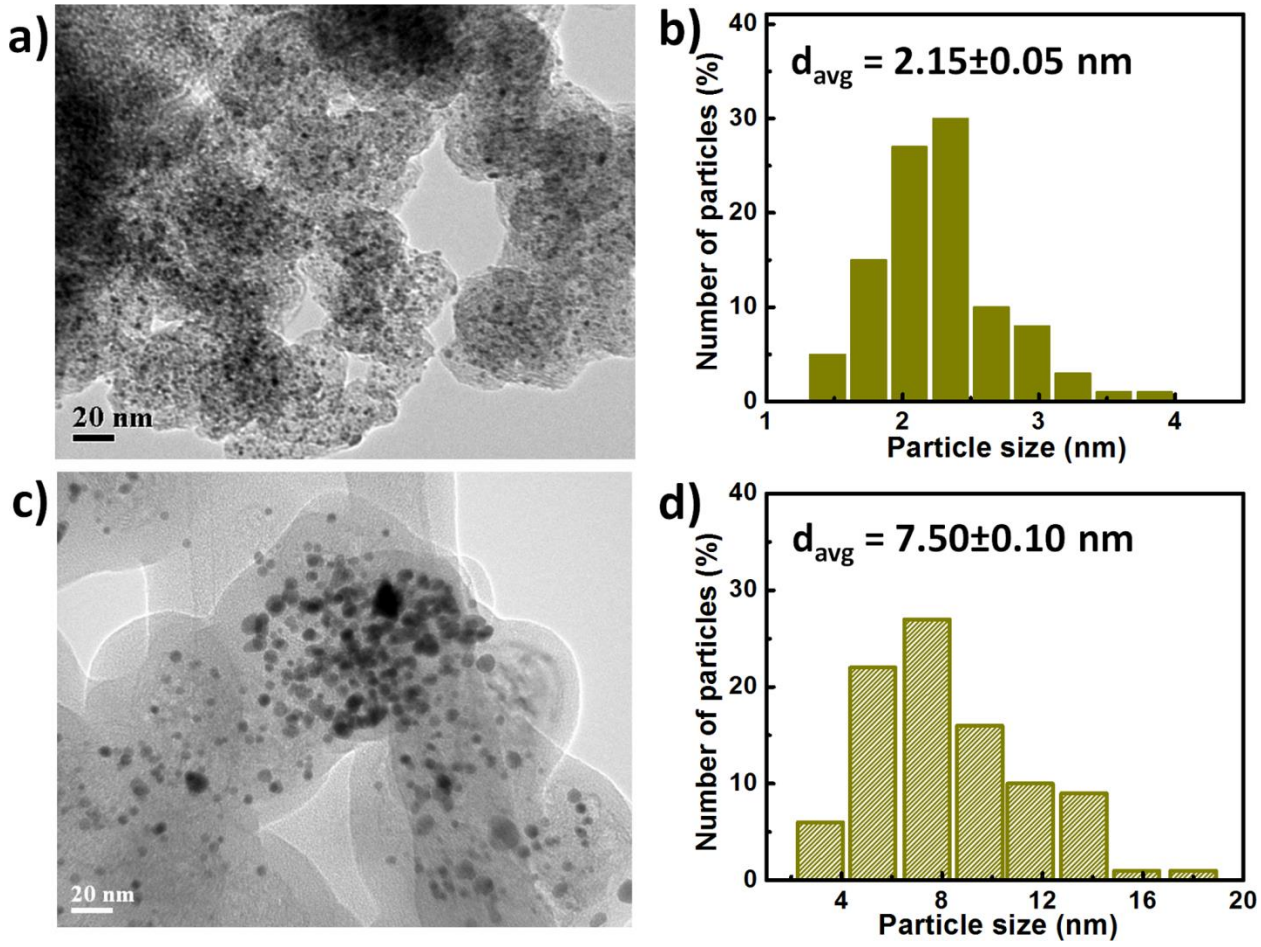

Figure A-24 TEM images and particle size histograms of Pt/C a-b) before and c-d) after ADT.

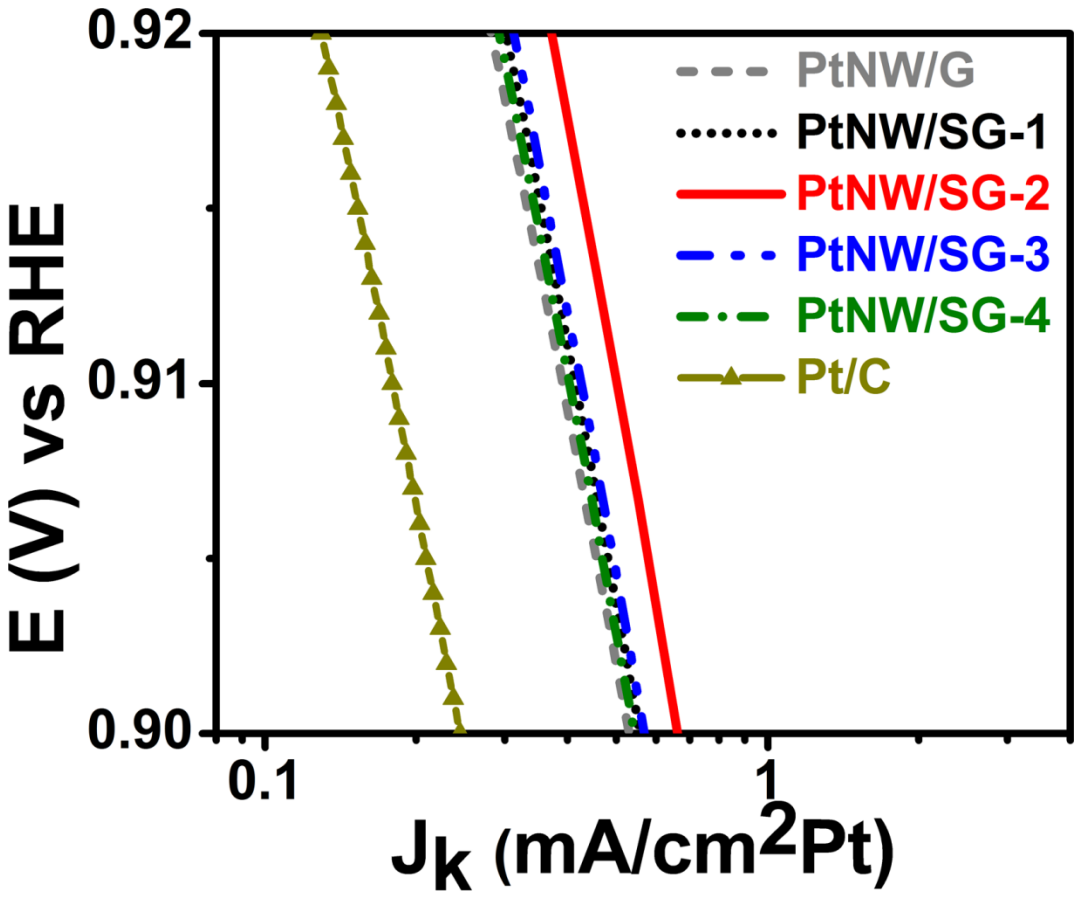

Figure A-25 Kinetically corrected Pt-specific activities of PtNW/G, PtNW/SG-1, PtNW/SG-2, PtNW/SG-3, PtNW/SG-4 and Pt/C.

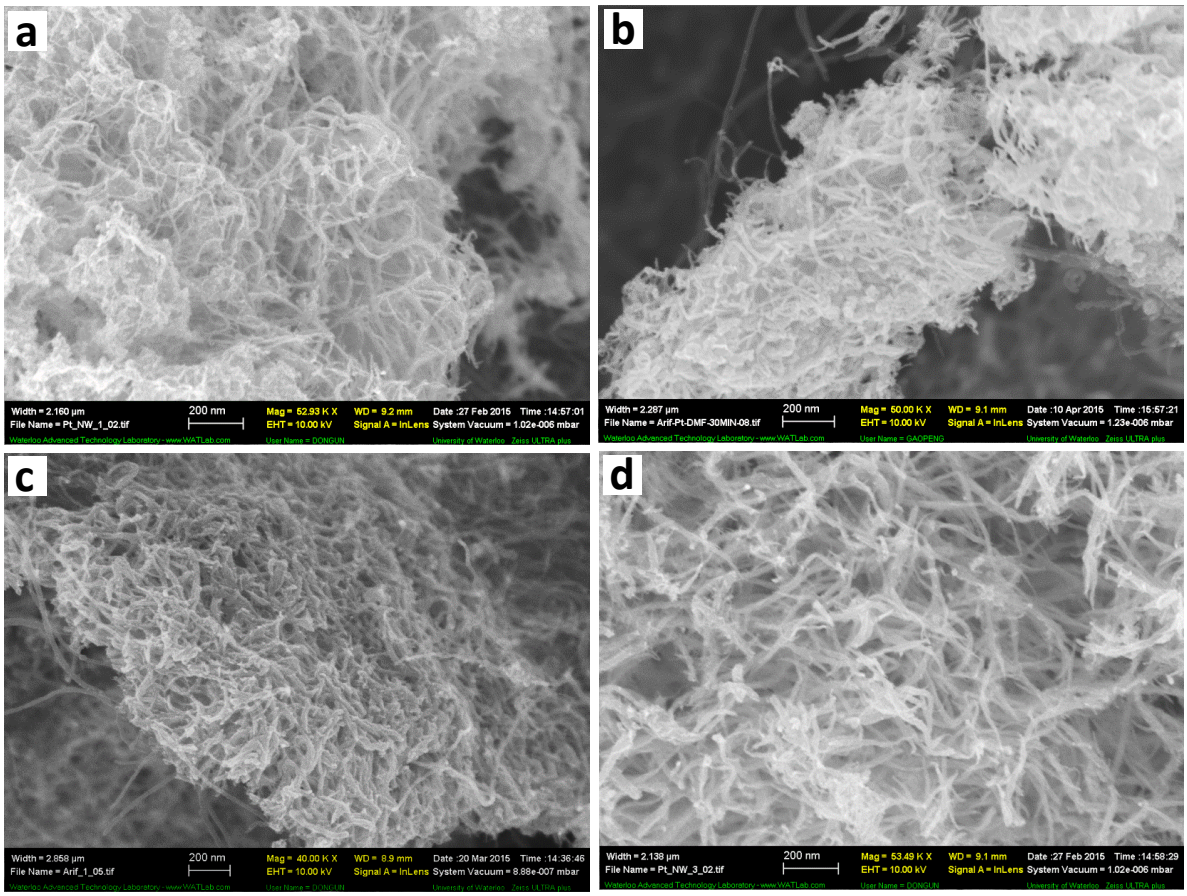

Figure A-26 SEM images of products obtained from reaction mixture containing 15 mL EG, 15 mL DMF, 1.5 g KOH, 10 mg Pt and 10 mg S-CNT. Products obtained after a) mixing precursors together for 24 h, b) dissolving Pt salt in EG and then adding the resulting solution dropwise into a homogeneous mixture of DMF, KOH and S-CNT, c) dissolving Pt salt in DMF at first and then adding the resulting solution dropwise into a homogeneous mixture of EG, KOH and S-CNT and d) adding S-CNT to a homogeneous mixture of Pt salt, EG, DMF and KOH to produce well defined Pt nanowires.

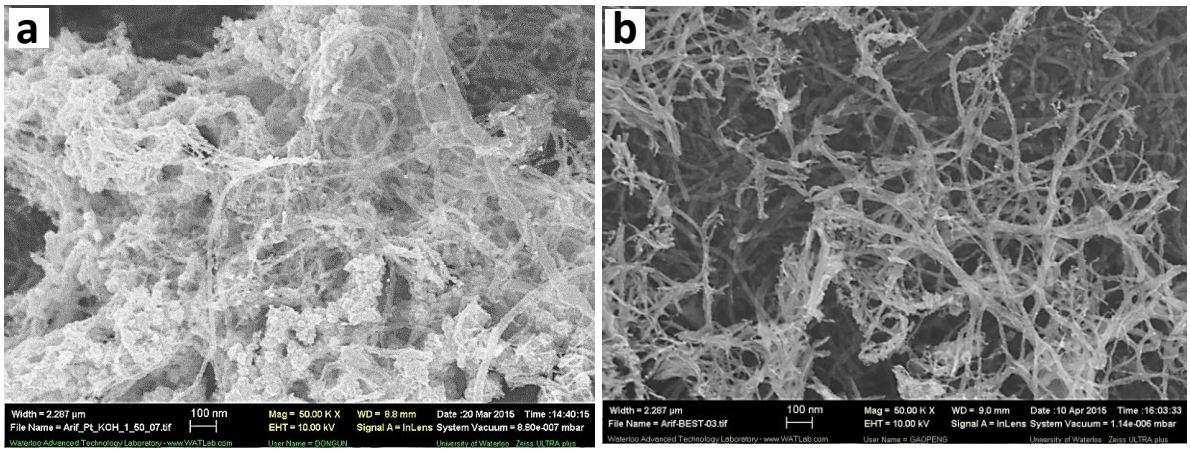

Figure A-27 SEM images of the PtNW/S-CNT synthesized in 15 mL EG, 15 mL DMF, 10 mg Pt and 10 mg S-CNT using a) 1 g KOH, and b) b) 2.0 g KOH. When the amount of KOH is reduced from 1.5 to 1 g, a mixture of nanoparticles and nanowires was observed. However, as the amount of KOH increases from 1.5 to 2 g, the amount of nanoparticles produced declines and large-diameter nanowires are preferentially formed. In this system, more ammine species that promote the formation of Pt nanowires are produced in the presence of KOH.

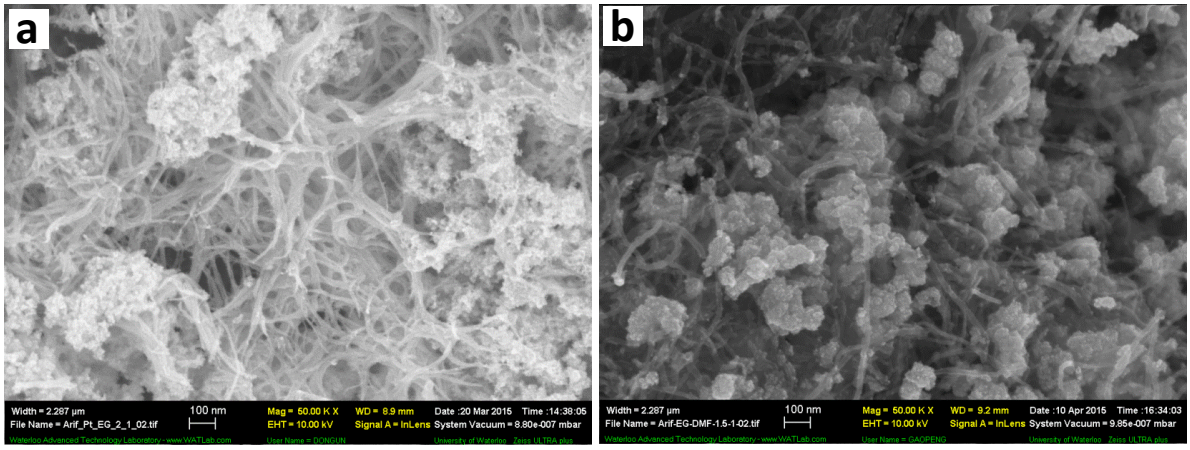

Figure A-28 SEM images of the PtNW/S-CNT synthesized in 15 mL DMF, 1.5 g KOH, 10 mg Pt and 10 mg S-CNT using a) 10 mL EG, and b) 5 mL EG. Reduction of the amount of EG from 15 to 10 mL leads to the formation of Pt nanowires and blocks of nanoparticles. When the amount of KOH is decreased as well, only Pt nanoparticles form.

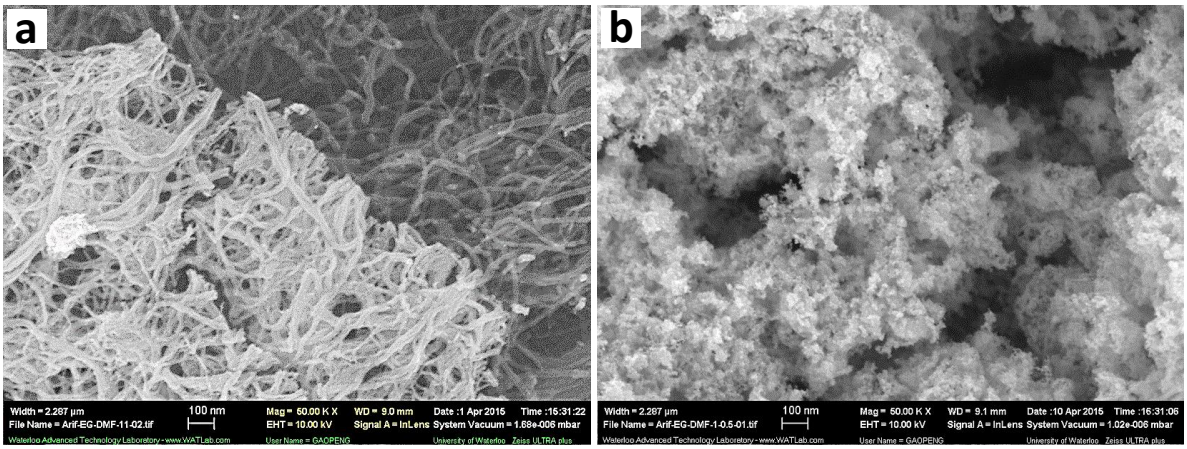

Figure A-29 SEM images of the PtNW/S-CNT synthesized in 15 mL EG, 1.5 g KOH, 10 mg Pt and 10 mg S-CNT using a) 10 mL DMF, b) 5 mL DMF. A reduction in the amount of DMF significantly interferes with the formation of Pt nanowires. It has been reported that ammine species produced by the reaction of KOH/NaOH and DMF affect the growth of Pt nanostructures at the presence of support materials.[257] Therefore, it is believed that a certain amount of DMF is required to obtain well-defined Pt nanowires in the presence of S-CNT.

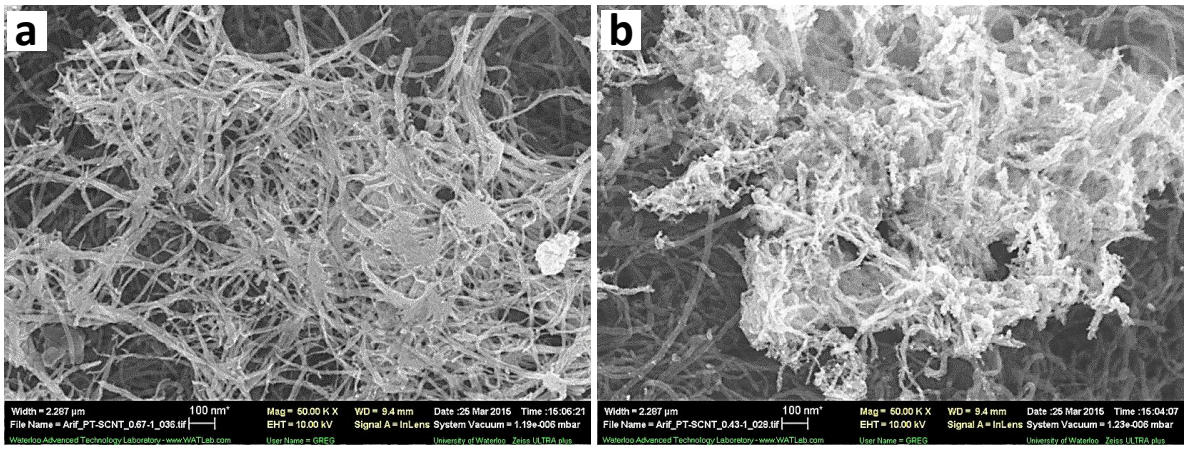

Figure A-30 SEM images of the PtNW/S-CNT synthesized in 15 mL EG, 1.5 g KOH, 15 mL DMF and 10 mg S-CNT using a) 6.7 mg Pt, b) 4.3 mg Pt. The formation of nanowires was inhibited by lowering the amount of Pt loaded.

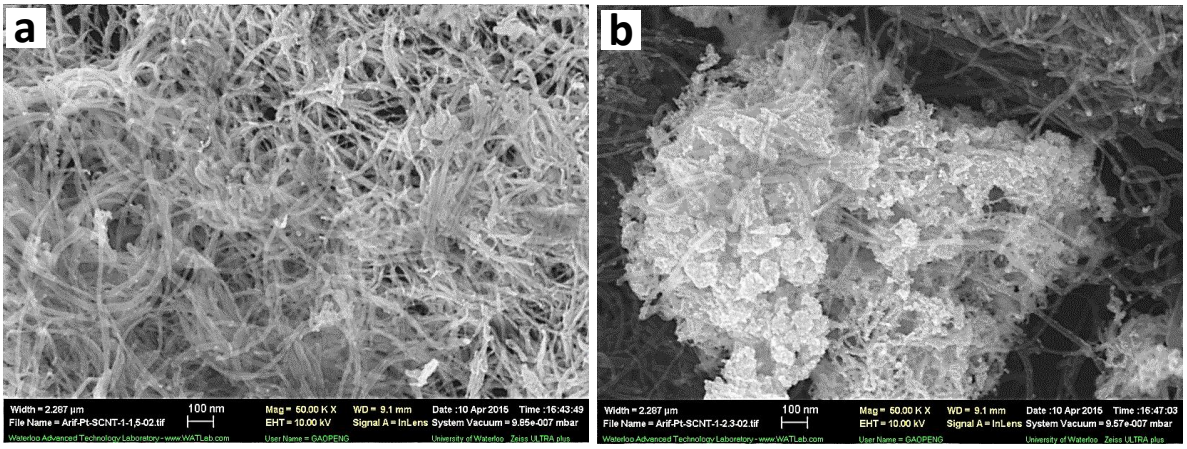

Figure A-31 SEM images of the PtNW/S-CNT synthesized in 15 mL EG, 1.5 g KOH, 15 mL DMF and 10 mg Pt. a) 15 mg S-CNT, b) 23 mg S-CNT. An increase in the amount of S-CNT used significantly interrupt the formation of Pt nanowires.

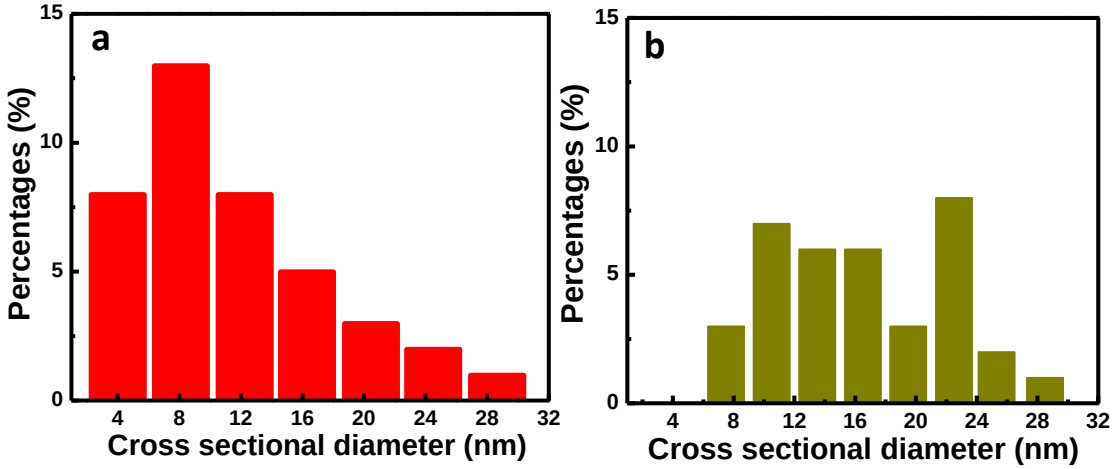

Figure A-32 Particle size histogram of a) PtNW/S-CNT and b) PtNW/F-CNT.

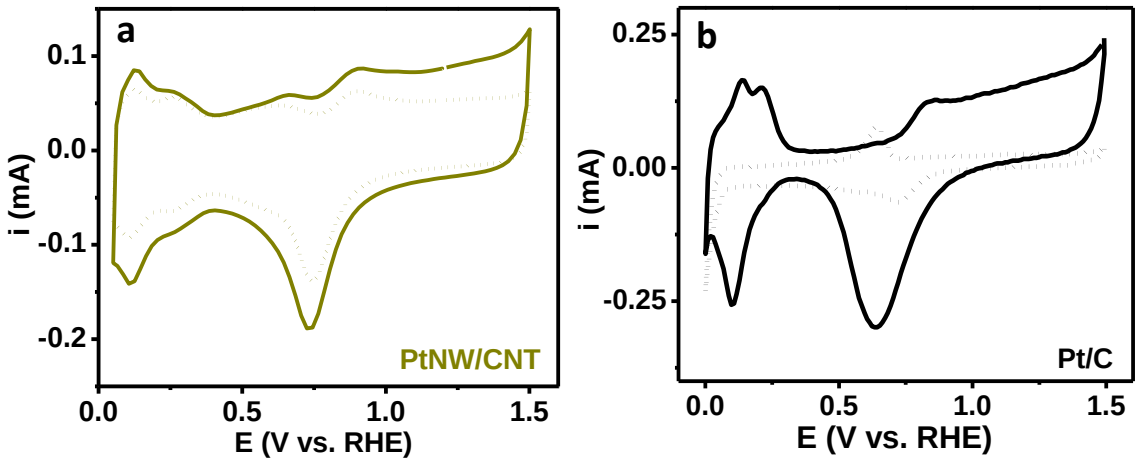

Figure A-33 CV curves obtained before and after ADT. a) PtNW/F-CNT and b) Pt/C.

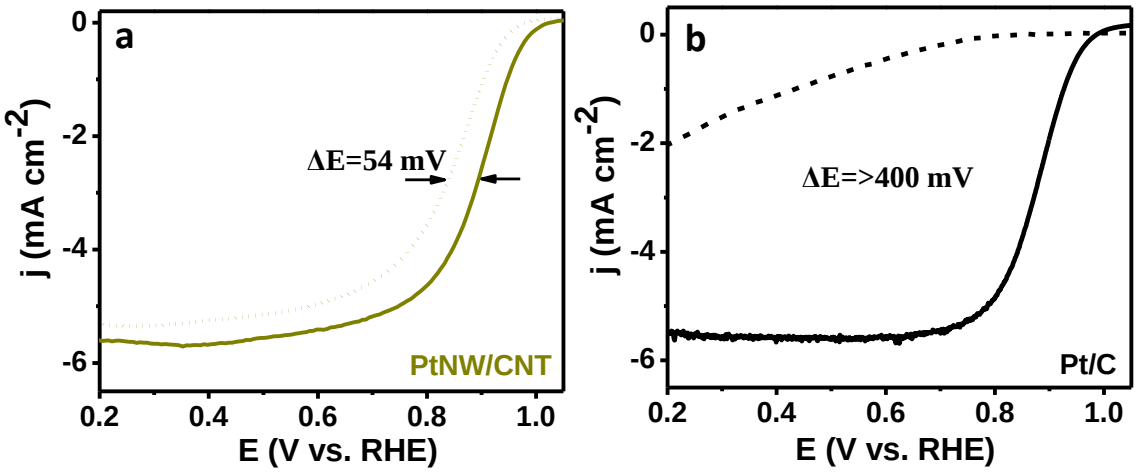

Figure A-34 ORR polarization curves obtained before and after ADT. a) PtNW/F-CNT and b) Pt/C.

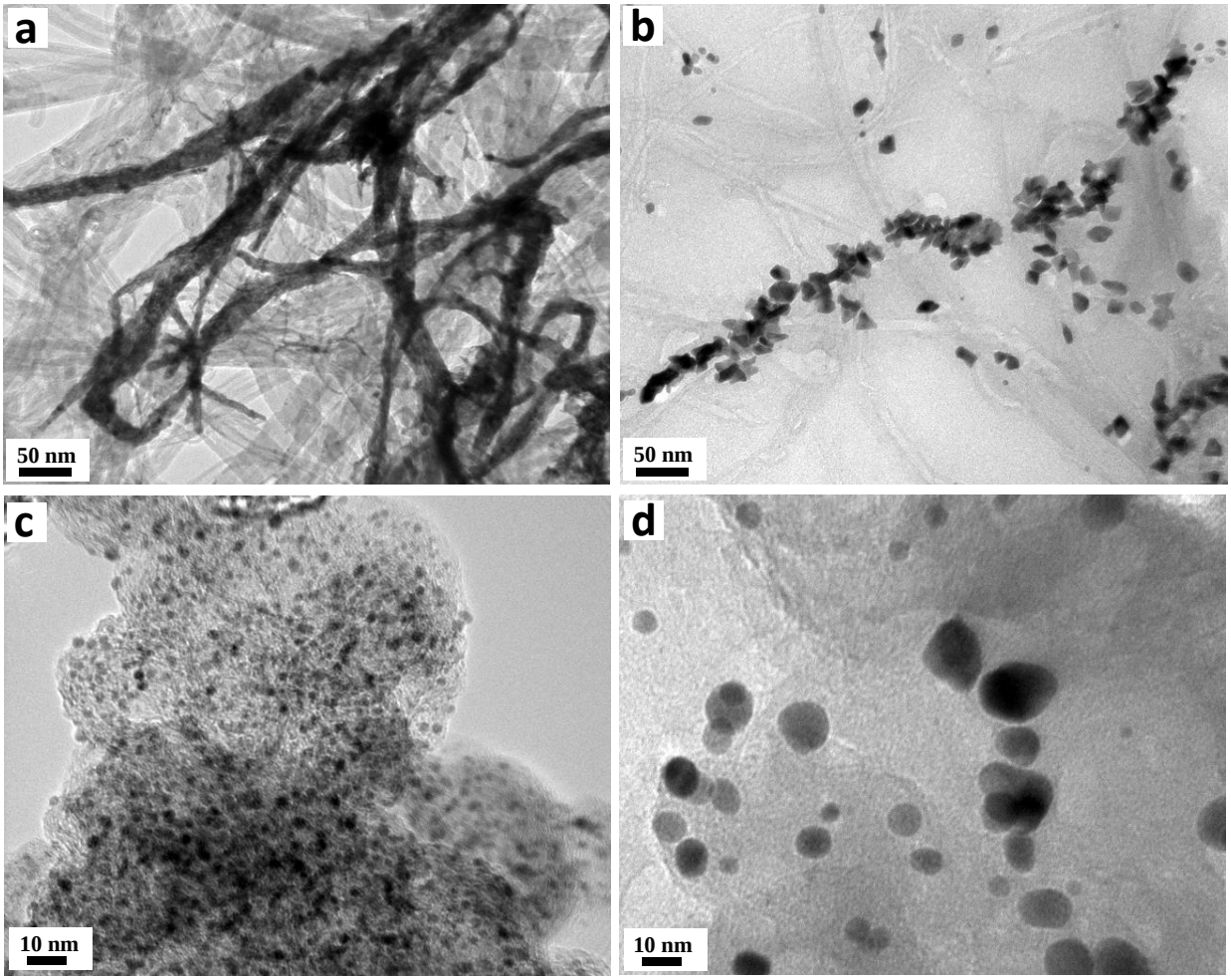

Figure A-35 TEM images obtained before and after ADT a-b) PtNW/F-CNT and c-d) Pt/C.

Table A-1 Surface atomic concentrations for SG and G, as determined by XPS

Sample	**Carbon (at. %)**	**Sulfur (at. %)**	**Oxygen (at. %)**
SG	93.03	2.32	4.65
G	92.51	-/-	7.49

Table A-2 Surface atomic concentrations for SG materials as determined by EDX and XPS

	S (EDX/XPS)	O (XPS)
SG-1	0.35±0.10/----------	12.90±0.02
SG-2	1.30±0.10/1.40±0.10	9.90±0.05
SG-3	2.70±0.05/2.80±0.05	4.45±0.06
SG-4	3.95±0.05/4.06±0.03	2.30±0.10

Table A-3 Comparison of exchange current densities (j_o) for oxygen reduction reaction

Exchange current density, j_o (A/cm^2) at low current regime				
	20^oC	30^oC	40^oC	50^oC
PtNW/G	7.6×10^{-9}	3.2×10^{-8}	6.9×10^{-8}	1.9×10^{-7}
PtNW/SG-1	9.5×10^{-9}	5.5×10^{-8}	1.1×10^{-7}	2.7×10^{-7}
PtNW/SG-2	5.0×10^{-8}	1.5×10^{-7}	2.8×10^{-7}	5.5×10^{-7}
PtNW/SG-3	4.0×10^{-9}	2.6×10^{-8}	6.0×10^{-8}	1.7×10^{-7}
Exchange current density, j_o (A/cm^2) at high current regime				
PtNW/G	9.8×10^{-6}	2.2×10^{-5}	3.2×10^{-5}	4.8×10^{-5}
PtNW/SG-1	1.5×10^{-5}	2.3×10^{-5}	3.9×10^{-5}	6.0×10^{-5}
PtNW/SG-2	2.0×10^{-5}	7.6×10^{-5}	4.6×10^{-5}	8.0×10^{-5}
PtNW/SG-3	6.8×10^{-6}	1.3×10^{-5}	2.4×10^{-5}	4.3×10^{-5}

Table A-4 Surface atomic concentrations for F-CNT and S-CNT as determined by XPS

at%	C	O	S
S-CNT	95.03	3.95	1.02
F-CNT	95.40	4.60	-/-